Gerald Reiter, BSc

Basic Investigations and Parameter Identification of a Steer-by-Wire Torque Vectoring Vehicle

MASTER'S THESIS

to achieve the university degree of

Diplom-Ingenieur

Master's degree programme: Mechanical Engineering

submitted to

Graz University of Technology

Supervisor

Dipl.-Ing. Andreas Hackl,BSc
Institute of Automotive Engineering
Member of [FSI]

Dipl.-Ing. Andreas Mitterrutzner
ThyssenKrupp Presta AG

Graz, May 2017

Restricted access until May 2022

Danksagung

Diese Arbeit wurde in Kooperation des Fahrzeugtechnik Institutes der TU Graz und der Thyssenkrupp Presta AG erstellt.

Zu Beginn möchte ich mich bei Professor Georg Rill bedanken, der mir sein Fahrzeug Modell zur Verfügung stellte und mir aufschlussreiche Einblicke in die Simulation und Modellbildung der Fahrzeugtechnik ermöglichte. Seine Publikationen bilden die Grundlage dieser Masterarbeit und haben zur Erweiterung meines Wissens beigetragen.

Des Weiteren bedanke ich mich bei dem gesamten Steer-by-Wire Team, insbesondere bei Kristof Polmans, Andreas Mitterrutzner und Carlo Miano, welche mich immer unterstützten und mich in meiner Arbeit bestärkten.

Außerdem möchte ich mich beim Fahrzeugtechnik Institut der TU Graz für die interessante Masterarbeit bedanken vor allem bei meinem Betreuer Andreas Hackl, der mir diese Arbeit ermöglichte. Maßgeblich für den Entstehungsprozess waren die vielen interessanten und fachspezifischen Diskussionen mit ihm.

Ein besonderer Dank gilt meiner Familie, die mich während meiner gesamten Ausbildung in jeglicher Hinsicht unterstützte und mir immer Rückhalt gegeben hat. Meinen Freunden, die mich durch meine Studienzeit begleitet haben, möchte ich für diese positive und schöne Zeit danken.

Ein besonderer Dank gilt meiner Freundin, die mir immer zur Seite stand.

Statutory Declaration

Ich erkläre an Eides statt, dass ich die vorliegende Arbeit selbstständig verfasst, andere als die angegebenen Quellen/Hilfsmittel nicht benutzt, und die den benutzten Quellen wörtlich und inhaltlich entnommenen Stellen als solche kenntlich gemacht habe.

Graz, am ....
(Unterschrift)

I declare that I have authored this thesis independently, that I have not used other than the declared sources / resources, and that I have explicitly marked all material which has been quoted either literally or by content from the used sources.

....
(date) (signature)

Abstract

This thesis deals with modelling, parametrization and validation of a steer-by-wire torque vectoring vehicle. The test vehicle is an electrically powered BMW X5, provided from the company Thyssenkrupp Presta AG.

The modelling part is focused on the suspensions and is based on a multi-body vehicle model from Professor Georg Rill. Hence, three-dimensional kinematic suspension models for the front and rear axle will be build up and validated by measurement data.

The next part is about the parameter identification of the entire vehicle model, especially the masses, moment of inertias and centers of gravity of certain components.

Next, the two different driving modes of the steer-by-wire vehicle will be validated. The first one is a conventional mode, whereby an electro-mechanic actuator at the rack generates the steering movement of the wheels. The second one is a torque vectoring mode, whereby a torque difference at the wheels generates the steering movement.

Finally, a parameter study was done and the efficiency of the torque vectoring steering was investigated. Furthermore, the driving behavior of these two modes was analyzed.

Kurzfassung

Die vorliegende Masterarbeit befasst sich mit der Modellierung, Parametrisierung und Validierung eines Steer-by-Wire Torque Vectoring Fahrzeuges. Das Versuchsfahrzeug ist ein elektrisch angetriebener BMW X5 der Firma Thyssenkrupp Presta AG.

Aufbauend auf dem Mehrkörper-Fahrzeugmodell von Professor Georg Rill liegt der Schwerpunkt der Modellierung bei den Fahrwerken. Hierbei werden sowohl für die Hinterachse als auch für die Vorderachse kinematische dreidimensionale Modelle aufgebaut und mit Messdaten validiert.

Die Parametrisierung bezieht sich auf das gesamte Fahrzeugmodell, wobei der Fokus auf der Bestimmung von Massen, Massenträgheiten und Schwerpunktslagen der einzelnen Teilkörper liegt.

Validert werden zwei unterschiedliche Fahrmodi des Steer-by-Wire Fahrzeuges. Der erste ist ein konventioneller Modus, bei dem ein elektromechanischer Aktuator am Lenkgetriebe den Lenkeinschlag generiert. Der zweite ist der Torque-Vectoring Modus, bei dem der Lenkvorgang durch unterschiedliche Drehmomente an den gelenkten Rädern realisiert wird und sich dadurch ein bestimmter Lenkeinschlag einstellt.

Abschließend wird untersucht, wie sich bestimmte Parameter auf die Effizienz der Torque-Vectoring Lenkung sowie auf das Fahrverhalten beider Fahrmodi auswirken.

Contents

Symbols

Mathematical objects within this work are denoted as follows:

a	scalar
$\boldsymbol{a}$	vector
$\boldsymbol{A}$	matrix

When present, symbols in sub- and superscripts of a vector $\boldsymbol{x}$ are used in the form $\boldsymbol{x}^4_{12,3}(5)$. The numbers denote the position of the following optional assignments:

1 ... the initial position of a vector, eg. w for *wheel center*
2 ... the end position of a vector,
3 ... the coordinate system, eg. F for *vehicle*
4 ... 0 for initial state and 1 for state after movement
5 ... vector entry, 1 for x position, 2 for y position and 3 for z position

Coordinate systems

$\mathcal{O}_0$	Earth fixed coordinate system
$\mathcal{O}_F$	Vehicle fixed coordinate system, in the center of the front axle
$\mathcal{O}_1$	Wheel carrier fixed coordinate system, in the center of the front wheel on the left hand side
$\mathcal{O}_2$	Wheel carrier fixed coordinate system, in the center of the front wheel on the right hand side
$\mathcal{O}_3$	Wheel carrier fixed coordinate system, in the center of the rear wheel on the left hand side
$\mathcal{O}_4$	Wheel carrier fixed coordinate system, in the center of the rear wheel on the right hand side

Variables, parameters and constants

a	Dimension of planar four-bar linkage
a_y	Lateral acceleration
$\boldsymbol{A}_{1F}$	Transformation matrix from $\mathcal{O}_1$ to $\mathcal{O}_F$
$\boldsymbol{A}_{3F}$	Transformation matrix from $\mathcal{O}_3$ to $\mathcal{O}_F$

$\boldsymbol{A}_{\text{cardan}}$	Cardan rotation matrix
$\boldsymbol{A}_{\alpha_k}$	Rotation matrix about x-axis, part of Cardan rotation matrix
$\boldsymbol{A}_{\beta_k}$	Rotation matrix about y-axis, part of Cardan rotation matrix
$\boldsymbol{A}_{\gamma_k}$	Rotation matrix about z-axis, part of Cardan rotation matrix
$\boldsymbol{A}_{\varphi}$	Rotation matrix of revolute joint suspension arm about angle φ
$\boldsymbol{A}_{\psi}$	Rotation matrix of revolute joint suspension arm about angle ψ
b	Dimension of planar four-bar linkage
$\boldsymbol{b}$	Disturbance vector for velocity computation of suspension
$\tilde{\boldsymbol{b}}_1$	Part of vector $\boldsymbol{b}$
$\tilde{\boldsymbol{b}}_2$	Part of vector $\boldsymbol{b}$
$\boldsymbol{B}$	Coefficient matrix for velocity computation of suspension
$\boldsymbol{B}_{ij}$	$i = 1, 2$ and $j = 1, 2$ Submatrices of $\boldsymbol{B}$
c	Dimension of planar four-bar linkage
$\boldsymbol{c}_i$	i=1,2,3,4 Solution vectors of velocity computation of suspension
c_{arb}	Anti roll bar spring stiffness
c_{arb}^f	Front anti roll bar stiffness
c_{arb}^r	Rear anti roll bar stiffness
c_{s}	Spring stiffness
c_{d}	Bump stop spring coefficient
c_α	Tire cornering stiffness
$\boldsymbol{C}^0$	Auxiliary matrix of initial state vectors for $\boldsymbol{A}_{3F}$ computation
$\boldsymbol{C}^1$	Auxiliary matrix of actual state vectors for $\boldsymbol{A}_{3F}$ computation
d	Dimension of planar four-bar linkage
$\boldsymbol{d}_i$	i=1,2,3,4 Solution vectors of velocity computation of suspension
$\boldsymbol{d}_{iu}$	$i = 1, 2$ Partial derivation vectors of front wheels rotations
d_{d}	Damper coefficient
$\boldsymbol{e}$	Unit vector
$\tilde{\boldsymbol{e}}$	Skew-symmetric matrix
$\boldsymbol{e}_i^0$	$i = a, b, c$ Unit vectors of $\boldsymbol{C}^0$
$\boldsymbol{e}_i^1$	$i = a, b, c$ Unit vectors of $\boldsymbol{C}^1$
$\boldsymbol{E}$	Identity matrix
$\boldsymbol{f}$	Vector of nonlinear equations, Newton-Raphson method
F_{arb}	Absolute force of anti roll bar
F_{bs}	Absolute force of bump stop
F_{damper}	Absolute force of damper
F_{fr}	Friction force of the rack
F_{spring}	Absolute force of spring
$\boldsymbol{F}_{wi}$	$i = 1, 2$ Force vectors at front wheel centers
gi	$i = 1...9$ Dimensions of simplified model, for $\boldsymbol{\Theta}_{\text{frontsusp}}$ determination
G_i	$i = 1, 2$ Bodies of simplified model, for $\boldsymbol{\Theta}_{\text{frontsusp}}$ determination
G_i	$i = a, b, c, w$ Point masses of simplified model, for $\boldsymbol{\Theta}_{\text{frontsusp}}$ determination

h	Height of CoG of Chassis in respect to $\mathcal{O}_F$
hi	$i = 1...7$ Dimensions of simplified model, for $\boldsymbol{\Theta}_{\text{rearsusp}}$ determination
h_d	Height of CoG of Chassis plus drivers in respect to $\mathcal{O}_F$
h_l	Measured height of lifted vehicle
H_i	$i = a, b, c, d, w$ Point masses of simplified model, for $\boldsymbol{\Theta}_{\text{rearsusp}}$ determination
H_1	Body of simplified model, for $\boldsymbol{\Theta}_{\text{rearsusp}}$ determination
$\boldsymbol{J}$	Jacobian matrix, Newton-Raphson method
l	Length of element
l_{spring}	Absolute length of spring
l_{damper}	Absolute length of damper
l_{arb}	Absolute length of anti roll bar
L_{0F}	Positive distance of CoG of chassis to front axle
L_{0R}	Positive distance of CoG of chassis to rear axle
L_{1F}	Horizontal, positive distance of CoG of chassis to front axle, lifted vehicle
L_{1R}	Horizontal, positive distance of CoG of chassis to rear axle, lifted vehicle
L_M	Distance between measurement point for CoG computation
L_{WB}	Wheel base
ΔL_ϵ	Maximum length change by given tolerance ϵ, *Newton-Raphson* method
m	Mass
m_i	$i = 1, 2$ Mass of front suspensions including the tires
$m_{\text{ch,drivers}}$	Mass of chassis with two drivers
$m_{\text{ch,empty}}$	Mass of chassis without drivers
m^0_{front}	Mass of front axle
m^1_{front}	Mass of front axle, lifted vehicle
$m_{\text{frontsusp}}$	Mass of front suspensions
m_{rack}	Rack mass
m^0_{rear}	Mass of rear axle
m^1_{rear}	Mass of rear axle, lifted vehicle
m_{rearsusp}	Mass of rear suspension
$m_{red,act}$	Reduced mass on the rack of electro-mechanic actuator and hang-on parts
m_{rim}	Mass of rim
m_{tire}	Mass of tire
$m_{\text{total,0}}$	Total vehicle mass
m_{wheel}	Mass of tire and rim
m_{Bi}	$i = 1, 2$ Masses of body 1 and 2
m_{Bai}	$i = 1, 2$ Masses of battery stack 1 and 2
m_{BM}	Balance mass

m_{Ci}	$i = 1, 2, 3, 4$ Mass of comparison masses
m_{E}	Mass of engine
M_u	Computation mass for steering model
$n_{elements}$	Number of elements
n_{free}	Number of free, acceptable degrees of freedom
$n_{revolutejoints}$	Number of revolute joints
$n_{slidingjoints}$	Number of sliding joints
$n_{sphericaljoints}$	Number of spherical joints
$NRMSE_{roll}$	Normalized mean square error of roll acceleration
$NRMSE_{yaw}$	Normalized mean square error of yaw acceleration
o	Dimension of planar four-bar linkage
p_{spring}	Ratio of suspension suspension attachment points
$\boldsymbol{q}$	Variable vector, Newton-Raphson method
Q_u	Computation force for steering model
$\boldsymbol{r}$	Position vector
$\boldsymbol{r}_{\mathrm{2dirvers},F}$	Position vector of two drivers
$\boldsymbol{r}_{\mathrm{Bi}}$	$i = 1, 2$ Position vector of body 1 and 2
$\boldsymbol{r}_{\mathrm{Bai}}$	$i = 1, 2$ Position vector of battery stack 1 and 2
$\boldsymbol{r}_{\mathrm{BM}}$	Position vector of balance mass
$\boldsymbol{r}_{\mathrm{Ci}}$	$i = 1, 2, 3, 4$ Position vector of comparison masses
r_x	Absolute distance in x direction between comparison masses and CoG
r_y	Absolute distance in y direction between comparison masses and CoG
$\boldsymbol{r}_{\mathrm{CoG\ empty},F}$	Center of gravity of empty chassis in respect to $\mathcal{O}_F$
$\boldsymbol{r}_{\mathrm{CoG\ driver},F}$	Center of gravity of chassis with drivers in respect to $\mathcal{O}_F$
$\boldsymbol{r}_{\mathrm{E}}$	Position vector of engine
R	Cornering radius
$R1$,$R2$	Distances of instantaneous center M
sp	Thickness of spacer, distance plate
t	time
$\boldsymbol{t}_{iu}$	$i = 1, 2$ Partial derivation vectors of front wheels positions
ΔT	Torque difference of front wheels
$\boldsymbol{T}_i$	$i = 1, 2$ Driving torque vectors at front wheel centers
$\boldsymbol{T}_{br}$	$i = 1, 2$ Braking torque vectors at front wheel centers
$\boldsymbol{T}_{pi}$	$i = 1, 2$ Torque vectors at front wheel centers
$\boldsymbol{T}_{wi}$	$i = 1, 2$ Total torque vectors at front wheel centers
u	Rack position, generalized coordinate
δ_u	Damping coefficient of the rack
$u_{conv,SbW}$	Simulated rack displacement of the standard set-up, in conventional SbW mode
u_{setup}	Simulated rack displacement of a certain set-up, in TV mode
$u_{standard}$	Simulated rack displacement of the standard set-up, in TV mode

$\boldsymbol{v}$	Velocity vector
v_{arb}	Absolute velocity of anti roll bar
v_{damper}	Absolute velocity of damper
v_{spring}	Absolute velocity of spring
v_B	Absolute velocity of point B, double wishbone suspension
$\boldsymbol{x}_1$	Part of vector $\boldsymbol{x}$
$\boldsymbol{x}_2$	Part of vector $\boldsymbol{x}$
$\boldsymbol{x}$	Solution vector for velocity computation of suspension
x, y, z	Position of wheel center of suspension
z_i	$i = 1, 2, 3, 4$ Vertical position of wheel centers of front and rear suspensions
α	Roll angle
$\alpha_k, \beta_k, \gamma_k$	*Cardan angles*
α_l	Inclination angle of lifted vehicle
$\ddot{\alpha}_{max,meas}$	Maximum roll acceleration from measurements
$\ddot{\alpha}_{max,sim}$	Maximum roll acceleration from simulations
$\ddot{\alpha}_{min,meas}$	Maximum roll acceleration from measurements
$\ddot{\alpha}_{min,sim}$	Minimum roll acceleration from simulations
β	Pitch angle
γ	Yaw angle
γ_c	Camber angle
$\gamma_{c,in}$	Initial camber angle of front wheels
$\ddot{\gamma}_{max,meas}$	Maximum yaw acceleration from measurements
$\ddot{\gamma}_{meas}$	Yaw acceleration from measurements
$\ddot{\gamma}_{min,meas}$	Maximum yaw acceleration from measurements
$\ddot{\gamma}_{sim}$	Yaw acceleration from simulations
δ	Toe angle
δ_{in}	Initial toe angle of front wheels
$\boldsymbol{\delta}_{in}$	Increment vector, Newton-Raphson method
ϵ	tolerance value, Newton-Raphson method
$\boldsymbol{\Theta}$	Moment of inertia tensor
$\boldsymbol{\Theta}_i$	$i = 1, 2$ Moment of inertia tensor of front suspension including the wheels
$\boldsymbol{\Theta}_{\text{chassis}}$	Moment of inertia tensor of chassis
$\boldsymbol{\Theta}_{\text{frontsusp}}$	Moment of inertia tensor of front suspension without wheel
$\boldsymbol{\Theta}_{\text{rearsusp}}$	Moment of inertia tensor of rear suspension without wheel
$\boldsymbol{\Theta}_{\text{rim}}$	Moment of inertia tensor of rim
$\boldsymbol{\Theta}_{\text{tire}}$	Moment of inertia tensor of tire
Θ_{xx}	Moment of inertia about x axis
Θ_{ij}	i, j=x, y, z Moment of deviation
Θ_{yy}	Moment of inertia about y axis
Θ_{zz}	Moment of inertia about z axis

$\boldsymbol{\Theta}_i^s$	$i = xx, zz$ Moment of inertia of the simplified model without the comparison masses
μ	Road friction coefficient
σ	Angle of planar four-bar linkage
σ^0	Initial angle of planar four-bar linkage
$\widehat{\sigma}$	Auxiliary angle of planar four-bar linkage
$\widehat{\sigma}^*$	Auxiliary angle of planar four-bar linkage
φ	Rotation angle of suspension arm, generalized coordinate
φ^0	Initial angle of planar four-bar linkage
$\widehat{\varphi}$	Auxiliary angle of planar four-bar linkage
ψ	Angle of planar four-bar linkage
$\boldsymbol{\psi}$	Rotation angle of wheel carrier
ψ^0	Initial angle of planar four-bar linkage
$\widehat{\psi}$	Auxiliary angle of planar four-bar linkage
$\boldsymbol{\omega}$	Angular velocity vector

Abreviations

3D	Three dimensional
4link	Four-link suspension
ARB	Anti roll bar
CAD	Computer aided design
CoG	Center of gravity
conv.	Conventional
db	Double wishbone suspension
DoG	Degrees/Degree of freedom
EPS	Electric power steering
IABG	Industrieanlagen-Betriebsgesellschaft mbH
int4	Integral IV suspension
NTC	Nardo technical center
pdb	Planar double wishbone suspension
PI	Proportional - integral
SbW	Steer-by-wire
sp	Spacer, distance plate between wheel carrier and wheel
TKP	ThyssenKrupp Presta AG
TV	Torque vectoring

1 Introduction

1.1 ThyssenKrupp Presta AG

ThyssenKrupp Presta AG (TKP) is a successful steering system manufacturers for the automotive industry because every fourth passenger car worldwide is equipped with a Presta-Steering. The main customers are major automotive manufacturer. TKP is part of the business area *Components Technology* of the ThyssenKrupp group.

TKP employs about 7,000 people in 16 countries all located around the world. The head-quarters and the main research and development department are located in Eschen, Liechtenstein and employ about 2,000 people. They have an established reputation for innovations of steering components and systems. The main products of TKP are steering columns, steering gears, column-EPS and cold forging parts. This chapter is based on [1].

1.2 Motivation

TKP conducts research in steer-by-wire (SbW) technology for the increasing automation of passenger cars. A SbW system controls the lateral vehicle dynamic by using an electric-mechanic actuator that performs the steering maneuver. These systems do not have any mechanical connection between the steering wheel and the driven wheel [24]. A position sensor at the steering wheel or joystick provides the input for the steering control unit. This steering concept requires redundant systems to achieve the high safety and reliability standards in automotive industry. Therefore, torque vectoring (TV) can be used as a backup system in the case of a breakdown of the electro-mechanic actuator. A TV steering is using a torque difference at the steered wheels to perform the desired steering maneuver. Some advantages of SbW are to improve the safety by using advanced driver assistance systems, variable steering feel and steering functions. Another important benefit is the additional freedom in vehicle design, because there is no intermediate steering shaft as a mechanical connection needed. The required torque difference for the TV mode to control the vehicle depends on the suspension, drive train, vehicle dimensions and much more.

First, the aim of this thesis is to build up a simulation environment for a SbW TV vehicle, which is based on a prototype vehicle from TKP.
To accomplish this goal, the vehicle parameters have to be identified and suspension

models have to be build up for a virtual vehicle model. This model has to be validated by the use of measurement data from test drives.
The second part of this thesis is to analyze the impact of the suspension kinematic and basic vehicle parameters on the TV steering. These setting have to be evaluated by vehicle dynamic simulation of certain driving maneuvers.
Finally, the steering and driving behavior as well as the efficiency of the TV steering of these settings will be analyzed.

1.3 Test vehicle

The prototype research vehicle is a BMW X5 e70 2007 model and is depicted in Figure 1.1. The BMW X5 was refitted to an electrically powered vehicle by students from the ETH Zurich as part of the research project SUNCAR[23]. They removed the combustion engine with all hang-on parts and replaced it with two electric engines for each front wheels. Additionally, on each engine is a gearbox mounted to get the required transmission ratio. They mounted one accumulator battery stack instead of the back seats and one at the underbody for the power supply.

Figure 1.1: BMW X5 e70, electrically powered prototype vehicle

Furthermore, they extended the steering system by a SbW steering. Therefore, the BMW X5 can be driven as a conventional car with a mechanical connection between the steering wheel and the wheels or in two SbW modes. The first one is a conventional

SbW mode which is using an electro-mechanic actuator to drive the steering gear. The second one is the TV mode which is using a torque difference on the front wheels to drive the steering gear.

This prototype vehicle is equipped with sensors to measure the state of the vehicle, wheels, steering wheel and rack, suspension, engine and applied steering wheel torques. Table 1.1 shows basic informations of the electrical powered prototype vehicle.

Table 1.1: BMW X5 prototype vehicle, basic informations

Power train	
Engine	Two electrical motors, *Bruse HSM1-10.18.13* for each front wheel one
Max. power of one engine	140 kW (360 V)
Continuous power of one engine	84 kW (360 V)
Max. torque at max inverter current of one engine	305 Nm
Max. engine speed of one engine	13000 rpm
Max. torque at each wheel(of one engine)	1680 Nm
Total gearbox ratio	1:5.5
Overall	
Wheel base	2.933 m
Track width (front/rear)	1.644 m/1.65 m
Vehicle weight	2659 kg
Vehicle weight of an original BMW X5	2185 kg
Suspension	
Front suspension	*Four-link* suspension
Rear suspension	*Integral IV* suspension
Tire	*Uniroyal Rainsport3 P255/50 R19*

1.4 Test drive

The test drives for the model validation in Chapter 3 were done at the Nardo Technical Center (NTC) Porsche in Nardo, Italy and is depicted in Figure 1.2.
The test vehicle was equipped with a couple of sensors which recorded measurement data. The relevant sensors for this work are listed in Table 1.2, as well as the wheel load scale for the determination of the vehicle and wheel weights.

Table 1.2: Sensors and measurement equipment

Sensor list:	
Position of front wheels	Wheelvector sensor, *Kistler RV-4 Radvektor-Sensoren*
Deflection of rear suspension	Linear potentiometer, *Novotechnik TEX-0100-415-002-205*
Acceleration and yaw, roll, pitch rate sensor	*Racelogic VBOX IMU04*
Velocity in x- and y- direction	Contactless optical sensor, *Correvit S-350*
Portable wheel load scale	Four scales, *RW8.1 HKM Messtechnik*

Figure 1.2: NTC Porsche in Nardo, Italy [12]

1.5 Steering by torque vectoring

Torque vectoring(TV) means the individual torque distribution on the wheels. It can be either the braking or the driving torque. An example for braking torque distribution is *electronic stability control* (ESC), which applies the brakes to stabilize the vehicle when the drives loses control of it [24].
Torque vectoring can be also used as a redundant steering for SbW vehicle [19] and is the focus of this thesis. The prototype vehicle has a front wheel steering and front wheel drive. The basic investigations will be done for this vehicle system. A four wheel drive or an additional rear wheel steering would increase the possibilities of a torque vectoring steered vehicle but it is not a part of this thesis.
The present thesis deals with two different steering concepts. The first one is a conventional front wheel steering of the BMW X5 and the second one is the TV steering. The front wheels are still connected by tie rods and the rack but the rack position is not fixed and no external actuator is driving it. A certain road wheel angle will be generated just depending on the applied torque difference and the vehicle state. The control unit has to distribute the front wheel torques to ensure the desired lateral and longitudinal driving behavior.

1.6 Coordinate systems and definitions

The inertial coordinate system $\mathcal{O}_0$ lies in the reference ground plane and according to ISO 8855 the vehicle fixed coordinate system $\mathcal{O}_F$ is located in the center of gravity of the vehicle, Figure 1.3. But here the vehicle fixed system $\mathcal{O}_F$ is attached to the center

of the front axle, because this point does not change its position for different loads [21]. Therefore, the position of $\mathcal{O}_0$ is indicated by 0 and $\mathcal{O}_F$ by F. The *Cardan angles* α_k,β_k and γ_k define the orientation of the inertial coordinate system $\mathcal{O}_0$ to the vehicle fixed coordinate system $\mathcal{O}_F$. The front left wheel coordinate system $\mathcal{O}_1$ is located in the wheel

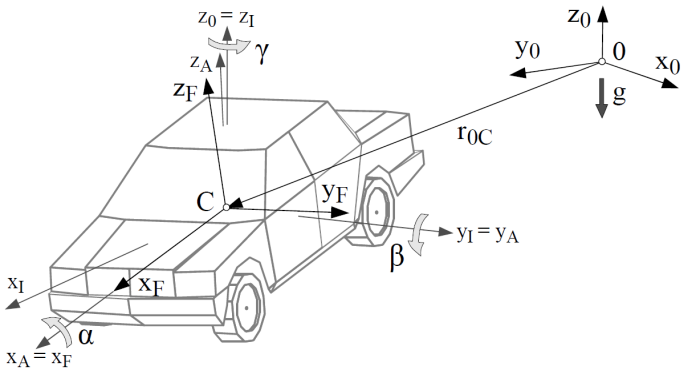

Figure 1.3: Cooridnate system of vehicle body, grafic from [21]

center. The position of the wheel center is given by

$$\boldsymbol{r}_{01,0} = \boldsymbol{r}_{0F,0} + \boldsymbol{r}_{F1,0} \tag{1.1}$$

and the wheel center is given by the point M, depicted in Figure 1.4. The wheel center at the present thesis is indicated by the latter w. Additionally, the vehicle fixed coordinate system lies in this figure in the center of gravity of the vehicle instead of the center of the front axle.

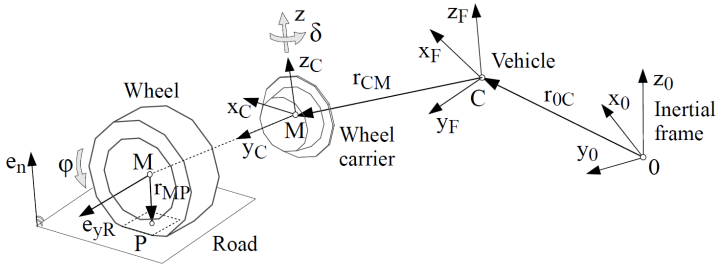

Figure 1.4: Cooridnate system of wheel, grafic from [21]

2 Vehicle model

In the field of vehicle dynamic simulation, there are many different approaches and methods. One key task is to build up a model which is simple as possible and accurate as necessary in order to meet the requirements. Simplifications in the process of modeling have to be done and this short list provides some methods and respective application fields.

- **Single track model**
  A single track model is based on many simplifications, for example it has only one single tire on each axle. It allows a physically plausible description of the driving behavior of vehicles with less parameterization effort.[24] The difference between a linear and a nonlinear single track model is the linear or nonlinear tire model. A nonlinear single track model can be used for real time applications for the SbW control unit. [16]
- **Multi-body system vehicle model**
  The classic approach in multi-body simulation for complex system is to use mostly rigid bodies with mass and massless connection elements. A full multi-body system vehicle model can consist of the vehicle framework, optional separate modules for steering system, drive train, tires, load, passengers, seats and an engine.[21]
- **Multi-body system vehicle model with elasto-kinematics**
  The assumption to have only rigid elements in the vehicle can simplify the process of modeling and computation. It is more complicated to consider the elastic behavior of the bodies and the joints [22]. For example, the suspension can contain elastic bushings or the frame of the vehicle can deform its shape at dynamic maneuvers. Joints can be approximated by spring and damper elements. For closer investigations, the finite element method can be used to describe the elastic and plastic characteristics of mechanical systems in order to determine the deformation and stress distribution due to external forces on a body.

The present thesis uses a three-dimensional multi-body vehicle model without elasto-kinematics behavior, neither at the suspensions nor at the frame.

2.1 Multi-body vehicle model

The model for the vehicle dynamic simulation is based on a full multi-body system vehicle model from Professor *Georg Rill*, from OTH Regensburg. The equations, formalism

and notation are based on [21] and [20]. These books provide further information about this model and more detailed background as well.
This vehicle model had to be extended with more detailed suspension models to characterize the kinematic movement. Additionally, a steering model has to be implemented for the torque vectoring investigations. This chapter illustrates assumptions, simplifications and background information for this full multi-body system vehicle model.

Methods

Common methods for multi-body simulations are the method of *Newton Euler*, the principle of *Jourdain*, the principle of *D'Alembert* and *Lagrange* equations of the second kind. [5].
The *Lagrange* equations of the second kind, *Jourdain* and *D'Alembert* equations are avoiding constraint-forces and torques. These equations lead to a minimal number of differential equations of generalized coordinates [22]. The principle of *D'Alembert* and *Jourdain* are comparable and easy to automate. That is a reason why the majority of commercial multi-body simulation tools as well as *Georg Rills* vehicle model are using these methods [21]. The basics of the principle of *Jourdain* are provided from Equation 2.1 to 2.7.

The *D'Alembert* principle states that the virtual work of all constraint-forces and constraint-torques is zero.
Compared to *D'Alembert*, *Jourdain's* principle states that the virtual power of all constraint-forces and constraint-torques is zero. A system with n bodies leads to the Equation 2.1 by using *Jourdain's* formalism.

$$\sum_{i=1}^{k} \left\{ \delta \dot{\boldsymbol{r}}_{0i,0}^{T} \; \boldsymbol{F}_{i,0}^{z} + \delta \dot{\boldsymbol{\psi}}_{0i,0}^{T} \boldsymbol{T}_{i,0}^{z} \right\} = 0 \tag{2.1}$$

The normal form of vectors are columns vectors. Therefore, the result of Equation 2.1 for each indices i is a scalar. $\boldsymbol{F}_{i,0}^{z}$ and $\boldsymbol{T}_{i,0}^{z}$ are constraint-forces and constraint-torques. They are given by

$$m_i \; \ddot{\boldsymbol{r}}_{0i,0} = \boldsymbol{F}_{i,0}^{z} + \boldsymbol{F}_{i,0}^{e} \tag{2.2}$$

and

$$\boldsymbol{\Theta}_{Si,0} \; \ddot{\boldsymbol{\psi}}_{0i,0} + \dot{\boldsymbol{\psi}}_{0i,0} \times \boldsymbol{\Theta}_{Si,0} \; \dot{\boldsymbol{\psi}}_{0i,0} = \boldsymbol{T}_{i,0}^{z} + \boldsymbol{T}_{i,0}^{e}. \tag{2.3}$$

m_i... is the mass of body i
$\boldsymbol{\Theta}_{Si,0}$... is the moment of inertia tensor with respect to center of gravity of body i
$\boldsymbol{F}_{i,0}^{e}$ and $\boldsymbol{T}_{i,0}^{e}$ ... are the internal forces and torques
$\boldsymbol{F}_{i,0}^{z}$ and $\boldsymbol{T}_{i,0}^{z}$ ... are the constraint forces and torques

The virtual velocities have to be consistent with the kinematic constraints and are given by

$$\delta \dot{\boldsymbol{r}}_{0i,0} = \frac{\partial \dot{\boldsymbol{r}}_{0i,0}(x, \dot{x})}{\partial \dot{x}} \delta \dot{x} \tag{2.4}$$

and the virtual angular velocities are given by

$$\delta\dot{\boldsymbol{\psi}}_{0i,0} = \frac{\partial\dot{\boldsymbol{\psi}}_{0i,0}(x,\dot{x})}{\partial\dot{x}}\delta\dot{x}. \tag{2.5}$$

x is the generalized coordinate and $\dot{x}$ its time derivation. The equation of motion can be found by using the assumption $\delta\dot{x} \neq 0$ and factor out the virtual coordinate $\delta\dot{x}$ in Equation 2.1.
According to [5] the partial derivation can be replaced by

$$\frac{\partial\dot{\boldsymbol{r}}_{i,0}}{\partial\dot{x}} = \frac{\partial\boldsymbol{r}_{i,0}}{\partial x} \tag{2.6}$$

and

$$\frac{\partial\dot{\boldsymbol{\psi}}_{i,0}}{\partial\dot{x}} = \frac{\partial\boldsymbol{\psi}_{i,0}}{\partial x} \tag{2.7}$$

and converts *Jourdain's* equation to *D'Alembert's* equation [20].

Full Vehicle model

Two different vehicle models are used within this thesis. One of them is for a conventional SbW vehicle and the other one for a TV steered vehicle. The Table 2.1 compares the key data

Table 2.1: Comparisson of vehicle models

Conventional SbW	**Torque vectoring**
Degrees of freedom (DoF)	
In total 26 DoF: 3 DoF for the position and 3 DoF for the orientation of the chassis, 4 DoF for the rotation angles of the wheels, 4 DoF for the suspension deflections and 3×4 DoF for the tire states for each tire	In total 27 DoF: 26 DoF of the conv. SbW vehicle plus 1 DoF for the rack position
Input parameter	
Rack position u Desired velocity v_{des} Braking torques $\boldsymbol{T}_{br}$	Driving torques $\boldsymbol{T}_1$ and $\boldsymbol{T}_2$ Desired velocity v_{des} Braking torques $\boldsymbol{T}_{br}$

$\boldsymbol{T}_1$ and $\boldsymbol{T}_2$ are the driving torque vectors at the front left and right wheel. v_{des} indicates the desired velocity and an integrated controller adds the required driving torques to $\boldsymbol{T}_1$ and $\boldsymbol{T}_2$. The 4×1 vector $\boldsymbol{T}_{br}$ provides the absolute braking torques for each wheel.

Suspension

Three-dimensional suspension models are kinematic chains with one DoF for the deflection movement and one more for the steering movement, in case of a steered suspension. Not for every kinematic chain does an analytic solution exist and it might not allow unrestricted movements. Fortunately, the suspension movement is limited by the displacement of the spring and damper. The model has to be valid only in this certain area. The requirements for suspension modeling are to describe the kinematic movement and velocity of the wheel center as well as of each additional part like the spring and damper. The applied *Jourdain's* method requires for each DoF one generalized coordinate and it is necessary to describe the change of the position and velocity in respect to these coordinates.

Newton-Raphson method

One way to solve nonlinear equations is the *Newton-Raphson* iteration method. According to *Reza N. Jaza*, it is the most common one and the complete algorithm and examples are provided in [13]. The required part of the algorithm is denoted from Equation 2.8 to 2.15.
For a set of nonlinear equations

$$\boldsymbol{f}(q) = \begin{bmatrix} f_1(q_1, q_1, ..., q_n) \\ f_2(q_1, q_1, ..., q_n) \\ ... \\ f_n(q_1, q_1, ..., q_n) \end{bmatrix}, \tag{2.8}$$

with the variable vector $\boldsymbol{q}$

$$\boldsymbol{q}^T = \begin{bmatrix} q_1 & q_2 & ... & q_n \end{bmatrix}, \tag{2.9}$$

is the Jacobian matrix $\boldsymbol{J}$ defined as

$$\boldsymbol{J} = \left[\frac{\partial \boldsymbol{f_i}}{\partial \boldsymbol{q_j}} \right]. \tag{2.10}$$

The iteration formula for $\boldsymbol{q}^{i+1}$ is defined as

$$\boldsymbol{q}^{i+1} = \boldsymbol{q}^i - \boldsymbol{J}^{-1}(\boldsymbol{q}^i)\ \boldsymbol{f}(\boldsymbol{q}^i). \tag{2.11}$$

The iteration starts with the guess of

$$\boldsymbol{q}^i = \boldsymbol{q}^0 \tag{2.12}$$

and computes $\boldsymbol{q}^{i+1}$ by applying Equation 2.11. The next step is to find the increment $\boldsymbol{\delta}^i_{in}$ with

$$\boldsymbol{\delta}^i_{in} = \boldsymbol{q}^{i+1} - \boldsymbol{q}^i. \tag{2.13}$$

If the absolute value of $|\boldsymbol{\delta}^i_{in}|$ is smaller as a defined tolerance ϵ, then the solution is given by

$$\boldsymbol{q} = \boldsymbol{q}^{i+1}. \tag{2.14}$$

Otherwise the iteration has to be done again, until

$$|\boldsymbol{\delta}_{in}^{i}| < \epsilon. \tag{2.15}$$

2.2 Tires

Modern tires are made out of rubber, fabric and steel. The deformation of a tire on the road creates the contact patch, where the normal and friction forces are transmitted. A force and a torque vector in a specific point at the contacted patch can describe the contact force [21].

Tire models for vehicle dynamic studies can be based on the physical nature of the tire or just empirical or a combination of them, the so called semi empirical tire models. The aim is to describe the tire behavior and the generated forces and torques [17]. The tire model for this multi-body vehicle model is *TMeasy*, a semi-empirical model, which is able to take the tire dynamic into account. Other models are for example the *TMsimple* model which was used in [16] or the *Pacejka magic formula* tire model.

2.3 Front suspension

At the front axle of the BMW X5 e70 is a *four-link* suspension and is depicted in Figure 2.1. The approach of suspension modeling at the present thesis is to create one simplified version, with an analytic solution and one version where each joint and link are considered. The aim of this approach is to be as simple as possible and as accurate as necessary, to avoid high computation time and to focus on the basic relationships in vehicle dynamics.
One assumption is that the compliance or elasto-kinematics are not taken into account, therefore, all links are stiff and the joints are either revolute, spherical or sliding joints. The real suspension has a couple of elastic bushings and links. It is possible to model the elasto-kinematics but it will increase the computation time [20]. One benefit of a stiff model without elasto-kinematics is that the state of the suspension model is only a function of the deflection and steering motion. Furthermore, there is no guarantee to increase the model quality if only the elasto-kinematics of the suspension is considered but not the elasticity of other elements or inaccurate identified parameters. It is similar to a chain, the whole model is just as good as the weakest link [20].

According to the BMW X5 suspension manual [3] the *four-link* front suspension is similar to a *double wishbone* suspension. Instead of a lower control arm the BMW X5 e70 suspension has two separate links, Figure 2.1
For this reason, the simplified model is a *double wishbone* suspension and the accurate

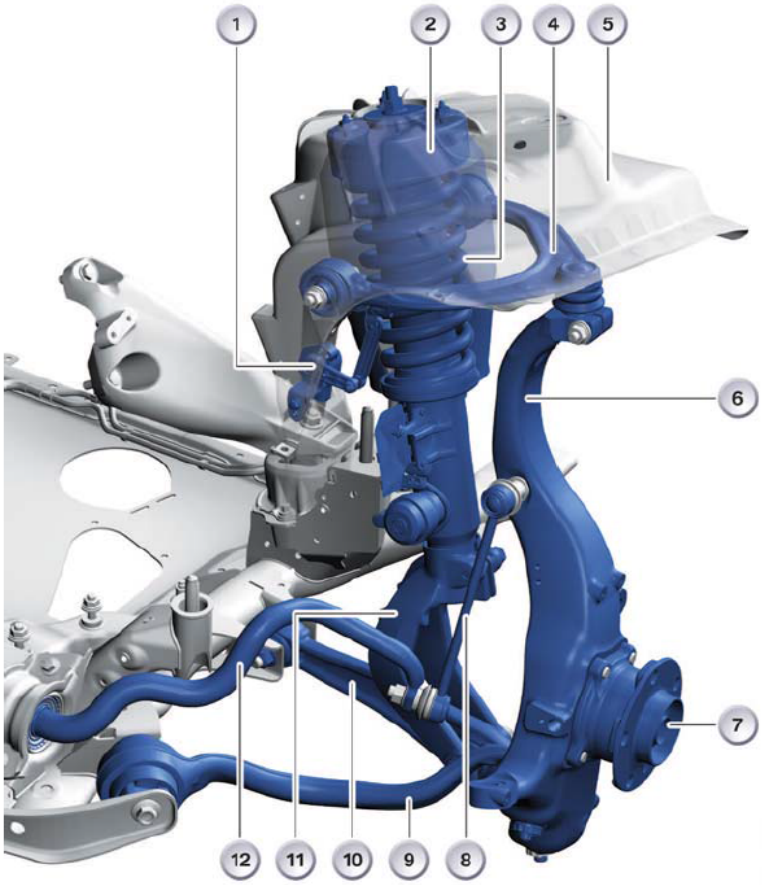

Figure 2.1: Front *four-link* suspension of BMW X5 e70[3], 1 = Level sensor, 2 = Strut bearing, 3 = Suspension strut, 4 = Upper control arm, 5 = Chassis,6 = Wheel carrier, 7 = Wheel bearing, 8 = Torque roll restrictor, 9 = Trailing arm, 10 = Lower wishbone, 11 = Suspension fork, 12 = Anti-roll-bar

one is the *four-link* suspension. The following subsections explain the models and the computation of the kinematic movement.

- **Simple model:** *Double wishbone* suspension
- **Advanced model:** *Four-link* suspension

In Chapter 3 the model validation is described and the pros and cons are pointed out. This Section 2.3 considers only the front left suspension. The modeling and equations are equal for the right side, except of the geometrical connection points, because they have to be mirrored.

Model

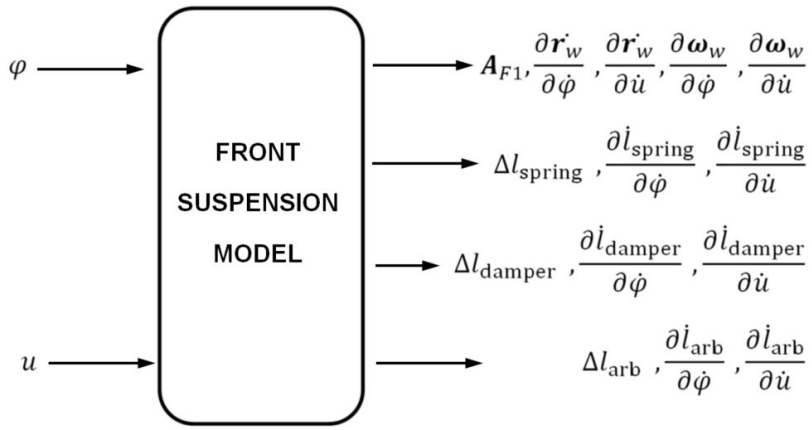

Figure 2.2: General in- and out-put of a front suspension model

The front suspension model can be considered as a black box, Figure 2.2. The input variables are the generalized coordinates φ and u. The output variables are the position of the wheel center $\boldsymbol{r}_{w,F}$, the transformation matrix $\boldsymbol{A}_{F1}$ from wheel carrier coordinate system $\mathcal{O}_1$ to the vehicle fixed coordinate system $\mathcal{O}_F$, the partial derivation of the wheel center vector by the generalized coordinates $\frac{\partial \dot{\boldsymbol{r}}_{w,1}}{\partial \dot{\varphi}}$ and $\frac{\partial \dot{\boldsymbol{r}}_{w,1}}{\partial \dot{u}}$ as well as the partial derivation of the rotation $\frac{\partial \boldsymbol{\omega}_{w,1}}{\partial \dot{\varphi}}$ and $\frac{\partial \boldsymbol{\omega}_{w,1}}{\partial \dot{u}}$. $\boldsymbol{\omega}$ is the time derivation of the rotation vector $\boldsymbol{\psi}$. In addition, the spring, damper and anti-roll-bar length changes are output variables as well as their partial derivations.

2.3.1 Double wishbone suspension

The kinematics of a *double wishbone* suspension is explained in the book [21] from *Georg Rill*. The spring damper element is attached to the lower control arm and the anti-roll-bar at the wheel carrier.

Degrees of freedom

The determination of the DoF is done in the same way like *Wolfgang Matschinsky* [15]. This suspension is made of five elements which affect the kinematic movement. These elements are the upper and lower control arm, tie rod, rack and wheel carrier. Each one has six DoF and a couple of constraints. A revolute joint reduces it by five DoF and a spherical joint reduces it by three and a sliding joint by five.
Additionally, there are some DoF which do not affect the kinematic movement, for example, the self rotation of the tie rod about its rod axis. The remaining numbers of DoF are given by

$$DoF = 6\ n_{elements} - 3\ n_{sphericaljoints} - 5\ n_{slidingjoints} - 5\ n_{revolutejoints} - n_{free} \quad (2.16)$$

This *double wishbone* suspension has five elements, four spherical joints, one sliding joint of the rack, two revolute joints of the wishbones and the tie rod, which can rotate about their own rod axis.

The number of elements is five, of spherical joints four, of sliding joints one, of revolute joints two and the number of free DoF is one. This leads to

$$DoF = 6 \cdot 5 - 3 \cdot 4 - 5 \cdot 1 - 5 \cdot 2 - 1 = 2, \tag{2.17}$$

and therefore, two generalized coordinates are required. One of them is the rotation angle about the lower control arm φ and the other one is the steering movement of the rack u. In general, the generalized coordinate can be chosen freely but they have to be independent of each other.

Computation of position

The position of each point i at the wheel carrier can be determined by

$$\boldsymbol{r}_{i,F}^{1} = \boldsymbol{r}_{w,F}^{0} + \boldsymbol{A}_{F1}\ \boldsymbol{r}_{wi,1} \tag{2.18}$$

$\boldsymbol{r}_{w,F}^{1}$ is the computated position of the wheel center w and $\boldsymbol{A}_{F1}$ the transformation matrix from the wheel carrier to the vehicle fixed system and given in [21]. $\boldsymbol{r}_{wi,F}$ is the distance vector from the wheel center to any point i, which can be either point c, q or v, Figure 2.3.

Computation of velocity

The actual velocity can be calculated with Equation 2.19.

$$\boldsymbol{v}_{w,F} = \frac{\partial \dot{\boldsymbol{r}}_{w,F}}{\partial \dot{\varphi}} \dot{\varphi} + \frac{\partial \dot{\boldsymbol{r}}_{w,F}}{\partial \dot{u}} \dot{u} \tag{2.19}$$

By using Equation 2.6 and 2.7 the velocity can be noted in the form

$$\boldsymbol{v}_{w,F} = \frac{\partial \boldsymbol{r}_{w,F}}{\partial \varphi} \dot{\varphi} + \frac{\partial \boldsymbol{r}_{w,F}}{\partial u} \dot{u}. \tag{2.20}$$

The actual angular velocity of the wheel center is given by

$$\boldsymbol{\omega}_{w,F} = \frac{\partial \boldsymbol{\omega}_{w,F}}{\partial \dot{\varphi}} \dot{\varphi} + \frac{\partial \boldsymbol{\omega}_{w,F}}{\partial \dot{u}} \dot{u}. \tag{2.21}$$

By using Equation 2.6 and 2.7 the angular velocity can be written as

$$\boldsymbol{\omega}_{w,F} = \frac{\partial \boldsymbol{\psi}_{w,F}}{\partial \varphi} \dot{\varphi} + \frac{\partial \boldsymbol{\psi}_{w,F}}{\partial u} \dot{u} \tag{2.22}$$

Force elements

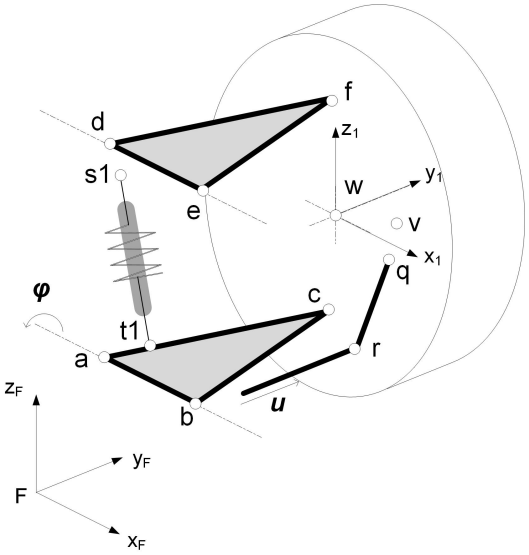

Figure 2.3: *Double wishbone* suspension model of BMW X5 e70

The spring-damper element is attached to the lower control arm and to the chassis. Hence, the velocity and length change of the damper and the spring are the same:

$$\Delta l_{\text{spring}} = \Delta l_{\text{damper}} \tag{2.23}$$

$$v_{\text{spring}} = v_{\text{damper}} \tag{2.24}$$

Therefore, the length change due to φ is given by

$$\Delta l_{\text{spring}} = |\boldsymbol{r}^1_{s1t1,F}| - |\boldsymbol{r}^0_{s1t1,F}| \tag{2.25}$$

$$\boldsymbol{r}^1_{s1t1,F} = \boldsymbol{r}^1_{t1,F} - \boldsymbol{r}^1_{s1,F} \tag{2.26}$$

$$\boldsymbol{r}^0_{s1t1,F} = \boldsymbol{r}^0_{t1,F} - \boldsymbol{r}^0_{s1,F} \tag{2.27}$$

The rack displacement does not affect the lower control arm. Therefore, the absolute velocity of the spring damper element due to $\dot{\varphi}$ is given by

$$v_{\text{spring}} = \frac{\partial l_{\text{spring}}}{\partial \varphi} \dot{\varphi} \tag{2.28}$$

The anti-roll-bar is attached to the wheel carrier. A simplification to determine the length change of the anti-roll-bar is to take only the z-direction of the attachment point $\boldsymbol{r}_{v,F}$ into account

$$\Delta l_{\text{arb}} = r^1_{v,F}(3) - r^0_{v,F}(3) \tag{2.29}$$

and the velocity due to $\dot{\varphi}$ and $\dot{u}$ is given by

$$v_{\text{arb}} = \frac{\partial l_{\text{arb}}}{\partial \varphi}\dot{\varphi} + \frac{\partial l_{\text{arb}}}{\partial u}\dot{u} \tag{2.30}$$

The spring force can be calculated with

$$F_{\text{spring}} = c_s(l_{\text{spring}})\ \Delta l_{\text{spring}}. \tag{2.31}$$

In general, the spring rate c_s is dependent on the length change Δl_{spring}. And the damper force is given by

$$F_{\text{damper}} = d_d(v_{\text{damper}})\ v_{\text{damper}} \tag{2.32}$$

and the damper coefficient d_d is dependent on the velocity v_{damper} in the damper axis. The bump stop is located at the damper and approximated by a nonlinear spring. The bump stop force F_{bs} depends on the spring rate c_d and is given by

$$F_{\text{bs}} = c_d(l_{\text{damper}})\ \Delta l_{\text{damper}} \tag{2.33}$$

The anti-roll-bar force is given by the linear equation

$$F_{\text{arb}} = c_{\text{arb}}\ \Delta l_{\text{arb}} \tag{2.34}$$

The anti-roll-bar rate is c_{arb} is approximated by a constant value, because the anti-roll-bar has a consistent and simple structure.

2.3.2 Four-link suspension

The *four-link* suspension model consists of one upper control arm and to separate links instead of the lower control arm. The spring damper element is attached to the lower wishbone and to the anti-roll-bar at the wheel carrier.

Degrees of freedom

The determination of the DoF is done in the same way like in Subsection 2.3.1. This suspension is made of six elements which affect the kinematic movement. This elements are the upper control arm, wishbone, trailing arm, tie rod, rack and wheel carrier. Each one has six DoF and a couple of constraints. It has seven spherical joints, one sliding joint at the rack, one revolute joint at the upper control arm and three links which can rotate about their rod axis.
This leads to

$$DoF = 6 \cdot 6 - 3 \cdot 7 - 5 \cdot 1 - 5 \cdot 1 - 3 = 2 \tag{2.35}$$

and therefore two generalized coordinates are required. One of them is the rotation angle about the upper control arm φ and the other one is the steering movement of the rack

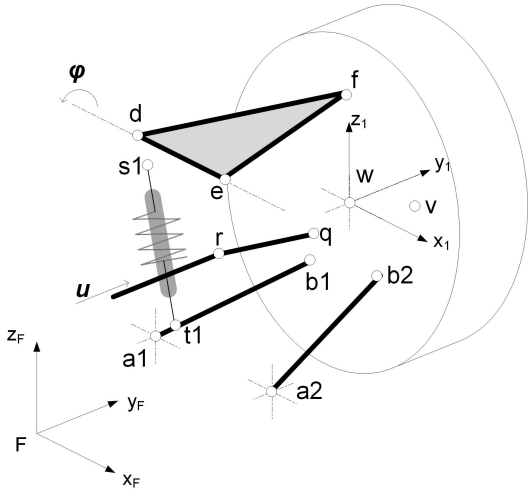

Figure 2.4: *Four-link* suspension model of BMW X5 e70

u.

Computation of position

The suspension can be considered as a closed kinematic chain. The model is depicted in Figure 2.4.
The approach is to set up equations for kinematic chains of the suspension. The aim is to determine the position of all elements for a given rotation angle φ and a rack position u. It is enough to compute the orientation of the wheel carrier, because it defines the position of the remaining elements. The wheel carrier has in general six DoF.
The rotation angle φ defines the position of the upper control arm and therefore of the connection point f, Figure 2.4. Hence, only three rotational DoF remains and can be described by the *Cardan angles* α_k, β_k and γ_k. The aim is to define three loop equations to determine the three missing angles. These equations have to be independent on each other. An explicit solution of these angle was found for the *double wishbone* suspension [21], but for the link-four suspension no explicit solution could be found.

Position of wheel center:

The aim of the first part is to determine the position of the wheel carrier center $\boldsymbol{r}_{w,F}$ and the transformation matrix A_{F1}. The position vector $\boldsymbol{r}^1_{f,F}$ can be calculated with

$$\boldsymbol{r}^1_{f,F}(\varphi) = \boldsymbol{r}^0_{d,F} + \boldsymbol{A}_\varphi \boldsymbol{r}^0_{df,F}. \tag{2.36}$$

The vector $\boldsymbol{r}^0_{d,F}$ is fixed to the chassis, $\boldsymbol{A}_\varphi$ is the rotation matrix about the axis $\boldsymbol{e}_{de,F}$ and $\boldsymbol{r}^0_{df,F}$ is the initial vector from point d to f, depicted in Figure 2.4, and denoted as

$$\boldsymbol{r}^0_{df,F} = \boldsymbol{r}^0_{f,F} - \boldsymbol{r}^0_{d,F}. \tag{2.37}$$

The matrix $\boldsymbol{A}_\varphi$ describes a rotation about the axis

$$\boldsymbol{e}_{de,F} = \frac{\boldsymbol{r}^0_{e,F} - \boldsymbol{r}^0_{d,F}}{|\boldsymbol{r}^0_{e,F} - \boldsymbol{r}^0_{d,F}|} \tag{2.38}$$

and the matrix $\boldsymbol{A}_\varphi$ is given by

$$\boldsymbol{A}_\varphi = \boldsymbol{e}_{de,F}\ \boldsymbol{e}^T_{de,F} + (\boldsymbol{E} - \boldsymbol{e}_{de,F}\ \boldsymbol{e}^T_{de,F})\ \cos(\varphi) + \tilde{\boldsymbol{e}}_{de,F}\ \sin(\varphi). \tag{2.39}$$

$\boldsymbol{E}$ is a 3x3 matrix of identity and the skew-symmetric matrix $\tilde{e}_{de,F}$ is defined by

$$\tilde{\boldsymbol{e}}_{de,F} = \begin{bmatrix} 0 & -e_{de,F}(3) & e_{de,F}(2) \\ e_{de,F}(3) & 0 & -e_{de,F}(1) \\ -e_{de,F}(2) & e_{de,F}(1) & 0 \end{bmatrix}, \tag{2.40}$$

the vector $\boldsymbol{r}^1_{f,F}$ defines one point of the wheel carrier after a certain movement of the upper control arm by a rotation of φ. The three remaining rotation DoF are dependent on constraints. Therefore, three equations are required. There are many different approaches to find a solution. For example, the cartesian coordinates of certain points can be used, like in Subsection 2.4.2, for the *integral IV* rear suspension. But the applied method is to define a rotation in form of the *Cardan angles* α_k, β_k and γ_k. This leads to the matrix

$$\boldsymbol{A}_{\text{cardan}}(\alpha_k, \beta_k, \gamma_k) = \boldsymbol{A}_{\alpha_k}\ \boldsymbol{A}_{\beta_k}\ \boldsymbol{A}_{\gamma_k} \tag{2.41}$$

with

$$\boldsymbol{A}_{\alpha_k} = \begin{bmatrix} 1 & 0 & 0 \\ 0 & \cos\ \alpha_k & -sin\ \alpha_k \\ 0 & \sin\ \alpha_k & \cos\ \alpha_k \end{bmatrix}, \tag{2.42}$$

$$\boldsymbol{A}_{\beta_k} = \begin{bmatrix} \cos\ \beta_k & 0 & \cos\ \beta_k \\ 0 & 1 & 0 \\ -sin\ \beta_k & 0 & \cos\ \beta_k \end{bmatrix}, \tag{2.43}$$

and

$$\boldsymbol{A}_{\gamma_k} = \begin{bmatrix} \cos\ \gamma_k & -sin\ \gamma_k & 0 \\ \sin\ \gamma_k & \cos\ \gamma_k & 0 \\ 0 & 0 & 1 \end{bmatrix}. \tag{2.44}$$

The matrix $\boldsymbol{A}_{\text{cardan}}$ is the transformation matrix from the left wheel carrier fixed coordinate system $\mathcal{O}_1$ to vehicle fixed coordinate system $\mathcal{O}_F$ and can be written as

$$\boldsymbol{A}_{F1} = \boldsymbol{A}_{\text{cardan}}. \tag{2.45}$$

The required condition for the three loop equations is that the length of the lower links and the rod are constant. The initial vectors of the links are defined by

$$\boldsymbol{r}^0_{a1b1,F} = \boldsymbol{r}^0_{b1,F} - \boldsymbol{r}^0_{a1,F}, \tag{2.46}$$

$$\boldsymbol{r}^0_{a2b2,F} = \boldsymbol{r}^0_{b2,F} - \boldsymbol{r}^0_{a2,F}, \tag{2.47}$$

and

$$\boldsymbol{r}^0_{rq,F} = \boldsymbol{r}^0_{q,F} - \boldsymbol{r}^0_{r,F}. \tag{2.48}$$

The lengths of the links are given by

$$l^0_{a1b1} = |\boldsymbol{r}^0_{a1b1,F}|, \tag{2.49}$$

$$l^0_{a2b2} = |\boldsymbol{r}^0_{a2b2,F}|, \tag{2.50}$$

and

$$l^0_{rq} = |\boldsymbol{r}^0_{rq,F}|. \tag{2.51}$$

The vectors of the links after a rotation angle φ and a displacement u of the rack, are denoted as

$$\boldsymbol{r}^1_{a1b1,F} = \boldsymbol{r}^1_{f,F}(\varphi) + \boldsymbol{A}_{F1}(\alpha_k, \beta_k, \gamma_k)\ \boldsymbol{r}_{fb1,1} - \boldsymbol{r}^0_{a1,F}, \tag{2.52}$$

$$\boldsymbol{r}^1_{a2b2,F} = \boldsymbol{r}^1_{f,F}(\varphi) + \boldsymbol{A}_{F1}(\alpha_k, \beta_k, \gamma_k)\ \boldsymbol{r}_{fb2,1} - \boldsymbol{r}^0_{a2,F}, \tag{2.53}$$

and

$$\boldsymbol{r}^1_{rq,F} = \boldsymbol{r}^1_{f,F}(\varphi) + \boldsymbol{A}_{F1}(\alpha_k, \beta_k, \gamma_k)\ \boldsymbol{r}_{fq,1} - \boldsymbol{r}^0_{a1,F} - \boldsymbol{r}^1_{r,F}(u). \tag{2.54}$$

The vector $\boldsymbol{r}^1_{r,F}$ is shifted in y-direction by the second generalized coordinate u and is defined by

$$\boldsymbol{r}^1_{r,F}(u) = \boldsymbol{r}^0_{r,F} + \begin{bmatrix} 0 \\ u \\ 0 \end{bmatrix} \tag{2.55}$$

and the lengths of the links can be determined by the norm of the vectors and are given by

$$l^1_{a1b1} = |\boldsymbol{r}^1_{a1b1,F}|, \tag{2.56}$$

$$l^1_{a2b2} = |\boldsymbol{r}^1_{a2b2,F}|, \tag{2.57}$$

and

$$l^1_{rq} = |\boldsymbol{r}^1_{rq,F}|. \tag{2.58}$$

The three nonlinear loop equations are

$$l^1_{a1b1} - l^0_{a1b1} = 0, \tag{2.59}$$

$$l^1_{a2b2} - l^0_{a2b2} = 0, \tag{2.60}$$

and

$$l^1_{rq} - l^0_{rq} = 0 \tag{2.61}$$

and the approximated solution can be found by applying the *Newton-Raphson* method by using the Equations 2.8 to 2.12. The variable vector $\boldsymbol{q}$ from Equation 2.8 is

$$\boldsymbol{q}^T = \begin{bmatrix} \alpha_k & \beta_k & \gamma_k \end{bmatrix} \tag{2.62}$$

and the vector $\boldsymbol{f}$ which contains the sets of nonlinear equations is

$$\boldsymbol{f}(q) = \begin{bmatrix} f_1(q) \\ f_2(q) \\ f_3(q) \end{bmatrix} = \begin{bmatrix} l^1_{a1b1} - l^0_{a1b1} \\ l^1_{a2b2} - l^0_{a2b2} \\ l^1_{rq} - l^0_{rq} \end{bmatrix} \tag{2.63}$$

and the Jacobian matrix $\boldsymbol{J}$ is denoted as

$$\boldsymbol{J}(q) = \begin{bmatrix} \frac{\partial f_1}{\partial \alpha_k} & \frac{\partial f_1}{\partial \beta_k} & \frac{\partial f_1}{\partial \gamma_k} \\ \frac{\partial f_2}{\partial \alpha_k} & \frac{\partial f_2}{\partial \beta_k} & \frac{\partial f_2}{\partial \gamma_k} \\ \frac{\partial f_3}{\partial \alpha_k} & \frac{\partial f_3}{\partial \beta_k} & \frac{\partial f_3}{\partial \gamma_k} \end{bmatrix}. \tag{2.64}$$

Starting with the initial value of

$$\boldsymbol{q}^0 = \begin{bmatrix} 0 \\ 0 \\ 0 \end{bmatrix} \tag{2.65}$$

to determine a better solutions by evaluating the Equation 2.11. The next step is to determine the increment δ^i_{in} and the iteration will be done as long as δ^i_{in} is bigger than the tolerance ϵ. The required condition of Equation 2.15 is fulfilled if the solution vector is accurate enough. The entries of the solution vector $\boldsymbol{q}$ are the *Cardan angles* and the unit of them is radiant. The choice of the tolerance is

$$\epsilon = 0.00001 \text{ rad} \tag{2.66}$$

The assumption of this tolerance is accurate enough because a rotation of 0.00001 rad of a 500 mm lever arm (that is the approximated length of the wheel carrier), change the position about

$$\Delta L_\epsilon \leqslant 500 \text{ mm} \mid \begin{bmatrix} 0 & 0 & 1 \end{bmatrix}^T - \boldsymbol{A}_{\text{cardan}}(\epsilon) \begin{bmatrix} 0 & 0 & 1 \end{bmatrix}^T \mid = 0.0071 \text{ mm} \tag{2.67}$$

if the *Cardan angles* α_k, β_k and γ_k are the tolerance ϵ. The compliance of the suspension and possible measurement deviations of the connection points might generate larger deviations.

The position of the upper control arm plus the values of the *Cardan angles* of the wheel carrier define the entire state of the suspension. The position of the wheel carrier center is given by

$$\boldsymbol{r}^1_{w,F} = \boldsymbol{r}^1_{f,F} + \boldsymbol{A}_{F1}\ \boldsymbol{r}_{fw,1} \tag{2.68}$$

with

$$\boldsymbol{r}_{fw,1} = \boldsymbol{r}_{w,1} - \boldsymbol{r}_{f,1}. \tag{2.69}$$

Length of anti-roll-bar:

The next step is to compute the length change of the spring damper element and of the anti-roll-bar due to the generalized coordinates φ and u.
A simplification to compute the length change of the anti-roll-bar is to determine only the change in z-direction in the vehicle fixed coordinate system. The anti-roll-bar is connected via the torque roll restrictor to the wheel carrier and the relevant change is in vertical directions and is defined by

$$\Delta l_{\text{arb}} = r^0_{v,F}(3) - r^1_{v,F}(3) \tag{2.70}$$

with

$$\boldsymbol{r}^1_{v,F} = \boldsymbol{r}^1_{f,F} + \boldsymbol{A}_{F1}\ \boldsymbol{r}_{fv,1}, \tag{2.71}$$

and

$$\boldsymbol{r}_{fv,1} = \boldsymbol{r}_{v,1} - \boldsymbol{r}_{f,1}. \tag{2.72}$$

Length of spring and damper:

The length change of the spring damper element is

$$\Delta l_{\text{spring}} = l^1_{\text{spring}} - l^0_{\text{spring}} \tag{2.73}$$

with

$$l^0_{\text{spring}} = |\boldsymbol{r}^0_{s1,F} - \boldsymbol{r}^0_{t1,F}| \tag{2.74}$$

and

$$l^1_{\text{spring}} = |\boldsymbol{r}^0_{s1,F} - \boldsymbol{r}^1_{t1,F}|. \tag{2.75}$$

The spring damper element is attached to link 1(wishbone) $\boldsymbol{r}^1_{t1,F}$, depicted in Figure 2.4. Link 1 will not rotate about its rod axis because this movement is blocked by the spring damper element. Furthermore $\boldsymbol{r}^1_{t1,F}$ is located on the rod axis of link 1. The approach to define this point after the movement is given by

$$\boldsymbol{r}^1_{t1,F} = \boldsymbol{r}^0_{a1,F} + \boldsymbol{e}^1_{a1b1,F}\ l_{a1t,F} \tag{2.76}$$

with

$$\boldsymbol{e}^1_{a1b1,F} = \frac{\boldsymbol{r}^1_{b1,F} - \boldsymbol{r}^0_{a1,F}}{|\boldsymbol{r}^1_{b1,F} - \boldsymbol{r}^0_{a1,F}|} \tag{2.77}$$

and

$$l_{a1t1,F} = |\boldsymbol{r}^0_{t1,F} - \boldsymbol{r}^0_{a1,F}|. \tag{2.78}$$

Computation of velocity

The aim is to determine the velocity $\boldsymbol{v}_{w,F}$ and angular velocity $\boldsymbol{\omega}_{w,F}$ of the wheel center as well as the velocity of the spring damper element and the anti-roll-bar due to the generalized velocities $\dot{\varphi}$ and $\dot{u}$. The used method for the velocity computation is based on [15]. A different approach is presented by *Georg Rill* in [21] and in [20].

Angular velocity of wheel center:

The velocity of the connection point of the upper control arm is only dependent on the angular velocity $\dot{\varphi}$ and can be determined by the cross product with $\boldsymbol{r}^1_{ef,F}$. The scalar value $\dot{\varphi}$ times the unit vector $\boldsymbol{e}_{de,F}$ of the rotation axle of the upper control arm axle gives the required rotation vector, depicted in Equation 2.79.

$$\boldsymbol{v}_{f,F} = \dot{\varphi}\ \boldsymbol{e}_{de,F} \times \boldsymbol{r}^1_{ef,F} \tag{2.79}$$

The velocity of the connection point $\boldsymbol{r}^1_{q,F}$ of the tie rod is

$$\boldsymbol{v}_{q,F}(\dot{\varphi}, \dot{u}) = \boldsymbol{v}_{f,F}(\dot{\varphi}) + \boldsymbol{\omega}_{w,F}(\dot{\varphi}, \dot{u}) \times \boldsymbol{r}^1_{fq,F} \tag{2.80}$$

and the velocity of the connection points of the lower links $\boldsymbol{r}^1_{b1,F}$ and $\boldsymbol{r}^1_{b2,F}$ is

$$\boldsymbol{v}_{b1,F}(\dot{\varphi}, \dot{u}) = \boldsymbol{v}_{f,F}(\dot{\varphi}) + \boldsymbol{\omega}_{w,F}(\dot{\varphi}, \dot{u}) \times \boldsymbol{r}^1_{fb1,F} \tag{2.81}$$

and

$$\boldsymbol{v}_{b2,F}(\dot{\varphi}, \dot{u}) = \boldsymbol{v}_{f,F}(\dot{\varphi}) + \boldsymbol{\omega}_{w,F}(\dot{\varphi}, \dot{u}) \times \boldsymbol{r}^1_{fb2,F}. \tag{2.82}$$

The four unknown three-dimensional velocity vectors are $\boldsymbol{\omega}_{w,F}$, $\boldsymbol{v}_{q,F}$, $\boldsymbol{v}_{b1,F}$ and $\boldsymbol{v}_{b2,F}$. Hence, twelve equations are required to determine them. The Equations 2.80 to 2.82 provide nine because each one exists out of three separate equations. Three more can be found by using kinematic constraints conditions. It is known that the velocity of the connection points $\boldsymbol{r}^1_{b1,F}$ and $\boldsymbol{r}^1_{b2,F}$ are perpendicular to their links because they can just perform a rotation about the spherical joints at $\boldsymbol{r}^1_{a1,F}$ and $\boldsymbol{r}^1_{a2,F}$. This relation can be expressed by the dot-product, which has to be zero and is denoted by

$$\boldsymbol{v}_{b1,F}(\dot{\varphi}, \dot{u}) \cdot \boldsymbol{r}^1_{a1b1} = 0 \tag{2.83}$$

and

$$\boldsymbol{v}_{b2,F}(\dot{\varphi}, \dot{u}) \cdot \boldsymbol{r}^1_{a2b2} = 0. \tag{2.84}$$

The connection point r of the tie rod at the rack has the known velocity $\boldsymbol{v}_{r,F}(\dot{u})$. Hence, the velocity of point q of the tie rod at the wheel carrier is given by a superposition of two velocities. The first one is the velocity due to the rotation of the tie rod about point r and the second one is the linear velocity $\boldsymbol{v}_{r,F}(\dot{u})$ of point r. The dot product of the velocity $\boldsymbol{v}_{r,F}$ and $\boldsymbol{r}^1_{rq}$ is not zero like at Equations 2.83 and 2.84 but has a remaining term

$$\boldsymbol{v}_{q,F}(\dot{\varphi}, \dot{u}) \cdot \boldsymbol{r}^1_{rq} = \boldsymbol{v}_{r,F}(\dot{u}) \cdot \boldsymbol{r}^1_{rq}. \tag{2.85}$$

The vector $\boldsymbol{v}_{r,F}(\dot{u})$ has only a velocity term in y-direction because the rack is parallel to the frontal axle, where the vehicle fixed coordinate system $\mathcal{O}_F$ is located and is

$$\boldsymbol{v}_{r,F}(\dot{u}) = \begin{bmatrix} 0 \\ \dot{u} \\ 0 \end{bmatrix}. \tag{2.86}$$

The Equations 2.80 to 2.85 can be expressed by the system of linear equations

$$\boldsymbol{B}\ \boldsymbol{x} = \boldsymbol{b} \tag{2.87}$$

with the matrix $\boldsymbol{B}$

$$\boldsymbol{B} = \begin{bmatrix} \boldsymbol{B}_{11}^{9x3} & \boldsymbol{B}_{12}^{9x9} \\ \boldsymbol{B}_{21}^{3x3} & \boldsymbol{B}_{22}^{3x9} \end{bmatrix} \tag{2.88}$$

and which contains the sub-matrix

$$\boldsymbol{B}_{11} = \begin{bmatrix} 0 & r_{fb1}(3) & -r_{fb1}(2) \\ -r_{fb1}(3) & 0 & r_{fb1}(1) \\ r_{fb1}(2) & -r_{fb1}(1) & 0 \\ 0 & r_{fb2}(3) & -r_{fb2}(2) \\ -r_{fb2}(3) & 0 & r_{fb2}(1) \\ r_{fb2}(2) & -r_{fb2}(1) & 0 \\ 0 & r_{fq}(3) & -r_{fq}(2) \\ -r_{fq}(3) & 0 & r_{fq}(1) \\ r_{fq}(2) & -r_{fq}(1) & 0 \end{bmatrix} \tag{2.89}$$

and the 9×9 negative identity matrix

$$\boldsymbol{B}_{12} = \begin{bmatrix} -1 & 0 & 0 & 0 & 0 & 0 & 0 & 0 & 0 \\ 0 & -1 & 0 & 0 & 0 & 0 & 0 & 0 & 0 \\ 0 & 0 & -1 & 0 & 0 & 0 & 0 & 0 & 0 \\ 0 & 0 & 0 & -1 & 0 & 0 & 0 & 0 & 0 \\ 0 & 0 & 0 & 0 & -1 & 0 & 0 & 0 & 0 \\ 0 & 0 & 0 & 0 & 0 & -1 & 0 & 0 & 0 \\ 0 & 0 & 0 & 0 & 0 & 0 & -1 & 0 & 0 \\ 0 & 0 & 0 & 0 & 0 & 0 & 0 & -1 & 0 \\ 0 & 0 & 0 & 0 & 0 & 0 & 0 & 0 & -1 \end{bmatrix} \tag{2.90}$$

as well as 3×3 zero matrix

$$\boldsymbol{B}_{21} = \begin{bmatrix} 0 & 0 & 0 \\ 0 & 0 & 0 \\ 0 & 0 & 0 \end{bmatrix} \tag{2.91}$$

and

$$\boldsymbol{B}_{22} =$$

$$\begin{bmatrix} r^1_{a1b1,F}(1) & r^1_{a1b1,F}(2) & r^1_{a1b1,F}(3) & 0 & 0 & 0 & 0 & 0 & 0 \\ 0 & 0 & 0 & r^1_{a2b2,F}(1) & r^1_{a2b2,F}(2) & r^1_{a2b2,F}(3) & 0 & 0 & 0 \\ 0 & 0 & 0 & 0 & 0 & 0 & r^1_{rq,F}(1) & r^1_{rq,F}(2) & r^1_{rq,F}(3) \end{bmatrix}. \tag{2.92}$$

The unknown solution vector $\mathbf{x}$ is given by

$$\boldsymbol{x} = \begin{bmatrix} \boldsymbol{\omega}_{w,F} \\ \boldsymbol{v}_{b1,F} \\ \boldsymbol{v}_{b2,F} \\ \boldsymbol{v}_{q,F} \end{bmatrix} = \begin{bmatrix} \omega_{w,F}(1) \\ \omega_{w,F}(2) \\ \omega_{w,F}(3) \\ v_{b1,F}(1) \\ v_{b1,F}(2) \\ v_{b1,F}(3) \\ v_{b2,F}(1) \\ v_{b2,F}(2) \\ v_{b2,F}(3) \\ v_{q,F}(1) \\ v_{q,F}(2) \\ v_{q,F}(3) \end{bmatrix} \tag{2.93}$$

and the known disturbance vector $\boldsymbol{b}$ by

$$\boldsymbol{b}(\dot{\varphi}, \dot{u}) = \begin{bmatrix} -v_{f,F}(1) \\ -v_{f,F}(2) \\ -v_{f,F}(3) \\ -v_{f,F}(1) \\ -v_{f,F}(2) \\ -v_{f,F}(3) \\ -v_{f,F}(1) \\ -v_{f,F}(2) \\ -v_{f,F}(3) \\ 0 \\ 0 \\ v_{r,F}(1)\ r^1_{rq,F}(1) + v_{r,F}(2)\ r^1_{rq,F}(2) + v_{r,F}(3)\ r^1_{rq,F}(3) \end{bmatrix} = \begin{bmatrix} -\dot{\varphi}\ r_{de,F}(1) \\ -\dot{\varphi}\ r_{de,F}(2) \\ -\dot{\varphi}\ r_{de,F}(3) \\ -\dot{\varphi}\ r_{de,F}(1) \\ -\dot{\varphi}\ r_{de,F}(2) \\ -\dot{\varphi}\ r_{de,F}(3) \\ -\dot{\varphi}\ r_{de,F}(1) \\ -\dot{\varphi}\ r_{de,F}(2) \\ -\dot{\varphi}\ r_{de,F}(3) \\ 0 \\ 0 \\ \dot{u}\ r^1_{rq,F}(2) \end{bmatrix}. \tag{2.94}$$

The vector $\boldsymbol{b}(\dot{\varphi}, \dot{u})$ can be split up into $\tilde{\boldsymbol{b}}_1(\dot{\varphi})$ and $\tilde{\boldsymbol{b}}_2$, illustrated in Equations 2.95 to 2.96.

$$\boldsymbol{b}(\dot{\varphi}, \dot{u}) = \dot{\varphi}\ \tilde{\boldsymbol{b}}_1(\dot{\varphi}) + \dot{u}\ \tilde{\boldsymbol{b}}_2 \tag{2.95}$$

$$\tilde{\boldsymbol{b}}_1 = \begin{bmatrix} -r_{de,F}(1) \\ -r_{de,F}(2) \\ -r_{de,F}(3) \\ -r_{de,F}(1) \\ -r_{de,F}(2) \\ -r_{de,F}(3) \\ -r_{de,F}(1) \\ -r_{de,F}(2) \\ -r_{de,F}(3) \\ 0 \\ 0 \\ 0 \end{bmatrix} \quad \tilde{\boldsymbol{b}}_2 = \begin{bmatrix} 0 \\ 0 \\ 0 \\ 0 \\ 0 \\ 0 \\ 0 \\ 0 \\ 0 \\ 0 \\ 0 \\ r^1_{rq,F}(2) \end{bmatrix} \tag{2.96}$$

By applying the superposition principle of linear equations the solution vector $\boldsymbol{x}(\dot{\varphi}, \dot{u})$ is given by the sum

$$\boldsymbol{x}(\dot{\varphi}, \dot{u}) = \boldsymbol{B}^{-1} \left(\dot{\varphi}\ \tilde{\boldsymbol{b}}_1 + \dot{u}\ \tilde{\boldsymbol{b}}_2 \right) \tag{2.97}$$

and can be written as

$$\boldsymbol{x}(\dot{\varphi}, \dot{u}) = \boldsymbol{x}_1(\dot{\varphi}) + \boldsymbol{x}_2(\dot{u}) \tag{2.98}$$

with

$$\boldsymbol{x}_1(\dot{\varphi}) = \dot{\varphi}\ \boldsymbol{B}^{-1}\tilde{\boldsymbol{b}}_1 \tag{2.99}$$

and

$$\boldsymbol{x}_2(\dot{u}) = \dot{u}\ \boldsymbol{B}^{-1}\tilde{\boldsymbol{b}}_2. \tag{2.100}$$

Using the notation of Equation 2.93 the solution $\boldsymbol{x}(\dot{\varphi}, \dot{u})$ can be written as

$$\begin{bmatrix} \boldsymbol{\omega}_{w,F} \\ \boldsymbol{v}_{b1,F} \\ \boldsymbol{v}_{b2,F} \\ \boldsymbol{v}_{q,F} \end{bmatrix} = \dot{\varphi} \begin{bmatrix} \boldsymbol{c}_1 \\ \boldsymbol{c}_2 \\ \boldsymbol{c}_3 \\ \boldsymbol{c}_4 \end{bmatrix} + \dot{u} \begin{bmatrix} \boldsymbol{d}_1 \\ \boldsymbol{d}_2 \\ \boldsymbol{d}_3 \\ \boldsymbol{d}_4 \end{bmatrix} \tag{2.101}$$

The vectors $\boldsymbol{c}_1, \boldsymbol{c}_2, \boldsymbol{c}_3$ and $\boldsymbol{c}_4$ are the solutions of $\boldsymbol{B}^{-1}\tilde{\boldsymbol{b}}_1$ and $\boldsymbol{d}_1, \boldsymbol{d}_2, \boldsymbol{d}_3$ and $\boldsymbol{d}_4$ are the solutions of $\boldsymbol{B}^{-1}\tilde{\boldsymbol{b}}_2$. Therefore, the angular velocity $\boldsymbol{\omega}_{w,F}$ can be written as

$$\boldsymbol{\omega}_{w,F} = \dot{\varphi}\ \boldsymbol{c}_1 + \dot{u}\ \boldsymbol{d}_1. \tag{2.102}$$

A different notation of $\boldsymbol{\omega}_{w,F}$ is given by

$$\boldsymbol{\omega}_{w,F} = \frac{\mathrm{d}\boldsymbol{\psi}_{w,F}(\varphi(t), u(t))}{\mathrm{d}t} = \dot{\varphi}\ \frac{\partial \boldsymbol{\psi}_{w,F}(\varphi(t), u(t))}{\partial \varphi} + \dot{u}\ \frac{\partial \boldsymbol{\psi}_{w,F}(\varphi(t), u(t))}{\partial u}. \tag{2.103}$$

The comparison of the coefficients of Equations 2.102 and 2.103 shows that

$$\boldsymbol{c}_1 = \frac{\partial \boldsymbol{\psi}_{w,F}(\varphi(t), u(t))}{\partial \varphi} \tag{2.104}$$

and

$$\boldsymbol{d}_1 = \frac{\partial \boldsymbol{\psi}_{w,F}(\varphi(t), u(t))}{\partial u} \tag{2.105}$$

which are the sought quantities.

Velocity of wheel center:

The velocity of the wheel center $\boldsymbol{v}_{w,F}$ is given by

$$\boldsymbol{v}_{w,F} = \boldsymbol{v}_{f,F}(\dot{\varphi}) + \boldsymbol{\omega}_{wc}(\dot{\varphi}, \dot{u}) \times \boldsymbol{r}^1_{fw,F} \tag{2.106}$$

and applying Equation 2.79 and 2.103, the velocity can be written as

$$\boldsymbol{v}_{w,F} = \dot{\varphi}\ (\boldsymbol{e}_{de,F} \times \boldsymbol{r}^1_{ef,F} + \boldsymbol{c}_1 \times \boldsymbol{r}^1_{fw,F}) + \dot{u}\ (\boldsymbol{d}_1 \times \boldsymbol{r}^1_{fw,F}). \tag{2.107}$$

The velocity $\boldsymbol{v}_{w,F}$ can be denoted as

$$\boldsymbol{v}_{w,F} = \frac{\mathrm{d}\boldsymbol{r}_{w,F}(\varphi(t), u(t))}{\mathrm{d}t} = \dot{\varphi}\ \frac{\partial \boldsymbol{r}_{w,F}(\varphi(t), u(t))}{\partial \varphi} + \dot{u}\ \frac{\partial \boldsymbol{r}_{w,F}(\varphi(t), u(t))}{\partial u} \tag{2.108}$$

as well and using Equation 2.107, leads to the sought quantities

$$\frac{\partial \boldsymbol{r}_{w,F}(\varphi(t), u(t))}{\partial \varphi} = (\boldsymbol{e}_{de,F} \times \boldsymbol{r}^1_{ef,F} + \boldsymbol{c}_1 \times \boldsymbol{r}^1_{fw,F}) \tag{2.109}$$

and

$$\frac{\partial \boldsymbol{r}_{w,F}(\varphi(t), u(t))}{\partial u} = \boldsymbol{d}_1 \times \boldsymbol{r}^1_{fw,F}. \tag{2.110}$$

Velocity of anti-roll-bar:

The anti-roll-bar is attached to the wheel carrier and the velocity of the anti-roll-bar is approximated by the velocity of point v in z-direction. Therefore, the velocity is given by

$$v_{v,F}(3) = (\boldsymbol{v}_{f,F}(\dot{\varphi}) + \boldsymbol{\omega}_{w,F}(\dot{\varphi}, \dot{u}) \times \boldsymbol{r}_{fv,F})\ \ \boldsymbol{e}_z \tag{2.111}$$

with

$$\boldsymbol{e}_z = \begin{bmatrix} 0 \\ 0 \\ 1 \end{bmatrix}. \tag{2.112}$$

The velocity $v_{v,F}$ can be denoted as

$$v_{v,F}(3) = \frac{\mathrm{d}l_{\mathrm{arb},F}(\varphi(t), u(t))}{\mathrm{d}t} = \left(\frac{\mathrm{d}\boldsymbol{r}_{v,F}(\varphi(t), u(t))}{\mathrm{d}t}\right)\ \boldsymbol{e}_z \tag{2.113}$$

with

$$v_{v,F}(3) = \dot{\varphi}\ \left(\frac{\partial \boldsymbol{r}_{v,F}(\varphi(t), u(t))}{\partial \varphi}\right)\ \boldsymbol{e}_z + \dot{u}\ \left(\frac{\partial \boldsymbol{r}_{v,F}(\varphi(t), u(t))}{\partial u}\right)\ \boldsymbol{e}_z, \tag{2.114}$$

respectively

$$v_{v,F}(3) = \dot{\varphi}\ \frac{\partial l_{\mathrm{arb},F}(\varphi(t),u(t))}{\partial \varphi} + \dot{u}\ \frac{\partial l_{\mathrm{arb},F}(\varphi(t),u(t))}{\partial u} \tag{2.115}$$

and using Equation 2.79 and 2.103, give

$$\frac{\partial l_{\mathrm{arb},F}(\varphi(t),u(t))}{\partial \varphi} = \left(\boldsymbol{e}_{de,F} \times \boldsymbol{r}^1_{ef,F} + \boldsymbol{c}_1 \times \boldsymbol{r}^1_{fv,F}\right)\ \boldsymbol{e}_z \tag{2.116}$$

and

$$\frac{\partial l_{\mathrm{arb},F}(\varphi(t),u(t))}{\partial u} = \left(\boldsymbol{d}_1 \times \boldsymbol{r}^1_{fv,F}\right)\ \boldsymbol{e}_z \tag{2.117}$$

which are the sought quantities.

Velocity of spring and damper:

The spring damper element is attached to point $t1$ which is located at link 1, depicted in Figure 2.4. The computation of the velocity $\boldsymbol{v}^1_{b1,F}$ is part of the solution of Equation 2.101 and is given by

$$\boldsymbol{v}_{b1,F} = \dot{\varphi}\ \boldsymbol{c}_2 + \dot{u}\ \boldsymbol{d}_2. \tag{2.118}$$

However, the velocity of the attachment point $\boldsymbol{r}^1_{t1,F}$ is lower as the velocity of point $\boldsymbol{r}^1_{t1,F}$, but the ratio p_{spring} between these velocities is constant and given by

$$p_{\mathrm{spring}} = \frac{\boldsymbol{r}^0_{t1,F} - \boldsymbol{r}^0_{a1,F}}{\boldsymbol{r}^0_{b1,F} - \boldsymbol{r}^0_{a1,F}}. \tag{2.119}$$

The required spring velocity is only acting in the spring rod axis, which is

$$\boldsymbol{e}_{t1s1} = \frac{\boldsymbol{r}^1_{s1,F} - \boldsymbol{r}^1_{t1,F}}{|\boldsymbol{r}^1_{s1,F} - \boldsymbol{r}^1_{t1,F}|} \tag{2.120}$$

The velocity v_{spring} can be denoted as

$$v_{\mathrm{spring}} = \frac{\mathrm{d}l_{\mathrm{spring}}(\varphi(t),u(t))}{\mathrm{d}t} = \dot{\varphi}\ \frac{\partial l_{\mathrm{spring}}(\varphi(t),u(t))}{\partial \varphi} + \dot{u}\ \frac{\partial l_{\mathrm{spring}}(\varphi(t),u(t))}{\partial u} \tag{2.121}$$

Using Equations 2.118, 2.119, 2.120 and 2.123 give

$$\frac{\partial l_{\mathrm{spring}}(\varphi(t),u(t))}{\partial \varphi} = \boldsymbol{c}_2 \cdot \boldsymbol{e}_{t1s1}\ p_{\mathrm{spring}} \tag{2.122}$$

and

$$\frac{\partial l_{\mathrm{spring}}(\varphi(t),u(t))}{\partial u} = \boldsymbol{d}_2 \cdot \boldsymbol{e}_{t1s1}\ p_{\mathrm{spring}} \tag{2.123}$$

which are the sought quantities.

Force elements

The determination of the spring, damper, anti-roll-bar and bump stop forces is equal to the *double wishbone* suspension and described by the Equations 2.24 to 2.34.

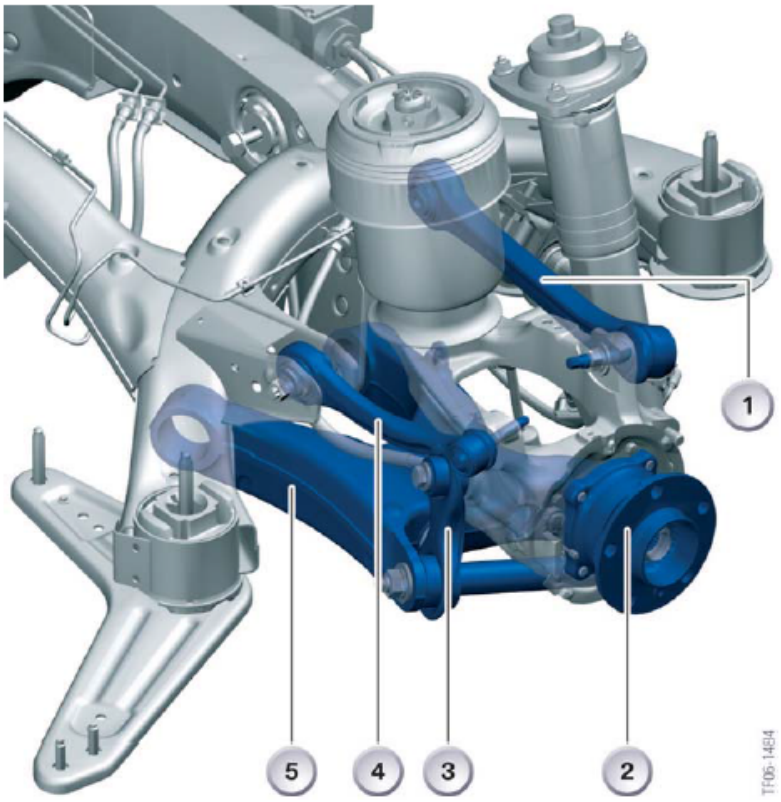

..

Figure 2.5: *Integral IV* rear suspension model of BMW X5 e70[2], 1 = Upper wishbone, 2 = Wheel carrier, 3 = Integral link, 4 = Upper trailing arm ,5= Control arm

2.4 Rear suspension

At the rear axle of the BMW X5 e70 is an *integral IV* suspension and is depicted in Figure 2.5. The approach of the rear suspension modeling is similar to the front suspension in Subsection 2.3 and the elasto-kinematics are not considered as well.
Hence, a simplified model and an advanced model will be build up. The simplified one is a *planar double wishbone* suspension because the rotation axles of the rear suspension are almost parallel. The advantage of a *planar double wishbone* suspension is that the kinematics can be described by a two-dimensional model.

The advanced model is the *integral IV* suspension where all links are considered and connected by spherical or revolute joints to guarantee a mechanically determined system.

- **Simple model:** *Planar double wishbone* suspension
- **Advanced model:** *Integral IV* suspension

In Chapter 3 the model validation is described and pros and cons are pointed out.
This Section 2.4 considers only the front left suspension. The modeling and equations

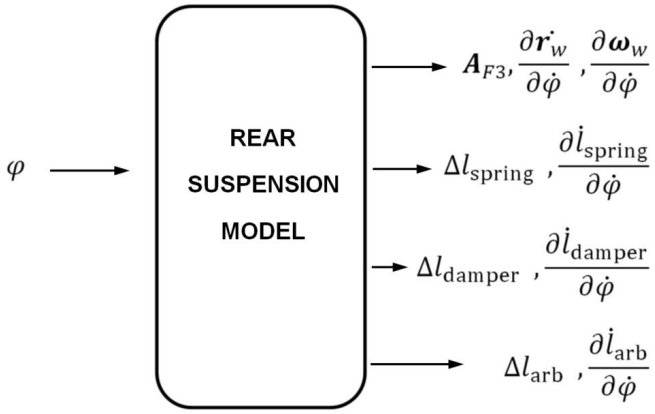

Figure 2.6: General in- and out-put of a rear suspension model

are equal for the right side, except of the geometrical connection points, because they have to be mirrored.

Model

The rear suspension model can be considered as a black box like in Subsection 2.3, depicted in Figure 2.6. The input variable is only the generalized coordinate φ. The output variables are the position of the wheel center $\boldsymbol{r}_{w,F}$, the transformation matrix $\boldsymbol{A}_{F3}$ from wheel carrier coordinate system $\mathcal{O}_3$ to the vehicle fixed coordinate system $\mathcal{O}_F$, the partial derivation of the wheel center vector by the generalized coordinate $\frac{\partial \dot{\boldsymbol{r}}_{w,1}}{\partial \dot{\varphi}}$ and the partial derivation of the rotation $\frac{\partial \boldsymbol{\omega}_{w,1}}{\partial \dot{\varphi}}$. In addition, the spring, damper and anti-roll-bar length changes are output variables as well as their partial derivations.

2.4.1 Planar double wishbone suspension

The kinematic model of the *planar double wishbone* suspension is approximated by four parallel rotation axes

$$\boldsymbol{e}_{ab} = \boldsymbol{e}_{cd} = \boldsymbol{e}_{g1g2} = \boldsymbol{e}_{f1f2} \tag{2.124}$$

and is depicted in Figure (a) 2.7.

Degrees of freedom

The determination of the DoF is done in the same way like in Subsection 2.3.1. The planar kinematic model, depicted in Figure (b) 2.7, is a planar *four-bar linkage* and has three flexible links and one fixed link. The planar model is based on the three-dimensional model in Figure (a) 2.7. One represents the trapezoid arm (link a) , one the wheel carrier (link b) and one the two upper links(link c). Each link has three DoF

and each joint reducs it by 2.
This leads to

$$DoF = 3 \cdot 3 - 2 \cdot 4 = 1 \tag{2.125}$$

and therefore, one generalized coordinate is required. The selected coordinate is the rotation angle about the trapezoid arm φ.

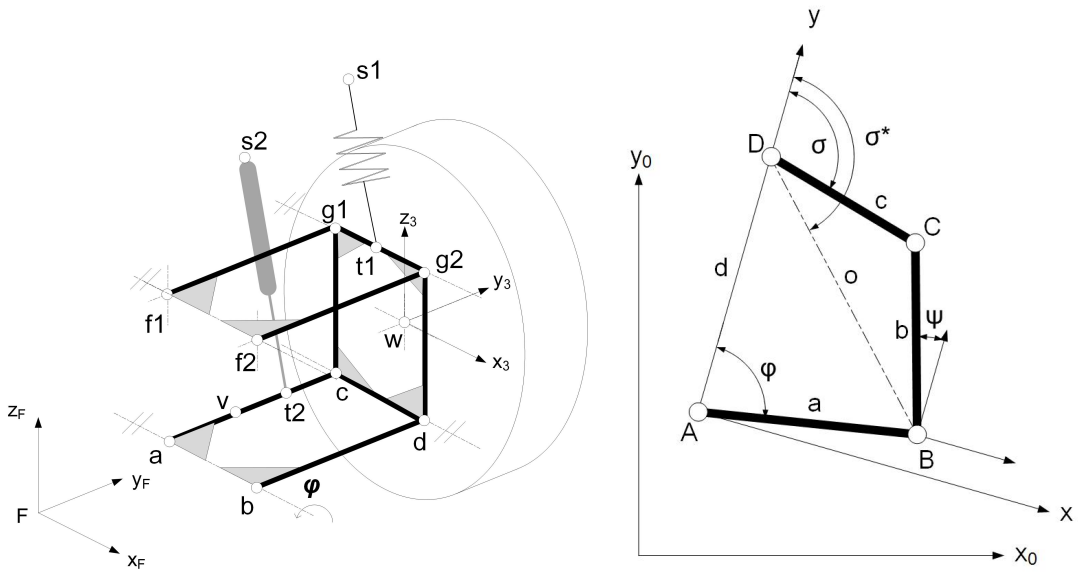

(a) 3D Model

(b) 2D Model for kinematic computation

Figure 2.7: *Planar double wishbone* suspension model of BMW X5 e70

Computation of position

Position of wheel center:

According to [11] the kinematic movement as a function of φ of a *planar double wishbone* is expressed by the equations,

$$o = \sqrt{a^2 + d^2 - 2\ a\ d\ \cos\widehat{\varphi}}, \tag{2.126}$$

$$\widehat{\sigma}^* = \pi - \arccos\left(\frac{d + a\ \cos\widehat{\varphi}}{o}\right), \tag{2.127}$$

and

$$\widehat{\sigma} = \widehat{\sigma}^* - k\ \arccos\left(\frac{o^2 + c^2 - b^2}{2\ o\ c}\right). \tag{2.128}$$

The parameter k is defined by

$$k = +1 \qquad \text{if} \qquad \widehat{\sigma}\ <\ \widehat{\sigma}^* \tag{2.129}$$

and

$$k = -1 \qquad \text{if} \qquad \widehat{\sigma} \; > \; \widehat{\sigma}^{*}. \tag{2.130}$$

k is in this case always positive, because of the proportions of the suspension and the relative small value of the maximum angle of φ. $\widehat{\psi}$ is given by

$$\widehat{\psi} = \arcsin\left(\frac{c \;\sin\left(\pi - \widehat{\varphi}\right)}{b}\right). \tag{2.131}$$

The angles $\widehat{\varphi}$, $\widehat{\sigma}$ and $\widehat{\psi}$ are the absolute angles but the required ones are the difference between the initial angles φ^0, σ^0 and ψ^0 and actual angles φ, σ and ψ. Therefore, these angles are denoted as

$$\varphi = \varphi^0 - \widehat{\varphi}, \tag{2.132}$$

$$\sigma = \sigma^0 - \widehat{\sigma}, \tag{2.133}$$

and

$$\psi = \psi^0 - \widehat{\psi}. \tag{2.134}$$

The definition of the rotation matrix $\boldsymbol{A}_{\varphi}$ about the unit axis $\boldsymbol{e}_{ab}$ in a three-dimensional space is given by Equations 2.38 to 2.40 and leads to

$$\boldsymbol{A}_{\varphi} = \boldsymbol{e}_{ab,F}\; \boldsymbol{e}_{ab,F}^{T} + (\boldsymbol{E} - \boldsymbol{e}_{ab,F}\; \boldsymbol{e}_{ab,F}^{T})\;\cos(\varphi) + \tilde{\boldsymbol{e}}_{ab,F}\;\sin(\varphi). \tag{2.135}$$

The transformation matrix $\boldsymbol{A}_{F3}$, from the wheel carrier fixed coordinate system $\mathcal{O}_3$ to the vehicle fixed coordinate system $\mathcal{O}_F$, can be written as

$$\boldsymbol{A}_{F3} = \boldsymbol{A}_{\psi} \tag{2.136}$$

and $\boldsymbol{A}_{\psi}$ is given in the form

$$\boldsymbol{A}_{\psi} = \boldsymbol{e}_{ab,F}\; \boldsymbol{e}_{ab,F}^{T} + (\boldsymbol{E} - \boldsymbol{e}_{ab,F}\; \boldsymbol{e}_{ab,F}^{T})\;\cos(\psi) + \tilde{\boldsymbol{e}}_{ab,F}\;\sin(\psi). \tag{2.137}$$

Furthermore the position of the wheel center is given by

$$\boldsymbol{r}_{w,F}^{1} = \boldsymbol{r}_{c,F}^{1} + \boldsymbol{A}_{F3}\; \boldsymbol{r}_{cw,3} \tag{2.138}$$

with

$$\boldsymbol{r}_{c,F}^{1} = \boldsymbol{r}_{a,F}^{0} + A_{\varphi}\; \boldsymbol{r}_{ac,F}^{0} \tag{2.139}$$

and

$$\boldsymbol{r}_{cw,3} = \boldsymbol{r}_{w,3} - \boldsymbol{r}_{c,3}. \tag{2.140}$$

Length of anti-roll-bar:

The determination of the length change of the anti-roll-bar Δl_{arb} is given in Subsection 2.3.2 and in particular at Equation 2.70. The position vector of the attachment point $\boldsymbol{r}_{v,F}^{1}$ at the lower control arm is denoted as

$$\boldsymbol{r}_{v,F}^{1} = \boldsymbol{r}_{a,F}^{0} + \boldsymbol{A}_{\varphi}\; \boldsymbol{r}_{av,F}^{0}. \tag{2.141}$$

Length of spring:

The Equations 2.73,2.75 and 2.72 to determine the length change of the spring element are given in Subsection 2.3.2. The position vector of the attachment point $\boldsymbol{r}^1_{t1,F}$ at the wheel carrier is expressed by

$$\boldsymbol{r}^1_{t1,F} = \boldsymbol{r}^1_{c,F} + \boldsymbol{A}_{F3}\ \boldsymbol{r}_{ct1,3}. \tag{2.142}$$

Length of damper:

The Equations 2.73,2.75 and 2.72 to determine the length change of the damper element are given in Subsection 2.3.2. The position vector of the attachment point $\boldsymbol{r}^1_{t2,F}$ at the lower control arm is denoted as

$$\boldsymbol{r}^1_{t2,F} = \boldsymbol{r}^0_{a,F} + \boldsymbol{A}_{\varphi}\ \boldsymbol{r}^0_{at2,F} \tag{2.143}$$

with

$$\boldsymbol{r}^0_{at2,F} = \boldsymbol{r}^0_{t2,F} - \boldsymbol{r}^0_{a,F}. \tag{2.144}$$

Computation of velocity

The aim is to determine the velocity $\boldsymbol{v}_{w,F}$ and angular velocity $\boldsymbol{\omega}_{w,F}$ of the wheel center as well as the velocity of the spring, damper and the anti-roll-bar due to the generalized velocity $\dot{\varphi}$.

Angular velocity of wheel center:

The angular velocity can be found by using two different formulations of the velocity of point B in the plane coordinate system, Figure 2.8. The connection point C is attached to the link a and b. The first equation describes a rotation of link a about the fixed point A and is given by

$$v_B = \dot{\varphi}\ a \tag{2.145}$$

and the second one is the rotation of link b about the instantaneous center M of Figure 2.8 and given by

$$v_B = \dot{\psi}\ \ (R1 - a)\,. \tag{2.146}$$

The instantaneous center M of link b is a unique point which is its center of rotation and has zero velocity. The normal vector of each velocity vector at any point on link b are intersecting in the instantaneous points. An exception is, if link b does not perform a rotation movement, because the velocity vectors are parallel. This would be the case if link a and c as well as b and d are of equal lengths.
The instantaneous center M is defined by

$$0 = R1\ \sin\varphi - R2\ \sin\sigma \tag{2.147}$$

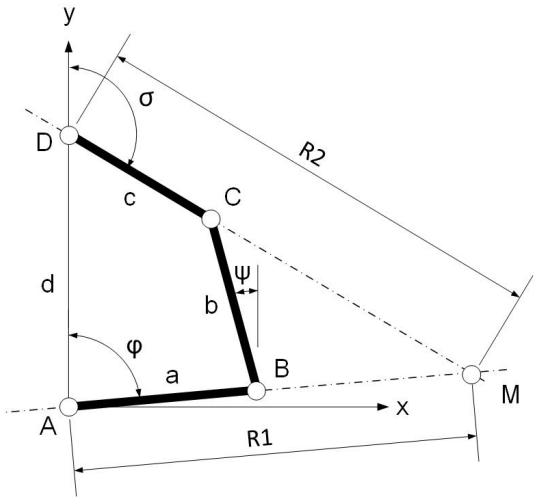

Figure 2.8: Kinematic *planar double wishbone* model with instantaneous center M

and

$$d = R1\ \cos\varphi - R2\ \cos\sigma. \tag{2.148}$$

Equations 2.147 and 2.148 can be transformed to

$$R1 = \frac{d}{\cos\varphi - \frac{\sin\varphi}{\sin\sigma}\ cos\sigma}. \tag{2.149}$$

Using the Equations 2.145 and 2.146, the angular velocity can be denoted as

$$\dot{\psi} = \dot{\varphi}\ \frac{a}{R1 - a}. \tag{2.150}$$

The rotation of φ and ψ is about the unit vector $\boldsymbol{e}_{ab}$. Hence, the angular velocity vectors can be written as

$$\dot{\boldsymbol{\varphi}} = \dot{\varphi}\ \boldsymbol{e}_{ab} \tag{2.151}$$

and

$$\dot{\boldsymbol{\psi}} = \dot{\psi}\ \boldsymbol{e}_{ab}. \tag{2.152}$$

Furthermore the angular velocity of the wheel center is given by

$$\boldsymbol{\omega}_w = \dot{\boldsymbol{\psi}} = \frac{\mathrm{d}\boldsymbol{\psi}(\varphi(t))}{\mathrm{d}t} = \frac{\partial\boldsymbol{\psi}}{\partial\varphi}\ \dot{\varphi}. \tag{2.153}$$

Comparing with Equation 2.150 results in

$$\frac{\partial\boldsymbol{\psi}}{\partial\varphi} = \frac{a}{R1 - a}\ \boldsymbol{e}_{ab} \tag{2.154}$$

which is the sought quantity.

Velocity of wheel center:

The velocity of the wheel center is given by

$$\boldsymbol{v}_{w,F} = \dot{\boldsymbol{\varphi}} \times \boldsymbol{r}^1_{ac,F} + \boldsymbol{\omega}_w \times \boldsymbol{r}^1_{cw,F} \tag{2.155}$$

and using the notation

$$\boldsymbol{v}_w = \frac{\mathrm{d}\boldsymbol{r}^1_{w,F}(\varphi(t))}{\mathrm{d}t} = \frac{\partial \boldsymbol{r}^1_{w,F}}{\partial \varphi}\ \dot{\varphi} \tag{2.156}$$

and substituting Equations 2.153, 3.38 in Equation 2.166 gives

$$\frac{\partial \boldsymbol{r}^1_{w,F}}{\partial \varphi} = \boldsymbol{e}_{ab} \times \boldsymbol{r}^1_{ac,F} + \frac{l_a}{R1 - l_a}\ \boldsymbol{e_{ab}} \times \boldsymbol{r}^1_{cw,F}. \tag{2.157}$$

which is the sought quantity.

Velocity of anti-roll-bar:

The complete determination of the velocity of the anti-roll-bar is provided in Equations 2.111 to 2.117. The anti-roll-bar is attached to the lower arm and the velocity is given by

$$\boldsymbol{v}_v = \dot{\boldsymbol{\varphi}} \times \boldsymbol{r}^1_{\boldsymbol{av,F}} \tag{2.158}$$

the z-component is the only required one, gives

$$v_{\mathrm{arb}} = \dot{\varphi}\ \frac{\partial l_{\mathrm{arb}}}{\partial \varphi} \tag{2.159}$$

with

$$\frac{\partial l_{\mathrm{arb}}}{\partial \varphi} = \left(\boldsymbol{e}_{ab} \times \boldsymbol{r}^1_{av,F}\right) \cdot \boldsymbol{e}_z \tag{2.160}$$

which is the sought quantity.

Velocity of damper:

The complete determination of the velocity of the damper is provided in Equations 2.118 to 2.123. The damper is attached to the lower arm and the velocity is given by

$$\boldsymbol{v}_q = \dot{\boldsymbol{\varphi}} \times \boldsymbol{r}^1_{at2,F} \tag{2.161}$$

only the velocity in the damper rod axis is required and is denoted as

$$v_{\mathrm{damper}} = \dot{\varphi}\ \frac{\partial l_{\mathrm{damper}}}{\partial \varphi} \tag{2.162}$$

with

$$\frac{\partial l_{\mathrm{damper}}}{\partial \varphi} = \left(\boldsymbol{e}_{ab} \times \boldsymbol{r}^1_{at2,F}\right) \cdot \boldsymbol{e}_{t2s2} \tag{2.163}$$

which is the sought quantity.

Velocity of spring:

The complete determination of the velocity of the spring is provided in Equations 2.118 to 2.123. The spring is attached to the wheel carrier and the velocity is given by

$$\boldsymbol{v}_{t1} = \dot{\boldsymbol{\varphi}} \times \boldsymbol{r}^1_{ac,F} + \boldsymbol{\omega}_c \times \boldsymbol{r}^1_{ct1,F} \tag{2.164}$$

only the velocity in the spring rod axis is required and is denoted as

$$v_{\text{spring}} = \dot{\varphi} \, \frac{\partial l_{\text{spring}}}{\partial \varphi} \tag{2.165}$$

with

$$\frac{\partial l_{\text{spring}}}{\partial \varphi} = \left(\boldsymbol{e}_{ab} \times \boldsymbol{r}^1_{ac,F} + \frac{l_a}{R1 - l_a} \, \boldsymbol{e_{ab}} \times \boldsymbol{r}^1_{ct1,F} \right) \cdot \boldsymbol{e}_{t1s1} \tag{2.166}$$

which is the sought quantity.

Force elements

The determination of the spring, damper, anti-roll-bar and bump stop forces is equal to the *double wishbone* suspension and described by the Equations 2.24 to 2.34.

2.4.2 Integral IV suspension

The *integral IV* suspension model represents the real rear suspension of the BMW X5. Therefore, all links are considered and connected by spherical or revolute joints to guarantee a mechanical determined system.

Degrees of freedom

The determination of the DoF is done in the same way like in Subsection 2.3.1. This suspension is made of five elements which affect the kinematic movement. This elements are the control arm, wishbone, trailing arm, integral link and wheel carrier. Each one has six DoF and a couple of constraints. It has seven spherical joints, one revolute joint at the control arm. The wishbone, trailing arm and integral link can rotate about their rod axis.

This leads to

$$DoF = 6 \cdot 5 - 3 \cdot 7 - 5 \cdot 1 - 5 \cdot 0 - 3 = 1 \tag{2.167}$$

and therefore, one generalized coordinate is required. This one is the rotation angle about the control arm φ.

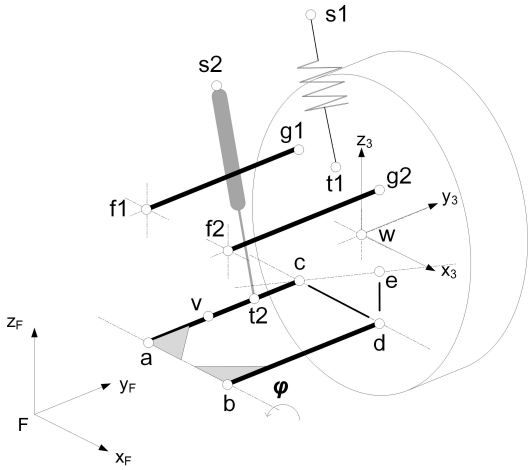

Figure 2.9: *Integral IV* suspension model of BMW X5 e70

Computation of position

Position of wheel center:

The computation of the position of the wheel center and the transformation matrix is done in the same way like in Subsection 2.3.2. However, the rear suspension has only one degree of freedom and the related generalized coordinate φ is the rotation angle of the lower control arm. The position of the wheel center as well as the transformation matrix can be found by solving a set of nonlinear equations. The position of the lower control arm is given by

$$\boldsymbol{r}^1_{c,F} = \boldsymbol{r}^0_{a,F} + \boldsymbol{A}_\varphi \, \boldsymbol{r}^0_{ac,F} \tag{2.168}$$

and

$$\boldsymbol{r}^1_{d,F} = \boldsymbol{r}^0_{a,F} + \boldsymbol{A}_\varphi \, \boldsymbol{r}^0_{ad,F}. \tag{2.169}$$

The rotation matrix $\boldsymbol{A}_\varphi$ describes a rotation about the axle $\boldsymbol{e}_{ab,F}$ which is given by

$$\boldsymbol{e}_{ab,F} = \frac{\boldsymbol{r}^0_{b,F} - \boldsymbol{r}^0_{a,F}}{|\boldsymbol{r}^0_{b,F} - \boldsymbol{r}^0_{a,F}|}. \tag{2.170}$$

The unknown position vectors are $\boldsymbol{r}^1_{e,F}$,$\boldsymbol{r}^1_{g1,F}$ and $\boldsymbol{r}^1_{g2,F}$. The assumption is that the distances between those vectors stay constant after a movement. This can be done by the Cartesian coordinates and for three vectors are nine equations necessary and defined as follows

$$|\boldsymbol{r}^0_{d,F} - \boldsymbol{r}^0_{e,F}| = |\boldsymbol{r}^1_{d,F} - \boldsymbol{r}^1_{e,F}|, \tag{2.171}$$

$$|\boldsymbol{r}^0_{c,F} - \boldsymbol{r}^0_{e,F}| = |\boldsymbol{r}^1_{c,F} - \boldsymbol{r}^1_{e,F}|, \tag{2.172}$$

$$|\boldsymbol{r}^0_{g1,F} - \boldsymbol{r}^0_{e,F}| = |\boldsymbol{r}^1_{g1,F} - \boldsymbol{r}^1_{e,F}|, \tag{2.173}$$

$$|\boldsymbol{r}^0_{g2,F} - \boldsymbol{r}^0_{e,F}| = |\boldsymbol{r}^1_{g2,F} - \boldsymbol{r}^1_{e,F}|, \tag{2.174}$$

$$|\boldsymbol{r}^0_{f1,F} - \boldsymbol{r}^0_{g1,F}| = |\boldsymbol{r}^1_{f1,F} - \boldsymbol{r}^1_{g1,F}|, \tag{2.175}$$

$$|\boldsymbol{r}^0_{f2,F} - \boldsymbol{r}^0_{g2,F}| = |\boldsymbol{r}^1_{f2,F} - \boldsymbol{r}^1_{g2,F}|, \tag{2.176}$$

$$|\boldsymbol{r}^0_{c,F} - \boldsymbol{r}^0_{g1,F}| = |\boldsymbol{r}^1_{c,F} - \boldsymbol{r}^1_{g1,F}|, \tag{2.177}$$

$$|\boldsymbol{r}^0_{c,F} - \boldsymbol{r}^0_{g2,F}| = |\boldsymbol{r}^1_{c,F} - \boldsymbol{r}^1_{g2,F}|, \tag{2.178}$$

and

$$|\boldsymbol{r}^0_{g1,F} - \boldsymbol{r}^0_{g2,F}| = |\boldsymbol{r}^1_{g2,F} - \boldsymbol{r}^1_{g2,F}|. \tag{2.179}$$

The solution can be found by applying the *Newton-Raphson* algorithm. The transformation matrix $\boldsymbol{A}_{F3}$ from the left wheel carrier fixed coordinate system $\mathcal{O}_3$ to vehicle fixed coordinate system $\mathcal{O}_F$ can be found by using

$$\boldsymbol{C}^1 = \boldsymbol{A}_{F3}\boldsymbol{C}^0 \tag{2.180}$$

with

$$\boldsymbol{A}_{F3} = \boldsymbol{C}^0\ (\boldsymbol{C}^1)^{-1}. \tag{2.181}$$

$\boldsymbol{C}^1$ and $\boldsymbol{C}^0$ are two 3×3 matrices of freely chosen three unit vectors, fixed at the wheel carrier and linearly independent. $\boldsymbol{C}^0$ is the state matrix before the movement and defined as

$$\boldsymbol{C}^0 = \begin{bmatrix} \boldsymbol{e}^0_a & \boldsymbol{e}^0_b & \boldsymbol{e}^0_c \end{bmatrix} \tag{2.182}$$

and $\boldsymbol{C}^1$ is the state matrix after the movement and defined as

$$\boldsymbol{C}^1 = \begin{bmatrix} \boldsymbol{e}^1_a & \boldsymbol{e}^1_b & \boldsymbol{e}^1_c. \end{bmatrix} \tag{2.183}$$

The unit vectors are

$$\boldsymbol{e}^0_a = \frac{\boldsymbol{r}^0_{g1,F} - \boldsymbol{r}^0_{w,F}}{|\boldsymbol{r}^0_{g1,F} - \boldsymbol{r}^0_{w,F}|}, \tag{2.184}$$

$$\boldsymbol{e}^0_b = \frac{\boldsymbol{r}^0_{e,F} - \boldsymbol{r}^0_{w,F}}{|\boldsymbol{r}^0_{e,F} - \boldsymbol{r}^0_{w,F}|}, \tag{2.185}$$

$$\boldsymbol{e}^0_c = \boldsymbol{e}^0_a \times \boldsymbol{e}^0_b, \tag{2.186}$$

$$\boldsymbol{e}^1_a = \frac{\boldsymbol{r}^1_{g1,F} - \boldsymbol{r}^1_{w,F}}{|\boldsymbol{r}^1_{g1,F} - \boldsymbol{r}^1_{w,F}|}, \tag{2.187}$$

$$\boldsymbol{e}^1_b = \frac{\boldsymbol{r}^1_{e,F} - \boldsymbol{r}^1_{w,F}}{|\boldsymbol{r}^1_{e,F} - \boldsymbol{r}^1_{w,F}|}, \tag{2.188}$$

and

$$\boldsymbol{e}^1_c = \boldsymbol{e}^1_a \times \boldsymbol{e}^1_b \tag{2.189}$$

The position of the wheel center is given by

$$\boldsymbol{r}_{w,F}^{1} = \boldsymbol{r}_{c,F}^{1} + \boldsymbol{A}_{F3}\ \boldsymbol{r}_{cw,3} \tag{2.190}$$

with

$$\boldsymbol{r}_{cw,3} = \boldsymbol{r}_{w,3} - \boldsymbol{r}_{c,3}. \tag{2.191}$$

Length of anti-roll-bar:

The computation of the length of the anti-roll-bar is the same of Equation 2.141.

Length of spring:

The computation of the length of the spring is the same of Equation 2.142.

Length of damper:

The computation of the length of the damper is the same of Equation 2.143 and 2.144.

Computation of velocity

The computation of the velocity $\boldsymbol{v}_{w,F}$ and angular velocity $\boldsymbol{\omega}_{w,F}$ of the wheel center, the velocity of the spring, damper and anti-roll-bar, can be done in the same way like in Subsection 2.3.2 by using the Equations 2.79 to 2.123.

Force elements

The determination of the spring, damper, anti-roll-bar and bump stop forces is equal to the *double wishbone* suspension and described by the Equations 2.24 to 2.34.

2.5 Steering system

The vehicle model for the conventional SbW vehicle provides the rack position as an input parameter and a steering model is not needed. But the TV model has the front wheel torques as input parameters and the rack position u is one more degree of freedom and requires a steering model.

Torque vectoring steering model

The steering model is based on the model of [20] and is modified for the TV steering. The required mass M_u for the differential equation is given by

$$M_u = m_1\ \boldsymbol{t}_{1u}^{T}\ \boldsymbol{t}_{1u} + \boldsymbol{d}_{1u}^{T}\ \boldsymbol{\Theta}_1\ \boldsymbol{d}_{1u} + m_2\ \boldsymbol{t}_{2u}^{T}\ \boldsymbol{t}_{2u} + \boldsymbol{d}_{2u}^{T}\ \boldsymbol{\Theta}_2\ \boldsymbol{d}_{2u} + m_{rack} + m_{red,act}. \tag{2.192}$$

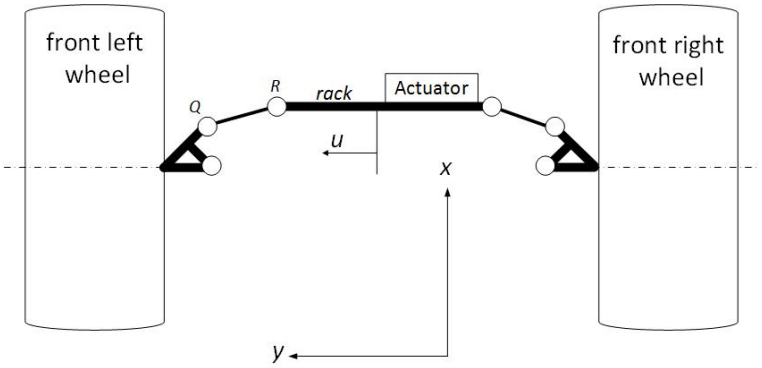

Figure 2.10: Steering system model based on [20]

The partial derivation of the wheel center position to the rack position for the front left suspension is given by

$$\boldsymbol{t}_{1u} = \frac{\partial \boldsymbol{r}_{w1,F}}{\partial u} \tag{2.193}$$

and for the front right suspension by

$$\boldsymbol{t}_{2u} = \frac{\partial \boldsymbol{r}_{w2,F}}{\partial u}. \tag{2.194}$$

Respectively the partial derivation of the wheel center rotation to the rack position for the front left suspension is given by

$$\boldsymbol{d}_{1u} = \frac{\partial \boldsymbol{\psi}_{w1,F}}{\partial u} \tag{2.195}$$

and for the front right by

$$\boldsymbol{d}_{1u} = \frac{\partial \boldsymbol{\psi}_{w2,F}}{\partial u}. \tag{2.196}$$

m_1 is the mass and $\boldsymbol{\Theta}_1$ the moment of inertia tensor of the front left suspension, including the tire. Respectively, m_2 and $\boldsymbol{\Theta}_2$ are the parameters for the front right suspension. m_{rack} is the mass of the rack and $m_{red,act}$ is the reduced mass of the actuator on the rack.
The required force Q_u for the differential equation is given by

$$Q_u = \boldsymbol{t}_{1u}^T \boldsymbol{F}_{w1}\ \boldsymbol{t}_{1u} + \boldsymbol{d}_{1u}^T \boldsymbol{T}_{w1}\ \boldsymbol{d}_{1u} + \boldsymbol{t}_{2u}^T \boldsymbol{F}_{w2}\ \boldsymbol{t}_{2u} + \boldsymbol{d}_{2u}^T \boldsymbol{T}_{w2}\ \boldsymbol{d}_{2u} + \delta_u\ \dot{u} + F_{fr}. \tag{2.197}$$

$\boldsymbol{F}_{w1}$ and $\boldsymbol{F}_{w2}$ are the effective forces at the front wheel centers. The effective torques at the wheel centers $\boldsymbol{T}_{w1}$ and $\boldsymbol{T}_{w2}$ are including the driving torques and are given by

$$\boldsymbol{T}_{wi} = \boldsymbol{T}_{pi} + \boldsymbol{T}_i \quad i = 1, 2. \tag{2.198}$$

$\boldsymbol{T}_i$ are the driving torques and $\boldsymbol{T}_{pi}$ are the resulting torque vectors at the wheel center due to the contacted forces and torques at the contacted patches. One example for a

part of this torque vector is the self-aligning torque.
The damping coefficient δ_u at the rack remains constant and the friction force F_{fr} is approximated by a constant value. In general, the friction force is a function of the applied normal force between the rack and the steering gear. But it requires a more elaborate model to determine the magnitude of the force because it varies with the inclination angles and the rod forces of the tie rods.
The equation of motion can be expressed by the second order differential equations of

$$\ddot{u} = \frac{M_u}{Q_u}. \tag{2.199}$$

3 Parametrization and validation

The Table 3.1 shows the required parameters for the full multi-body vehicle model as well as their sources.

Some of these parameters can have a major impact on vehicle dynamic simulations and it is a challenge to define and identify them accurately. There are some parameters which are easy determinable, such as the vehicle mass. Others require more effort like the moment of inertia of bodies, such as the chassis or wheel carrier.
The relevance of parameters depends on the driving maneuver as well. For example, the damper forces will be zero at a steady state maneuver. Moreover, some of the parameters can change their properties because of ageing or external influences like temperature. Furthermore, the prototype vehicle is a rebuilt test vehicle with a mileage of about 200,000 km. It is important to consider these circumstances in the identification of the parameters because they might differ from those of a new car. Some parameters are from a brand new car and are provided by an official report of BMW [2]. Others are based on measurements of students, for example, the connections points of the suspension. There is no information about the accuracy of these values.

To question varying parameters is not a part of this thesis. The aim of this chapter is to get parameters as accurate as possible without greater extra effort.

Table 3.1: Required Parameter

CHASSIS		
Name	**Value**	**Source**
Wheelbase	2.933 m	BMW manual [2]
Track width front	1.644 m	BMW manual [2]
Track width rear	1.65 m	BMW manual [2]
Chassis CoG (including drivers)	$\begin{bmatrix}-1.584 & 0 & 0.218\end{bmatrix}$ m	Section 3.1
Air drag force coefficient	0.38	*Cordes*** [4]
Air drag force position	$\begin{bmatrix}1 & 0 & 0.2\end{bmatrix}$ m	*Cordes*** [4]
Frontal area	2.9 m^2	BMW manual [2]
Chassis mass	2363.7 kg	Section 3.1
Mass of two drivers	150 kg	Section 3.1
Chassis main inertia $\begin{bmatrix}\Theta_{xx} & \Theta_{yy} & \Theta_{zz}\end{bmatrix}$	$\begin{bmatrix}1080 & 6500 & 6525\end{bmatrix}$ kgm^2	Section 3.1
Chassis inertia moment of deviation Θ_{xz}	168 kgm^2	Section 3.1
TIRES		
TMeasy parameter	–	TKP Report [7]
Tire and rim mass	30.7 kg	Section 3.2
Tire and rim main inertia $\begin{bmatrix}\Theta_{xx} & \Theta_{yy} & \Theta_{zz}\end{bmatrix}$	$\begin{bmatrix}1.4 & 2.34 & 1.4\end{bmatrix}$ kgm^2	Section 3.2
Tire and rim inertia moment of deviation $\begin{bmatrix}\Theta_{xy} & \Theta_{xz} & \Theta_{yz}\end{bmatrix}$	$\begin{bmatrix}1080 & 6500 & 6525\end{bmatrix}$ kgm^2	Section 3.2
FRONT SUSPENSION		
Connection points	–	NTB Buchs*
Front suspension mass	45.4 kg	Section 3.3
Front suspension main inertia $\begin{bmatrix}\Theta_{xx} & \Theta_{yy} & \Theta_{zz}\end{bmatrix}$	$\begin{bmatrix}0.85 & 0.69 & 0.36\end{bmatrix}$ kgm^2	Section 3.3
Front suspension inertia moment of deviation $\begin{bmatrix}\Theta_{xy} & \Theta_{xz} & \Theta_{yz}\end{bmatrix}$	$\begin{bmatrix}-0.03 & -0.02 & -0.05\end{bmatrix}$ kgm^2	Section 3.3
Spring rate	65.3 N/mm	BMW*
Damper table	–	BMW*
Anti-roll-bar rate	28.5 N/mm	BMW*
Bump stop characteristics	6.53 N/mm	Section 3.3
REAR SUSPENSION		
Connection points	–	NTB Buchs*
Rear suspension mass	39.7 kg	Section 3.4
Rear suspension main inertia $\begin{bmatrix}\Theta_{xx} & \Theta_{yy} & \Theta_{zz}\end{bmatrix}$	$\begin{bmatrix}0.85 & 0.34 & 0.75\end{bmatrix}$ kgm^2	Section 3.4
Rear suspension inertia moment of deviation $\begin{bmatrix}\Theta_{xy} & \Theta_{yz}\end{bmatrix}$	$\begin{bmatrix}0.01 & -0.01\end{bmatrix}$ kgm^2	Section 3.4
Spring rate defection	54.6 N/mm	BMW*
Spring rate rebound	43.8 N/mm	BMW*
Damper table	–	BMW*
Anti-roll-bar rate	22.7 N/mm	BMW*
Bump stop table	5.46 N/mm	Section 3.4
STEERING SYSTEM		
Steering gear friction force	270 N	TKP SbW*
Steering gear damping coefficient	780 Nm/s	TKP SbW*

* internal information, no official report provided ** no official, reliable source

Moment of Inertia

This chapter provides the necessary equations for the computation of the moment of inertia of certain bodies and is based on [11]. The general equations for the moment of inertias are given in Equations 3.1 to 3.6.

$$\Theta_{xx} = \int \left(y^2 + z^2\right)\ \mathrm{d}m = \int \left(r_x^2\right)\ \mathrm{d}m \tag{3.1}$$

$$\Theta_{yy} = \int \left(x^2 + z^2\right)\ \mathrm{d}m = \int \left(r_y^2\right)\ \mathrm{d}m \tag{3.2}$$

$$\Theta_{zz} = \int \left(x^2 + y^2\right)\ \mathrm{d}m = \int \left(r_z^2\right)\ \mathrm{d}m \tag{3.3}$$

$$\Theta_{xy} = \Theta_{yx} = \int xy\ \mathrm{d}m \tag{3.4}$$

$$\Theta_{xz} = \Theta_{zx} = \int xz\ \mathrm{d}m \tag{3.5}$$

$$\Theta_{yz} = \Theta_{zy} = \int yz\ \mathrm{d}m \tag{3.6}$$

The general moment of inertia tensor is defined as

$$\boldsymbol{\Theta} = \begin{bmatrix} \Theta_{xx} & -\Theta_{xy} & -\Theta_{xz} \\ -\Theta_{yx} & \Theta_{yy} & -\Theta_{yz} \\ -\Theta_{zx} & -\Theta_{zy} & \Theta_{zz} \end{bmatrix}. \tag{3.7}$$

The determination of the moment of inertia tensors of each sub-body of the vehicle will be done by using simplified models. These models consists of point masses, hollow cylinders, full cylinders, cubes or a combination of them. Table 3.2 depicts all entries of the moment of inertia tensor for these bodies.

Table 3.2: Moment of inertia

	Point mass parallel-axes theorem	**Hollow cylinder** x-axis = rotation axis	**Full cylinder** x-axis = rotation axis	**Cube**
Θ_{xx}	$m\ \left(y^2 + z^2\right)$	$m/2\ \left(r_{in}^2 + r_{ex}^2\right)$	$m/2\ r^2$	$m/12\ \left(l_y^2 + l_z^2\right)$
Θ_{yy}	$m\ \left(x^2 + z^2\right)$	$m/4\ \left(r_{in}^2 + r_{ex}^2 + l_x^2/3\right)$	$m/12\ \left(3\ r^2 + l_x^2\right)$	$m/12\ \left(l_x^2 + l_z^2\right)$
Θ_{zz}	$m\ \left(x^2 + y^2\right)$	$m/4\ \left(r_{in}^2 + r_{ex}^2 + l_x^2/3\right)$	$m/12\ \left(3\ r^2 + l_x^2\right)$	$m/12\ \left(l_x^2 + l_y^2\right)$
Θ_{xy}	$m\ xy$	–	–	–
Θ_{xz}	$m\ xz$	–	–	–
Θ_{yz}	$m\ yz$	–	–	–
l_x, l_y, l_z = length in x,y,z-direction, r = radius, r_{in} = internal radius, r_{ex} = external radius				

3.1 Chassis

This sections is about the determination of the unknown chassis parameters.

Center of gravity and mass

This subsection provides the determination of the center of gravity (CoG) of the chassis. The used coordinate system is the vehicle fixed system $\mathcal{O}_F$. One assumption is that the vehicle is symmetric about the xz-plane. Therefore, the y-value of the inertia tensor is zero, related to Equations 3.1 to 3.7. The approach to find the x-position of the CoG is to put all four wheels on wheel load scales and to measure the front m^0_{front} and rear m^0_{rear} wheel loads at a flat, horizontal ground. However, the required weight is the chassis weight without the suspension and wheel masses. This leads to Equation 3.8. The wheel mass includes the tire and rim mass.

$$L_{0F} = \frac{m^0_{\text{rear}} - 2\,(m_{\text{rearsusp}} + m_{\text{wheel}})}{m^0_{\text{rear}} + m^0_{\text{front}} - 2\,(m_{\text{rearsusp}} + m_{\text{frontsusp}}) - 4\;m_{\text{wheel}}}\;L_{WB} \tag{3.8}$$

L_{WB} is the wheelbase and L_{0F} is the negative position of the CoG $-\boldsymbol{r}_{\text{CoG empty},F}(3)$ in the vehicle fixed coordinate system of the empty vehicle.
The z-position of the CoG can be determined by doing the same measurement but lifting up the front axle of the vehicle. Next, the inclination angle α_l, depicted in Figure 3.1, the new wheel loads $m_{front,1}$ and $m_{rear,1}$ have to be measured. These measurements were done in a workshop at TKP by using a table lift. The height h of the CoG is given by

$$h = \frac{L_{0R}\cos\alpha - L_{1R}}{\sin\alpha} \tag{3.9}$$

with

$$L_{1R} = L_{WB}\;\cos\alpha - L_{1F}, \tag{3.10}$$

$$L_{0R} = L_{WB} - L_{0F} \tag{3.11}$$

and

$$L_{1F} = \frac{m^1_{\text{rear}} - 2\,(m_{\text{rearsusp}} + m_{\text{wheel}})}{m^1_{\text{rear}} + m^1_{\text{front}} - 2\,(m_{\text{rearsusp}} + m_{\text{frontsusp}}) - 4\;m_{\text{wheel}}}\;L_{WB}. \tag{3.12}$$

The angle α_l is given by

$$\alpha_l = \arcsin\left(\frac{h_l}{L_M}\right). \tag{3.13}$$

h_l is the height difference between the two reference points at the chassis in the lifted state and L_M is the absolute distance of these points.

A way to increase the accuracy is to do the same measurements in the opposite direction and lift the rear axle up. Unfortunately, it was not possible to get accurate, reliable data out of the rear axle lifted measurements. The results of the front axle lifted measurements

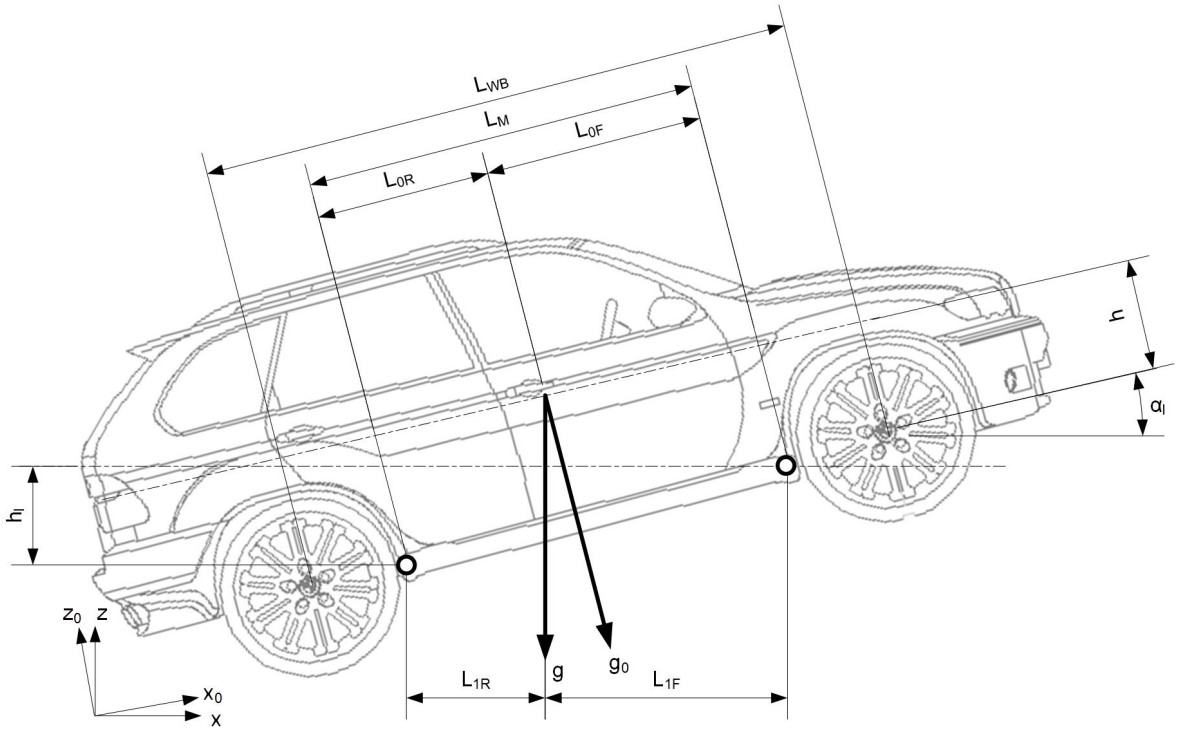

..

Figure 3.1: Scatch for center of gravity computation

are listed in Table 3.3. The measurements were done without drivers on board. During test drives there is always one driver and one co-driver on board. The mass and position of them is given by

$$m_{2dirvers} = 150 \text{ kg}, \tag{3.14}$$

$$\boldsymbol{r}_{2\text{dirvers},F} = \begin{bmatrix} -1.2 \\ 0 \\ 0.35 \end{bmatrix} \text{m} \tag{3.15}$$

and the CoG position in x-direction is given by

$$L_{0Fd} = \frac{m^0_{\text{total}}\ L_{0F} + m_{2drivers}\ \ (-r_{2drivers}(1))}{m^0_{total,0} + m_{2drivers}} \tag{3.16}$$

and in z-direction

$$h_d = \frac{m^0_{total,0}\ h + m_{2drivers}\ r_{2drivers}(3)}{m^0_{total,0} + m_{2drivers}}. \tag{3.17}$$

Table 3.3: Measured chassis weight for center of gravity determination

Center of Gravity measurement data of the empty vehicle					
Commend	**Index**	m^i_{front}	m^i_{rear}	m^i_{total}	h_l
Vehicle on horizontal ground	0	1067.6 kg	1296.1kg	2363.7 kg	0 m
Front wheels lifted	1	992.6 kg	1371.1 kg	2363.7 kg	0.535 m

The stated weights are without the suspension, tire and rim masses

L_M is the distance between the measurement point on the chassis, depicted in Figure 3.1, and is given by

$$L_M = 2.02 \text{ m}. \tag{3.18}$$

The CoG position in the vehicle fixed coordinate system $\mathcal{O}_F$ without drivers is given by

$$\boldsymbol{r}_{\text{CoG empty},F} = \begin{bmatrix} -L_{1F} \\ 0 \\ h \end{bmatrix} = \begin{bmatrix} -1.608 \\ 0 \\ 0.218 \end{bmatrix} \text{m} \tag{3.19}$$

and with drivers by

$$\boldsymbol{r}_{\text{cog driver},F} = \begin{bmatrix} -L_{1Fd} \\ 0 \\ h_d \end{bmatrix} = \begin{bmatrix} -1.584 \\ 0 \\ 0.226 \end{bmatrix} \text{m}. \tag{3.20}$$

The chassis mass without drivers is given by

$$m_{\text{ch,empty}} = 2369.7 \text{ kg} \tag{3.21}$$

and with drivers by

$$m_{\text{ch,driver}} = 2513.7 \text{ kg}. \tag{3.22}$$

Moment of inertia tensor

The master theses from *Leichtfried Franz* [14] and *Johannes Fehr* [8] show how to identify the moment of inertia of a vehicle about the x-, y- and z-axle($\Theta_{xx}, \Theta_{yy}, \Theta_{zz}$). They estimated these parameters by evaluating certain test drives. These theses point out that the determined parameters are an approximation and that accurate results can be found at expensive test benches.
The full three-dimensional vehicle model requires the complete inertia tensor including the moment of deviation. The strategy at the present thesis is to build up a simplified model, consisting of bodies and mass points, with the same CoG of the real chassis. The dimensions, positions and masses of the engine and accumulator battery stacks are already known. The moment of inertia about the z- and x-axle will be determined by evaluating the available measurement data and the use of the vehicle simulation. The missing entries of the tensor will be found by the simplified model, depicted in Figure

3.2. The advantage of this approach is the double check of the results. In other words, a physical model can be used to validate the results from the measurements.

Moment of inertia from test drives

The test maneuver for the parameter identification should guarantee a high dynamic about the z- and x-axle. The selected test maneuver for Θ_{zz} is a double lane change at 40 kph and at 50 kph for a left and right turn. The yaw acceleration is a good indicator for the moment of inertia about the z-axle and the roll acceleration for the x-axle. The normalized error vector of the yaw acceleration $\ddot{\gamma}$ between the simulated and the measured data, of the length n, is given by the *normalized mean square error* (*NRMSE*) and is defined as

$$NRMSE_{yaw} = \sqrt{\frac{\sum_{t=1}^{n} \left(\ddot{\gamma}_{sim} - \ddot{\gamma}_{meas}\right)^2}{n}} \frac{1}{\ddot{\gamma}_{max,meas} - \ddot{\gamma}_{min,meas}}. \tag{3.23}$$

The determination of a significant Θ_{xx} was more complicated than Θ_{zz}. A simplified definition of the *NRMSE* is given by the sum of the peak differences of the measured and simulated signals. The *NRMSE* of the roll accelerations $\ddot{\alpha}$ is given by

$$NRMSE_{roll} = \sqrt{\frac{\left(\ddot{\alpha}_{max,sim} - \ddot{\alpha}_{max,meas}\right)^2 + \left(\ddot{\alpha}_{min,sim} - \ddot{\alpha}_{min,meas}\right)^2}{2\ \left(\ddot{\alpha}_{max,meas} - \ddot{\alpha}_{min,meas}\right)^2}}. \tag{3.24}$$

The results are listed in Table 3.4 and Table 3.5. The simulation interval for the Θ_{zz} determination is from $1,000$ kgm^2 to $10,000$ kgm^2 in 100 kgm^2 steps and for the Θ_{xx} determination from 100 kgm^2 to $3,000$ kgm^2 in 100 kgm^2 steps. The reason for the chosen step size of 100 kgm^2 is because the variance of errors is still higher.

Table 3.4: Moment of inertia identification from test drives

Moment of inertia identification about the z-axis		
Test maneuver	Θ_{zz}	$NRMSE_{yaw}$
Double lane change 40 kph run 1	$6,500$ kgm^2	0.0216
Double lane change 40 kph run 2	$6,400$ kgm^2	0.0173
Double lane change 50 kph run 1	$6,600$ kgm^2	0.0266
Double lane change 50 kph run 2	$6,600$ kgm^2	0.0186
Average:	$6,525$ kgm^2	

Table 3.5: Moment of inertia identification from test drives

Moment of inertia identification about the x-axis		
Test maneuver	Θ_{xx}	$NRMSE_{roll}$
Step steer left 30 kph	$1,100$ kgm^2	0.0137
Step steer right 30 kph	$1,000$ kgm^2	0.0158
Step steer left 50 kph	$1,000$ kgm^2	0.0329
Step steer right 50 kph	$1,200$ kgm^2	0.057
Step steer left 70 kph	$1,100$ kgm^2	0.0888
Step steer right 70 kph	$1,100$ kgm^2	0.0031
Average:	$1,080$ kgm^2	

Simplified model for moment of inertia determination

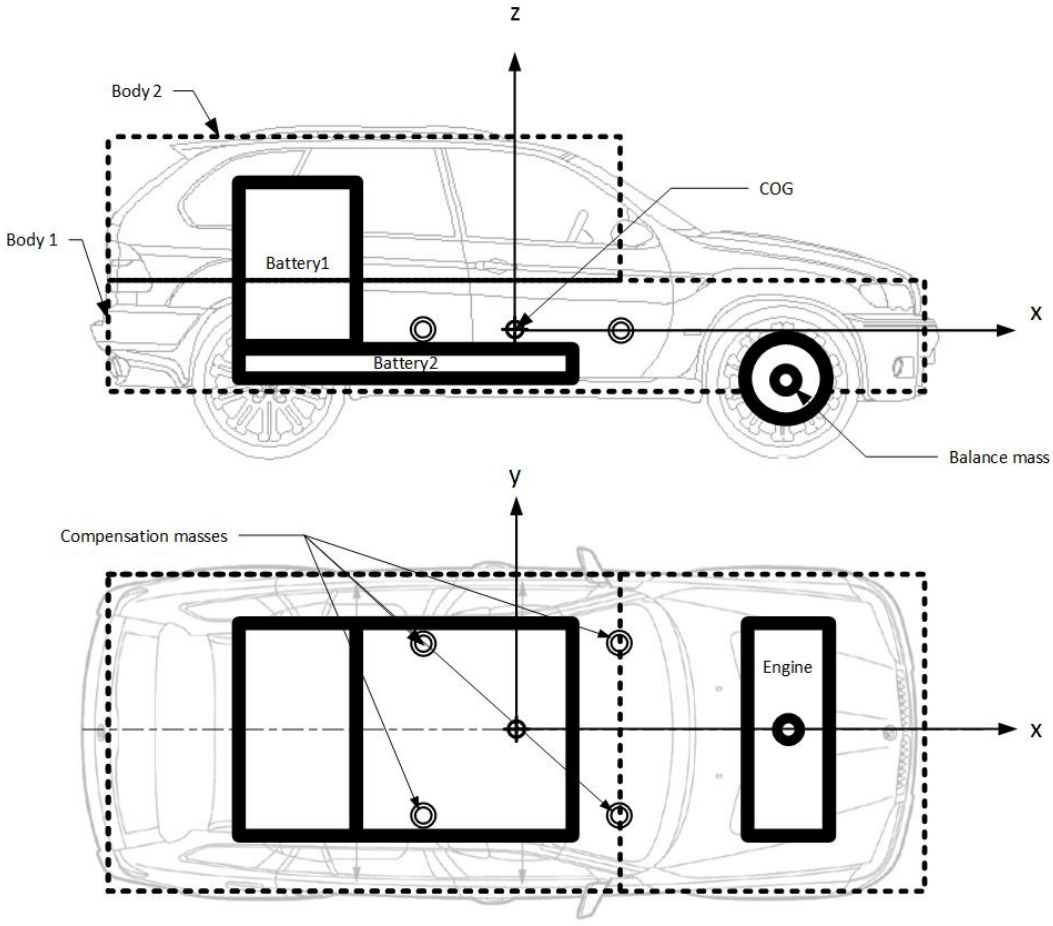

..

Figure 3.2: Simplified model for moment of inertia tensor computation

The CoG of *Body1* and of the *Compensation masses* are in the CoG of the vehicle and is depicted in Figure 3.2. The *Balance mass* is located at the center of the front axle but the z-position is the same of the CoG. The mass of *Body1* is estimated. Hence, only the *Balance mass*, *Body2* and the *Compensation masses* are unknown.
The position of the CoG in z-direction is fixed. Therefore, the mass of *Body2* can be calculated with

$$m_{\mathrm{B2}} = \frac{-m_{\mathrm{Ba1}}\ r_{\mathrm{Ba1}}(3) - m_{\mathrm{Ba2}}\ r_{\mathrm{Ba2}}(3) + m_{\mathrm{E}}\ r_{\mathrm{E}}(3)}{r_{\mathrm{B2}}(3)}. \tag{3.25}$$

The CoG in x-direction is fixed as well and the *Balance mass* is given by

$$m_{\mathrm{BM}} = \frac{-m_{\mathrm{Ba1}}\ r_{\mathrm{Ba1}}(1) - m_{\mathrm{Ba2}}\ r_{\mathrm{Ba2}}(1) + m_{\mathrm{E}}\ r_{\mathrm{E}}(1) + m_{\mathrm{B2}}\ r_{\mathrm{B2}}(1)}{r_{\mathrm{BM}}(1)}. \tag{3.26}$$

The remaining masses are the *Comparison masses* and they are given by

$$4\ m_{\mathrm{C1}} = m_{\mathrm{chassis}} - (m_{\mathrm{B1}} + m_{\mathrm{B2}} + m_{\mathrm{Ba1}} + m_{\mathrm{Ba2}} + m_{\mathrm{E}} + m_{\mathrm{BM}}) \tag{3.27}$$

with

$$m_{\mathrm{C1}} = m_{\mathrm{C2}} = m_{\mathrm{C3}} = m_{\mathrm{C4}}. \tag{3.28}$$

The x-position r_x of the *Comparison mass* 1 and 2 are the same of mass 3 and 4 but with opposite sign. That is the reason why they do not change the CoG position. The position r_x in x-direction is only dependent on the moment of inertia about the z-axle and can be determined by

$$r_x = \sqrt{\frac{\Theta_{zz} - \Theta^s_{zz}}{4\ m_{\mathrm{C1}}}}. \tag{3.29}$$

The y-position of the *Comparison masses* can be determined in the same way but they are only depend on the moment of inertia about the x-axle and is given by

$$r_y = \sqrt{\frac{\Theta_{xx} - \Theta^s_{xx}}{4\ m_{\mathrm{C1}}}}. \tag{3.30}$$

Θ^s_{zz} and Θ^s_{xx} are the moment of inertia of the simplified model without the *Comparison masses*.

Table 3.6: Elements and data for moment of inertia tensor of the chassis

Elements for inertia tensor determination				
Element	**Index** i	**Position vector** r_i	**Dimension** d_i	**Mass** m_i
Body1	B1	$[0.016\ 0\ 0]$ m	4.85 m × 1.65 m × 0.52 m	596.5 kg
Body2	B2	$[-0.79\ 0\ 1.3]$ m	3.24 m × 1.65 m × 1.04 m	63.7 kg
Battery 1	Ba1	$[-0.851\ 0\ 0.119]$ m	0.35 m × 0.9 m × 1.03 m	334.3 kg
Battery 2	Ba2	$[-0.251\ 0\ -0.336]$ m	1.55 m × 1.38 m × 0.12 m	265.7 kg
Engine	E	$[1.584\ 0\ -0.226]$ m	R135 mm × 630 mm	148.9 kg
Balance mass	BM	$[1.584\ 0\ -0.226]$ m	0 × 0 × 0	104.6 kg
Compensation mass 1	C1	$[1.85\ 0.8\ 0]$ m	0 × 0 × 0	250 kg
Compensation mass 2	C2	$[1.85\ -0.8\ 0]$ m	0 × 0 × 0	250 kg
Compensation mass 3	C3	$[-1.85\ 0.8\ 0]$ m	0 × 0 × 0	250 kg
Compensation mass 4	C4	$[-1.85\ -0.8\ 0]$ m	0 × 0 × 0	250 kg
			Sum:	2513.7 kg

The evaluation of this parameters leads to a moment of inertia tensor of

$$\boldsymbol{\Theta}_{\text{chassis}} = \begin{bmatrix} 1080 & 0 & 168 \\ 0 & 5871 & 0 \\ 168 & 0 & 6525 \end{bmatrix} \text{kgm}^2. \tag{3.31}$$

3.2 Tires

Mass and moment of inertia tensor

The mass of the *BMW Aluminium rim Y-Spoke 211* according to [9] is

$$m_{\text{rim}} = 16.4 \text{ kg} \tag{3.32}$$

and the measured weight of the new tire *P255/50 R19 Uniroyal Rainsport3* is 14.46 kg. The measured weight loss after the tire measurement on the test bench was about 380 g [7]. Therefore, an average tire weight including the tire wear is estimated by

$$m_{\text{tire}} = 14.3 \text{ kg}. \tag{3.33}$$

The simplified inertia tensor of the rim is taken from a hollow cylinder with the same mass and dimensions. The length of the cylinder is 255 mm the external diameter is 241 mm, the internal is 191 mm and the y-axle is the rotation axle. By using Equations 3.1 to 3.7 and Table 3.2, the moment of inertia tensor is

$$\boldsymbol{\Theta}_{\text{rim}} = \begin{bmatrix} 0.48 & 0 & 0 \\ 0 & 0.78 & 0 \\ 0 & 0 & 0.48 \end{bmatrix} \text{kgm}^2. \tag{3.34}$$

The inertia tensor of the tire will be determined by a more precise model. The density of the composite material of rubber and steel is not homogenous. The approach is to

cut an old tire and measure the weight of the single parts. The chosen model is made out of five sub-models, depicted in Figure 3.3. One is a hollow cylinder, representing the tire tread, two are rings for the bead and two discs are representing the side walls.

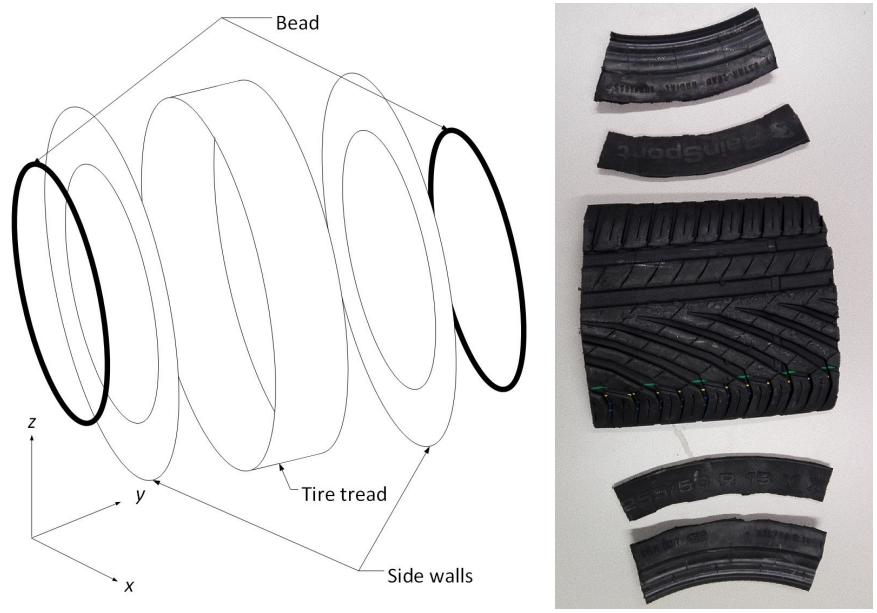

(a) Tire model for moment of inertia computation

(b) Cut tire, tire tread (center), side wall, bead (outside) for tire model

Figure 3.3: Tire model and mass identification of each part

Table 3.7: Mass and diamension of tire model

Element	**External radius**	**Internal radius**	**Length**	**Mass**
Tire tread	369 mm	353 mm	255 mm	9.36 kg
Side wall	353 mm	251.5 mm	5 mm	0.7 kg
Bead	251.5 mm	–	–	1.74 kg

The side walls and the tire tread are shifted about the half length of the tire tread in y-direction. The required equations can be found in Equations 3.1 to 3.7 and in Table 3.2. The rotation axle is the y-axle. Therefore, the moment of inertia tensor is given by

$$\boldsymbol{\Theta}_{\text{tire}} = \begin{bmatrix} 0.92 & 0 & 0 \\ 0 & 1.57 & 0 \\ 0 & 0 & 0.92 \end{bmatrix} \text{kgm}^2. \tag{3.35}$$

TMeasy parameters

The tire parametrisation and measurement at the *IABG* test bench in Munich was done

by *Klaus Esser* and the results are given in his report[7]. The Figures (a),(b) and (c) 3.4 depict the longitudinal force, lateral force and aligning torque of different wheel loads of the measurements and Figure (d) 3.4 shows the test bench.

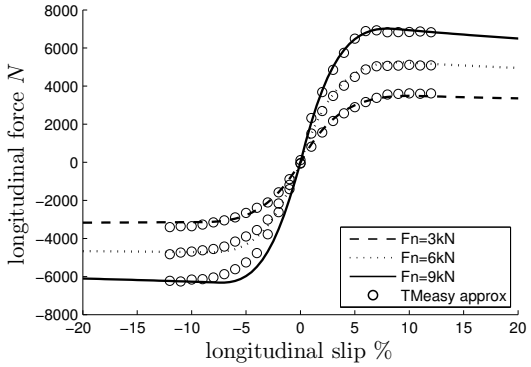

(a) Longitudinal force[7]

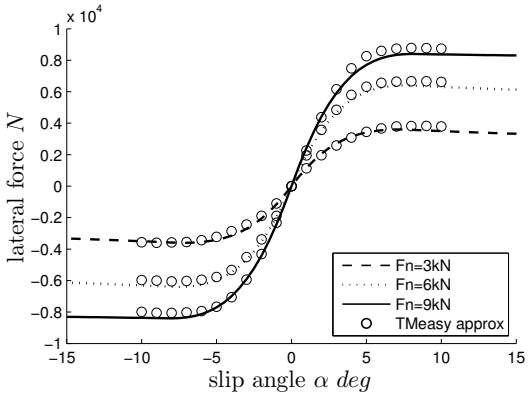

(b) Lateral force [7]

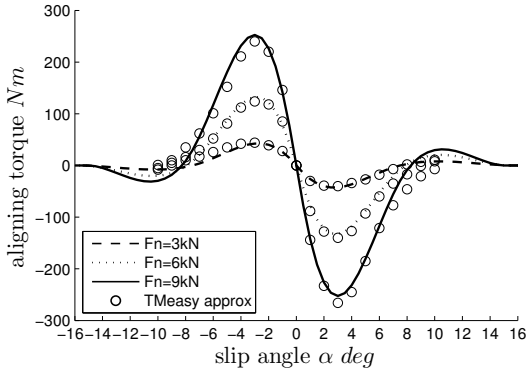

(c) Aligning torque [7]

(d) *IABG* testbench in Munich [7]

Figure 3.4: Measured and *TMeasy* approximated data of the tire: *Uniroyal Rainsport3 P255/50 R19*

3.3 Front suspension

Mass and moment of inertia tensor

An accurate way to measure the weight of the suspension would be to remove it from the prototype and put it on a scale. This approach requires a lot of effort and time in

the workshop. Furthermore, it gives no information about the inertia tensor.
Another way would be the use of a *Computer Aided Design*(CAD) model to determine the inertia tensor of the suspension. This approach requires a lot of designing effort.
However, the weights of each element can be found in a parts catalog. Additionally, the moment of inertia tensor can be determined by building up a simple model and use the information of the parts catalog.

Front suspension mass

The part catalog is taken from *Auto Leebmann GmbH* [9]. There are about 80 parts listed and some of the parts are attached either to the chassis or to the suspension or to both. Therefore, three different weight distribution factors are defined.
Either 100 % or 50 % or 0 % of their weight is added to the suspension. Some examples are given: the wheel carrier has the factor 100% because it is completely located on the suspension, the upper control arm has 50 % because it is attached to the chassis as well as to the wheel carrier and the bearing between the upper control arm and the chassis has 0 % because it is completely attached to the chassis. This leads to a front suspension weight of

$$m_{\text{frontsusp}} = 45.4 \text{ kg}. \tag{3.36}$$

Front suspension moment of inertia tensor

The simplified model for the determination of the front suspension inertia tensor is depicted in Figure 3.5.

The Table 3.8 shows the variable names of the simplified model.

Table 3.8: Dimensions of simplifed front suspension model, Figure 3.5

$g1$	Wheel center to connection point upper control arm
$g2$	Wheel center to connection point of lower links
$g3, g4$	Position of tie rod connection point
$g5$	Mean width of wheel carrier
$g6$	Mean thickness of wheel carrier
$g7$	Distance between wheel center and wheel carrier
$g8$	External radius of brake disc and wheel hub body
$g9$	Internal radius of brake disc and wheel hub body

For each element of the part catalog a distribution factor is allocated for one of these point masses or bodies and is depicted in Table 3.9.

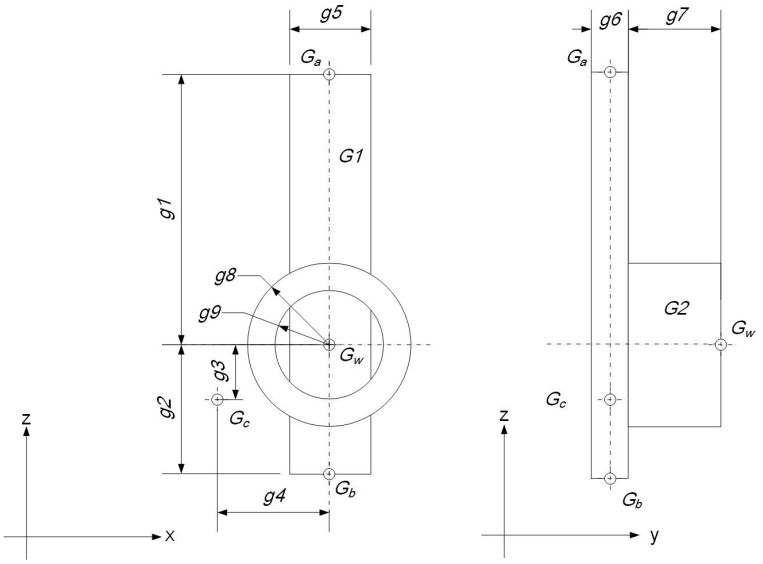

Figure 3.5: Simplified front suspension model for inertia tensor computation

Table 3.9: Elements of simplified front suspension model, see Figure 3.5

$G1$	Body, wheel carrier
$G2$	Body, brake disc and wheel hub body
G_a	Point mass, upper control arm connection point
G_b	Point mass, lower links connection point
G_c	Point mass, tie rod connection point
G_w	Point mass, wheel center

The equations to determine the inertia tensors of a cuboid and a cylindrical tube as well as the parallel axes theorem are given in Table 3.2. The estimated inertia tensor of the front suspension about the wheel center, without the wheel, is

$$\boldsymbol{\Theta}_{\text{frontsusp}} = \begin{bmatrix} 0.85 & -0.03 & -0.02 \\ -0.03 & 0.69 & -0.05 \\ -0.02 & -0.05 & 0.36 \end{bmatrix} \text{kgm}^2. \tag{3.37}$$

Connection points of front suspension

The measurement to determine the connection points were done by students of NTB Buchs [18] by using a portable measuring arm. These points were taken over except of the position of the wheel center, because it does not coincide with the track width of the vehicle.
The initial position of the suspension was found by measuring the height of the damper connection point, because it is a easy accessible joint.
The connection points are given for the *four-link* suspension. Therefore, the points for

the *double wishbone* suspension are the same except of the joint of the lower wishbone and the wheel carrier (point c, in Figure 2.3). A proper value for this point is the intersection of link *a1-b1* and link *a2-b2* (see Figure 2.4). Figure 3.6 depicts this virtual point c for the *double wishbone* suspension. The kingpin axis is defined by this intersection of point c and the point f of the upper control arm (see Figure 2.3).

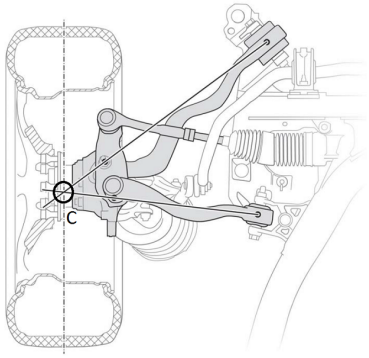

Figure 3.6: Intersection of links for *double wishbone* model [3]

Force elements

The spring rate c_s is constant, the damper coefficient d_d depends on the velocity and velocity direction of the damper v_damper and the anti-roll-bar rate c_arb is constant as well. The respective values of them are provided by internal documents of BMW. The spring rate of the bump stop c_d is unknown and estimated by 10 % of the front spring rate.

Figure 3.7: Wheel vector system *Kistler RV-4* [10]

Kinematic validation

The measurement for the validation of the front suspension models was done with the wheel vector sensors *Kistler RV-4* , depicted in Figure 3.7 and was carried out by a measurement engineer from the University of Technology Graz.

Figure 3.8 depicts the comparison of the wheel center movement of a stationary steering

maneuver of the *four-link* suspension, the *double wishbone* suspension and measurement data. Additionally, two set-ups for the suspension models are provided. One is the original set-up and the second one is with a distance plate of 35 mm between the wheel and the wheel carrier. This distance plate is called *spacer* and extends the front track wide from 1.644 m to 1.714 m.
The front wheels were placed on moveable plates to avoid deformations of the wheels and the suspensions. The procedure of the measurements was as follows: from zero degree steering angle to maximum left and afterwards to maximum right and back to zero degree. Figure 3.9 depicts the camber and toe angle of the this stationary steering maneuver but only with the original set-up because the spacer does not effect these angles.

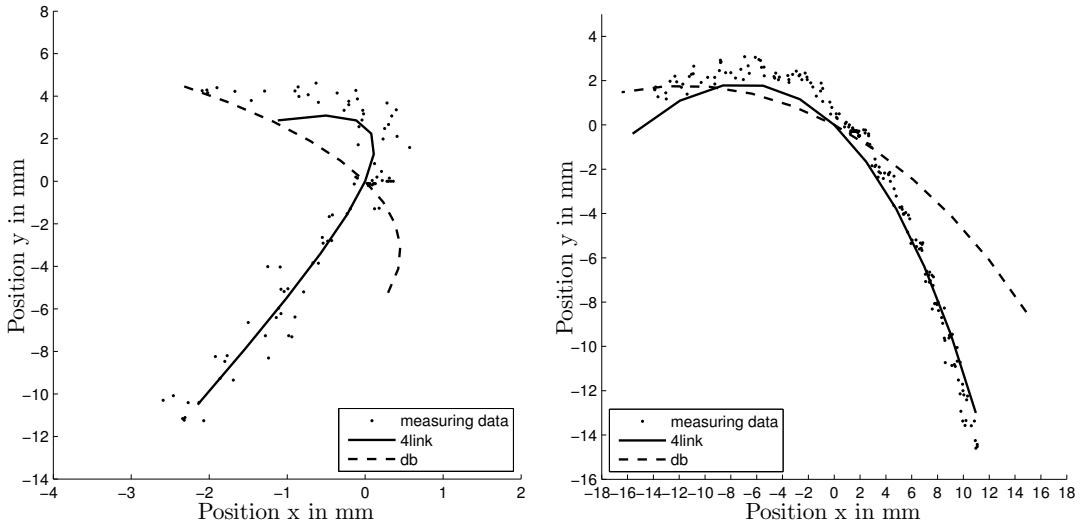

(a) Wheel center trajectory in xy-plane, original set-up

(b) Wheel center trajectory in xy-plane, with spacer

(c) Wheel center trajectory in yz-plane, original set-up

(d) Wheel center trajectory in yz-plane, with spacer

Figure 3.8: Steering maneuver, trajectory of wheel center
Legend of the plots: 4link = *four-link* suspension, db = *double wishbone* suspension, measuring data from a stationary steering maneuver

Figure (a) and (b) 3.8 show that the simulated trajectory of the *four-link* suspension fits better than the *double wishbone* suspension trajectory with the measurement data.

Each spot of the measurement data represents one measured signal. Therefore, no filtering was done. The error of the *double wishbone* suspension at low steering angles is acceptable but at higher steering angles the error is too big. The preferred model is the *four-link* suspension because the vehicle dynamic simulations will be done with high steering angles on the limit of the vehicle.

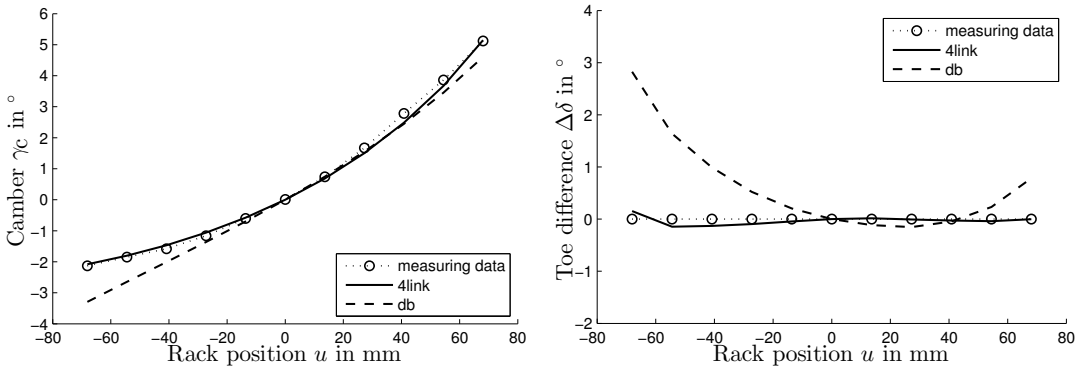

(a) Absolute camber angle

(b) Toe angle change

Figure 3.9: Steering maneuver, camber and toe angle

Figure (a) depicts the absolute camber angle and Figure (b) the toe angle minus the measured toe angle because the range of this angle is from $-22.05°$ to $24.6°$. This depiction shows the toe angle change explicitly due to the suspension kinematic.
Legend of the plots: 4link = *four-link* suspension, db = *double wishbone* suspension, measuring data from a stationary steering maneuver

Figure 3.9 depicts the camber and toe angle change. Again, the *four-link* suspension performs better than the *double wishbone* suspension. At low steering angles the *double wishbone* suspension trajectory is close to the measured signal but at higher steering angles the deviation is too big. For example, at a rack postion of -70 mm the measured steering angle is $-22.05°$, the simulated *four-link* steering angle is $-22.0°$ and the *double wishbone* steering angle is $-19.2°$. The error for this toe angle is less than 0.3 % for the *four-link* suspension and 13.2 % for the *double wishbone* suspension.

Figure 3.10 shows the trajectory of a stationary lifting maneuver of the *four-link* suspension, *double wishbone* suspension and measurement data of the original set-up. The reason why there are only figures with the original set-up is because there was almost no visible difference at the graphs.

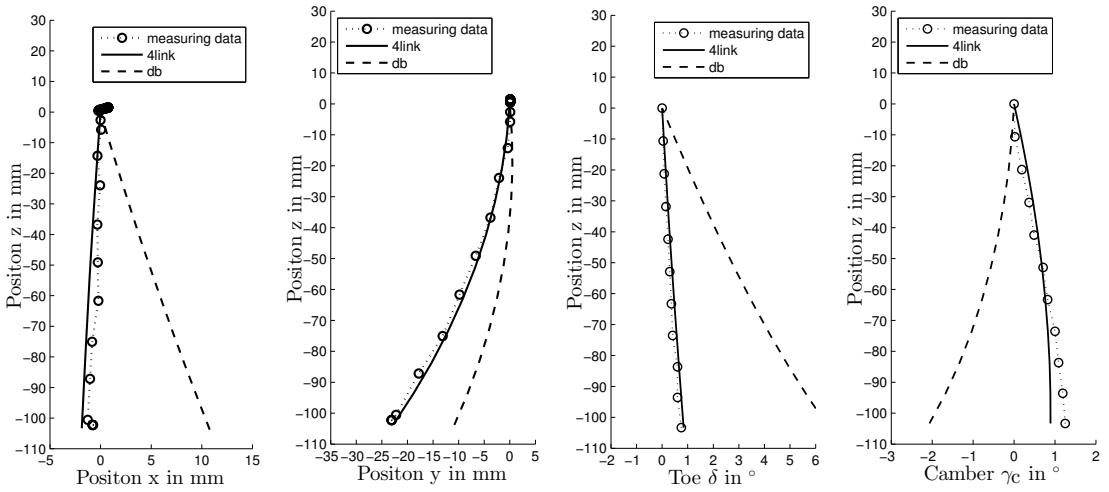

(a) Wheel center trajectory xz-plane, original set-up

(b) Wheel center trajectory yz-plane, original set-up

(c) Camber angle

(d) Toe angle

Figure 3.10: Lifting maneuver, trajetory of wheel center

Figures (a) depicts the absolute camber angle and Figure (b) the toe angle minus the measured toe angle because the range of this angle is from $-22.05deg$ to $24.6deg$. This depiction shows the toe angle change explicitly due to the suspension kinematic.
Legend of the plots: 4link = *four-link* suspension, db = *double wishbone* suspension, measuring data from a stationary lifting maneuver

Figure 3.10 confirms that the *four-link* suspension is the preferred model. The following vehicle dynamic simulations require a suspension model which is still accurate at high deflections. That is the reason why the *double wishbone* suspension is not accurate enough.

The *four-link* suspension performs at all validation maneuvers significantly better than the *double wishbone* suspension and is the preferred model. One advantage of the *four-link* suspension is because it considers the movement of the kingpin axle at a steering or lifting maneuver. Figure 3.11 depicts the travel of the intersection point c during a steering maneuver and only the *four-link* suspension is able to describe it. The stationary measurements were done with negligible longitudinal and lateral tire forces. Therefore, the elasto-kinematics effects were small.

3.4 Rear suspension

The determination of the rear suspension mass and the inertia tensor is done in the same way as shown in Chapter 3.3.

Mass and moment of Inertia Tensor

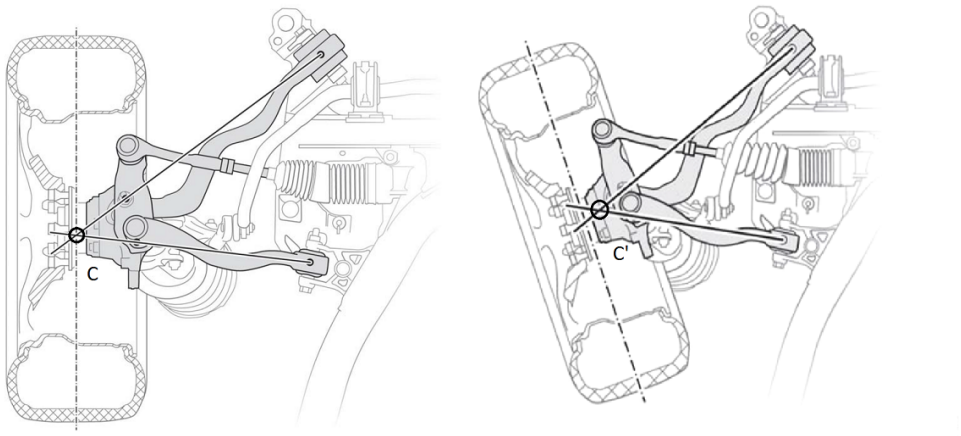

Figure 3.11: Movement of intersection point c to c' during a steering maneuver

Rear suspension mass

The determined mass of the rear suspension, without the wheel, is

$$m_{\text{rearsusp}} = 39.7 \text{ kg}. \tag{3.38}$$

Rear suspension moment of inertia tensor

The simplified model of the rear suspension is depicted in Figure 3.12.

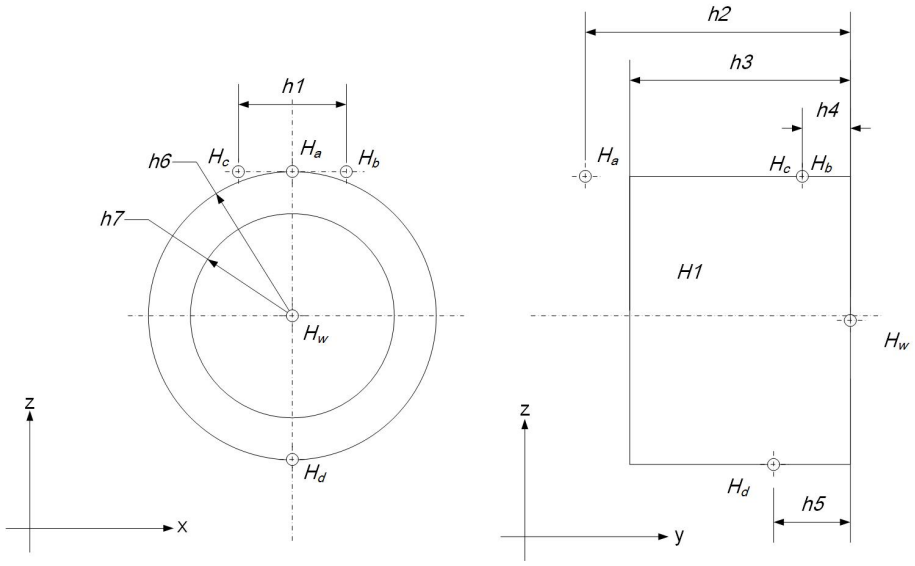

Figure 3.12: Simplified rear suspension model for inertia tensor computation

Table 3.10: Dimensions of simplfied rear suspension model, Figure 3.12)

$h1$	Distance between upper links at wheel carrier
$h2$	Position of spring attachment point at wheel carrier
$h3$	Length of wheel carrier
$h4$	Position of upper links at wheel carrier
$h5$	Mean position of lower wishbone
$h6$	External radius of wheel carrier
$h7$	Internal radius of wheel carrier

Each element of the part catalog is a distribution factor allocated for one of these point masses or bodies, which is depicted in Table 3.9.

Table 3.11: Elements simplified rear suspension model, see Figure 3.12

$H1$	Body, wheel carrier
H_a	Point mass of spring
H_b, H_c	Point mass of upper links
H_d	Point mass of lower wishbone
H_w	Point mass, wheel center

The equations to determine the inertia tensors of a cylindrical tube and the parallel axes theorem are given in Table 3.2. The estimated inertia tensor of the rear suspension about the wheel center, without the wheel, is

$$\boldsymbol{\Theta}_{\text{rearsusp}} = \begin{bmatrix} 0.85 & 0.01 & 0 \\ 0.01 & 0.34 & -0.01 \\ 0 & -0.01 & 0.75 \end{bmatrix} \text{kgm}^2. \tag{3.39}$$

Connection points of rear suspension

The position of the connection of the *integral IV* suspension are provided by students of the NTB Buchs like in Chapter 3.3. The position for the four rotation axles for the *planar double wishbone* suspension are determined by taking the mean value of point *a* and *b*, point *c* and *d*, point *g1* and *g2* as well as point *f1* and *f2*, depicted in Figure 2.9. The inclination of these four axes must be parallel for the *planar double wishbone* suspension, shown in Figure 2.7. Hence, the chosen angles are the average value of these four axes (distance of points *a*-*b*, *c*-*d*, *g1*-*g2* and *f1*-*f2*), which are already almost parallel. The aim is to modify only as less connection points as possible to guarantee a model, which is quite close to the real suspension.

The initial position of the suspension was found by measuring the height of the damper connection point and a trapezoid arm attachment point at the chassis.

Force elements

The spring rate c_s for the deflection is bigger than the rate for the rebound, the damper coefficient d_d depends on the velocity and velocity direction of the damper v_{damper} and the anti-roll-bar rate c_{arb} is constant. The respective values of them are provided by internal documents of BMW. The spring rate of the bump stop c_d is unknown and estimated by 10 % of the rear spring deflection rate.

Kinematic validation

The evaluation of the front suspension has a higher priority than the rear suspension, because of the higher impact on the torque vectoring steering. The *Wheel Vector System* was only available for the front suspension, that is the reason why the validation of the rear suspension was done in the workshop of TKP in Eschen by using a toe/camber angle measuring instrument, depicted in 3.13. A disadvantage of this approach is that the measurement gives only proper results for the rebound of the suspension. Figure 3.14 depicts the camber and toe angle changes over the z-position of the wheel center of the simulated *planar double wishbone* suspension, *integral IV* suspension and measuring data.

Figure 3.13: Measurement of toe and camber angle of rear suspension at TKP, Eschen

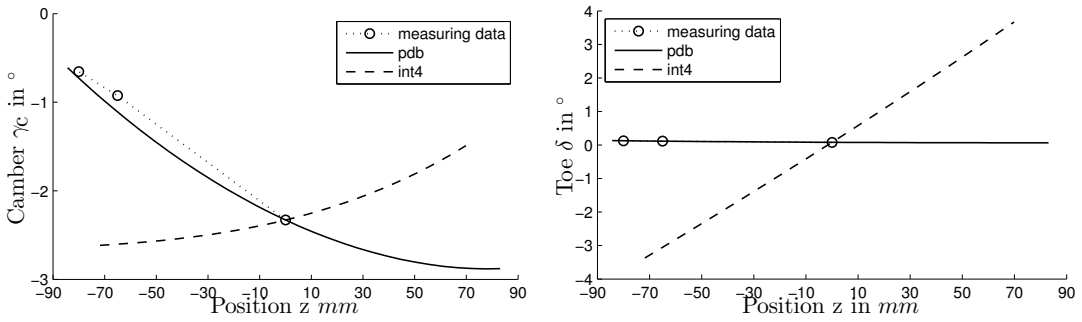

(a) Camber angle (b) Toe angle

Figure 3.14: Lifting maneuver of rear suspension, simulation and measurement data
Legend of the plots: pdb = *planar double wishbone* suspension, int4 = *integral IV* suspension, measuring data from a stationary steering maneuver

The suspension model validation shows that the *planar double wishbone* suspension is more suitable than the *integral IV* suspension. A reason for the poor performance of the *integral IV* suspension could be that the closed kinematic chain model is more complicated than the *planar double wishbone* suspension.
In general, closed kinematic chains with one DoF can have either one solution, multiple solutions or no solution for a certain movement. The present thesis deals only with movements and kinematic chains which have one, unique solution. Hence, a solution to solve these closed kinematic chains of the *integral IV* suspension requires big displacements of some links. These displacements lead to higher inclination angles of the wheel carrier than of the real model. The compliance of the real suspension compensates this effect. On the one hand, the real model has many elastic bushings and a very thin and flexible integral link and on the other hand it has a quite massive and strong arm like the control arm. At the selected modeling method all elements and joints are stiff, therefore a simplified model is better than a very detailed one. That is the reason why the *planar double wishbone* suspension performs better than the *integral IV* suspension. This shows that increasing the modeling complexity does not ensure an increasing accuracy of the simulation results.

3.5 Vehicle model validation

This chapter provides the model validation of the conventional SbW vehicle. Therefore, measurement and simulation data will be compared. There will be some parameters that might have higher deviations or are unknown, for example, the friction coefficient. It is possible to compensate these parameters by adjusting them. The goal is to get the same stationary driving behavior and reach the same maximum lateral acceleration. In addition, this chapter shows dynamic driving maneuvers used for the model validation.

Adjusting parameters for steering behaviour

One unknown parameter is the road friction coefficient μ. The *TMeasy* tire model has already a compensation factor for the different μ of the flat track and the road, which is provided in the report [7]. But this is not a constant, generally applicable factor and it depends among others on the test track and tire condition.
Another parameter which might have a wider range of variation is the position of the CoG in z-direction. The CoG position in x-direction and the vehicle weight were determined quite accurately. It is considered that they will remain constant. One reason why it is less precise to determine the CoG in z-direction is that the blocked tires can cause an unwanted load transfer while lifting. The blocked tires were necessary to ensure that the prototype vehicle stays on the table lift and does not roll down.
Figure 3.15 depicts the measurement data of left and right turns of 60 m constant radius maneuver. Additionally, it shows simulation data by using the original parameters, a low position of the CoG and a high road friction coefficient.

In Figure 3.15 and 3.16, on the abscissa the steering angle minus the ackermann steering angle are plotted. The Ackermann steering angle is defined as the quotient of the track width to the current cornering radius [6]. A straight line in the ordinate direction would be a neutral, to the left an understeering and to right an oversteering driving behavior. This kind of diagram is called handling diagramm.

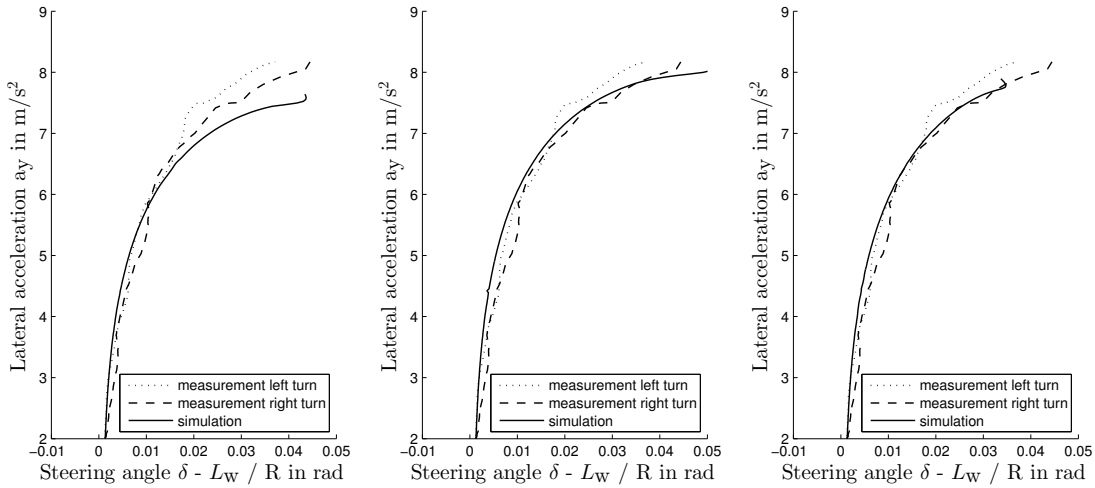

(a) Constant radius 60 m, original parameters (b) Constant radius 100 m, lower CoG (50 mm) (c) Ramp steer at 50 kph, higher road friction coefficient($\mu = 1.3$)

Figure 3.15: Steering behavior of conventional SbW vehicle, handling diagram
These figures depict measurement data of a left and right turn of a 60 m constant radius maneuver. Additionally, in Figure (a) the simulation data of the original set-up is depicted, in Figure (b) one with a lower CoG position and in Figure (c) one with a higher road friction coefficient.

A good choice for the road friction was 1.1 and for the CoG z-position 35 mm lower than the original one. Figure 3.16 depicts the measurement data of different maneuvers but with the slightly adapted parameters.

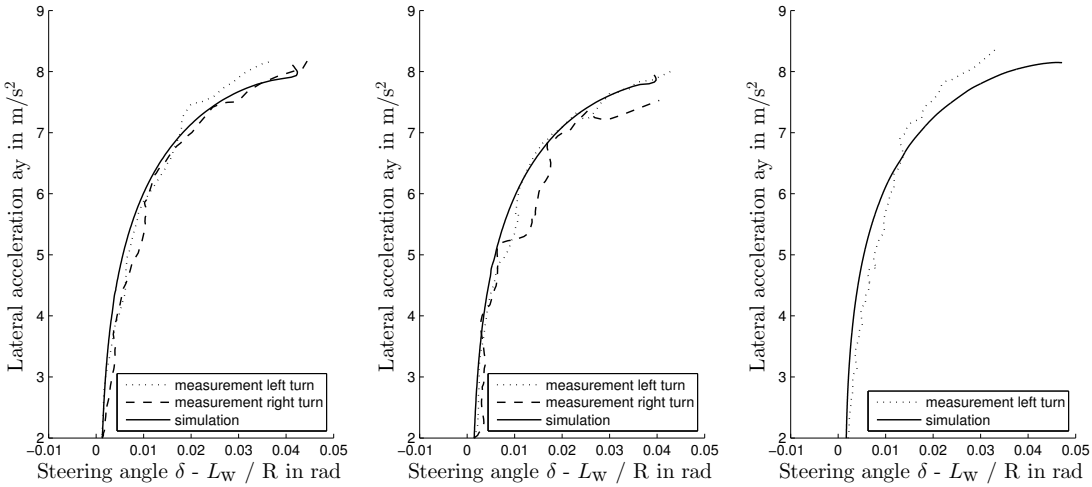

(a) Constant radius 60 m, improved parameters (b) Constant radius 100 m, improved parameters (c) Ramp steer at 50 kph, improved parameters

Figure 3.16: Steering behavior with improved parameters, handling diagram
Figures (a),(b) and (c) depict measurement and simulation data with the improved parameters. The road friction coefficient is 1.1 and the CoG z-position is 35 mm lower .

Dynamic maneuvers

This section provides the following maneuvers for the model validation:

- Double lane change
- Slalom maneuver
- Step steer

The input parameters for the simulation was the measured rack position u as well as a velocity profile of the test drives. The vehicle model has an integrated PI-controller to adapt the driving torques at the front axle to reach the desired velocity. There was no braking during the maneuvers necessary which simplified the simulations.

- **Double lane change at 40 kph**

The double lane change is the maneuver with the highest yaw acceleration of the available

test drive data. Therefore, more figures are provided than for the other maneuvers. Figure 3.17 depicts the lateral acceleration, the yaw rate and the roll rate over the time of the simulated and measured data.
The maximum lateral acceleration at the double lane change maneuver at 40 kph of the simulation is lower than the measured one. The yaw and roll rate of the simulation is close to the measurements and satisfy the requirements.

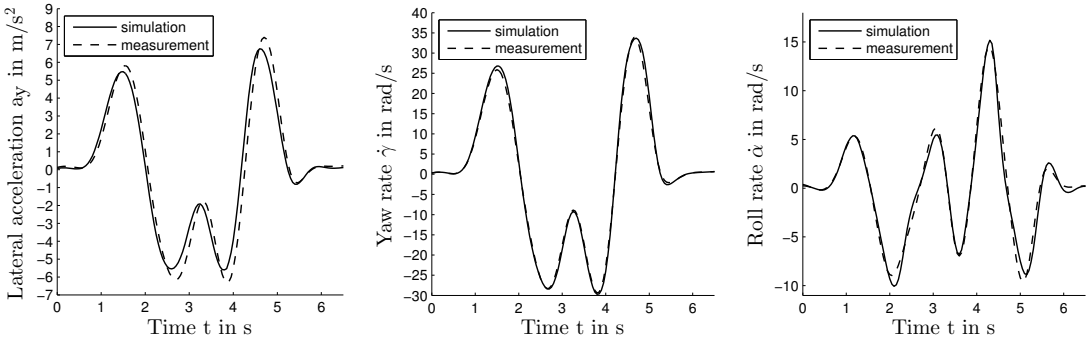

(a) Double lane change at 40 kph, lateral acceleration (b) Double lane change at 40 kph, yaw rate (c) Double lane change at 40 kph, roll rate

Figure 3.17: Double lane change, conventional SbW vehicle validation
Figures (a),(b) and (c) depicts measurement and simulation data from the conventional SbW vehicle. The input for the simulation was the rack position and a velocity profile for the PI-Speed-Controller

Figure 3.18 shows the measurement and simulation data from the suspensions. The first four plots depict the vertical movement of the suspension and the last two plots show the camber change of the front suspensions.
The simulated positions of the wheel centers $z1$ and $z2$ fit well to the measured positions and were measured with the wheelvector sensors. However, the simulated positions $z3$ and $z4$ at the rear suspensions have higher deviations but the characteristic is similar. A reason for these deviations is the used measurement method:
A linear potentiometer was attached at the lower trapezoid arm and the position of the wheel center was computed.
Therefore, the error chain of the measurements has to be considered. Many parameters had to be determined, for example, the inclination angle of the linear potentiometer, the attachment points of the potentiometer, the distance between the attachment points and the wheel center and so on. Additionally, some of these parameters change during the measurement. The measurement method of the wheelvector sensor is more accurate than the linear potentiometer method.
The simulated camber angle γ_c of the front left suspension is a bit higher than the measured angle and the front right angle is a bit lower but in general both are accurate enough.

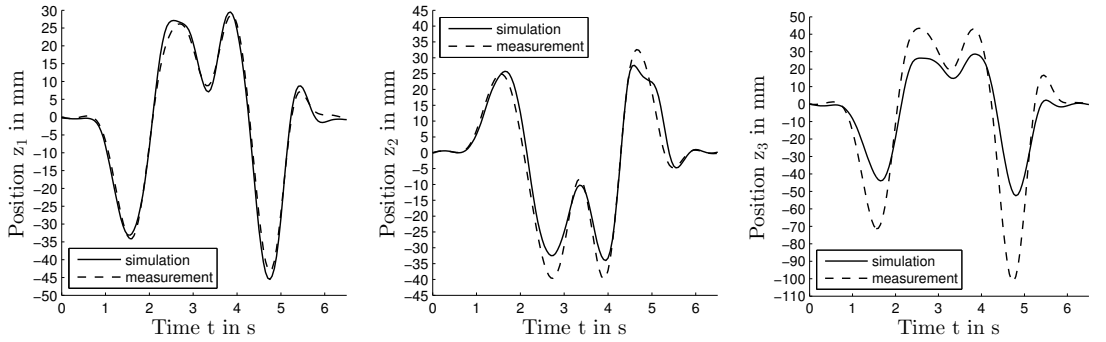

(a) Double lane change at 40 kph, vertical front left wheel position (b) Double lane change at 40 kph, vertical front right wheel position (c) Double lane change at 40 kph, vertical rear left wheel position

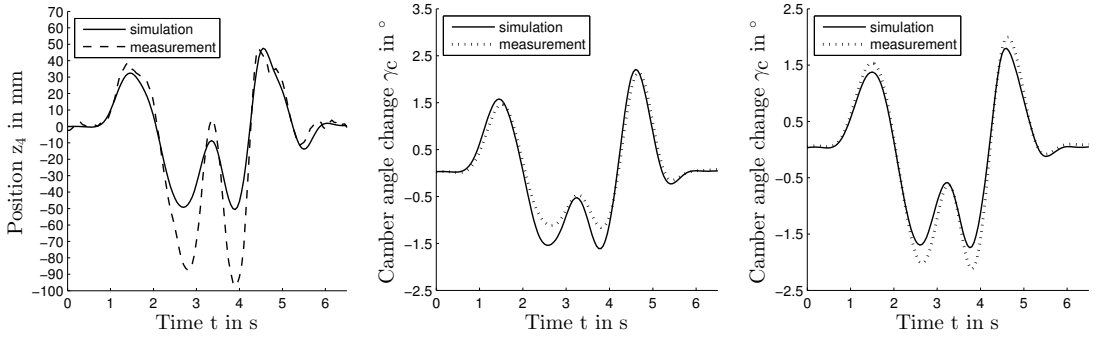

(d) Double lane change at 40 kph, vertical rear right wheel position (e) Double lane change at 40 kph, camber change front left wheel (f) Double lane change at 40 kph, camber change front right wheel

Figure 3.18: Double lane change, wheel state validation

Figures (a) to (d) depict the vertical movement of the wheel center of each wheel. Figure (e) and (f) depict the camber change of the front wheels. The input for the simulation was the rack position and a velocity profile for the PI-Speed-Controller.

- **Double lane change at 50 kph, slalom maneuver at 70 kph and step steer at 50 kph**

Figure 3.19 depicts measurement and simulation results of different driving maneuvers. These figures show only the lateral acceleration and the yaw rate, because these two values are significant for the lateral driving behavior.
The simulated lateral acceleration a_y of the slalom meneuver at 70 kph and of the step steer maneuver at 50 kph fit well. The simulated a_y of the double lane change at 50 kph has small deviations. Contrary results are given for the simulated yaw rate, because the double lane change maneuver fits well and the other ones are a bit higher.

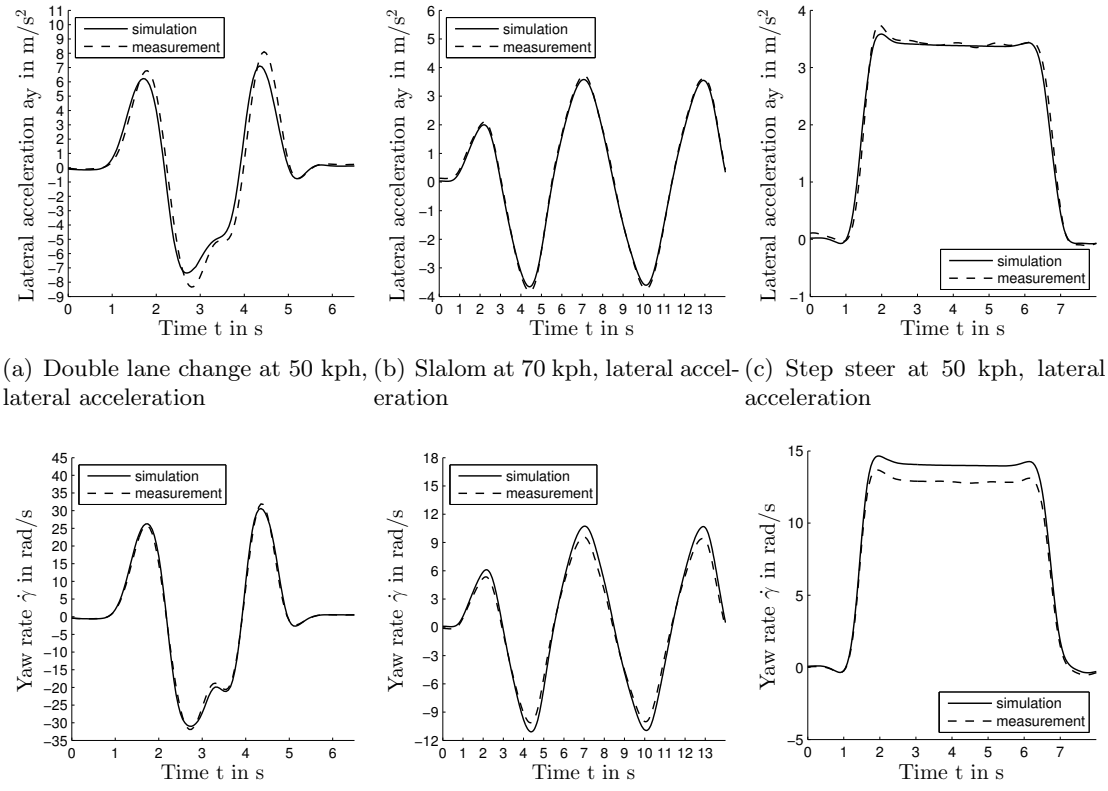

(a) Double lane change at 50 kph, lateral acceleration

(b) Slalom at 70 kph, lateral acceleration

(c) Step steer at 50 kph, lateral acceleration

(d) Double lane change at 50 kph, yaw rate

(e) Slalom at 70 kph, yaw rate

(f) Step steer at 50 kph, yaw rate

Figure 3.19: Conventional SbW vehicle validation

Figures (a),(b) and (c) depict measurement and simulation data from the conventional SbW vehicle. The input for the simulation was the rack position and a velocity profile for the PI-Speed-Controller.

In summary it can be said, that the conventional SbW model meets the requirements and builds up a good basis for the TV vehicle. The adjustment of μ and the CoG in z-direction lead to the same driving behavior, similar lateral acceleration, yaw rate, roll rate and front wheel positions at different driving maneuvers. The simulated rear wheel positions have higher deviations but the overall simulation results satisfy the requirements.

3.6 Vehicle model validation of torque vectoring mode

The second part of the model validation is about the TV model. The implementation of a TV steering is more complicated than a conventional steering system because the input parameter for a cornering maneuver is not the rack position but the driving torques.
The rack position of a conventional SbW vehicle is only dependent on the drivers input (as long as the actuator is strong enough). However, the rack position of a TV steered

vehicle is dependent on the suspension geometry, the tire forces, the tire torques, the vehicle state and the applied wheel torques. In general, all these factors can change at a cornering maneuver and therefore, it is more complicated to perform the desired driving maneuver.
There are two types of model validation: stationary driving maneuvers and dynamic driving maneuvers.

Stationary maneuvers

The steady state driving behavior is necessary to analyze the maximum acceleration and the steering tendency. In Section 3.5 the driving behavior is characterized by the steering angle minus the *Ackermann* steering angle. In that case, depicted in Figure 3.20 and 3.21, the rack position is plotted on the abscissa for two reasons. The first one is because there are no measurement data available for the steering angle but for the rack position. The second one is because the rack position is more universal as the steering angle because it is not influenced by the steering geometry or elasto-kinematics effects. Compared to Section 3.5 only a ramp steer maneuver is provided, because the measurement data of the constant radius maneuver oscillate too much.

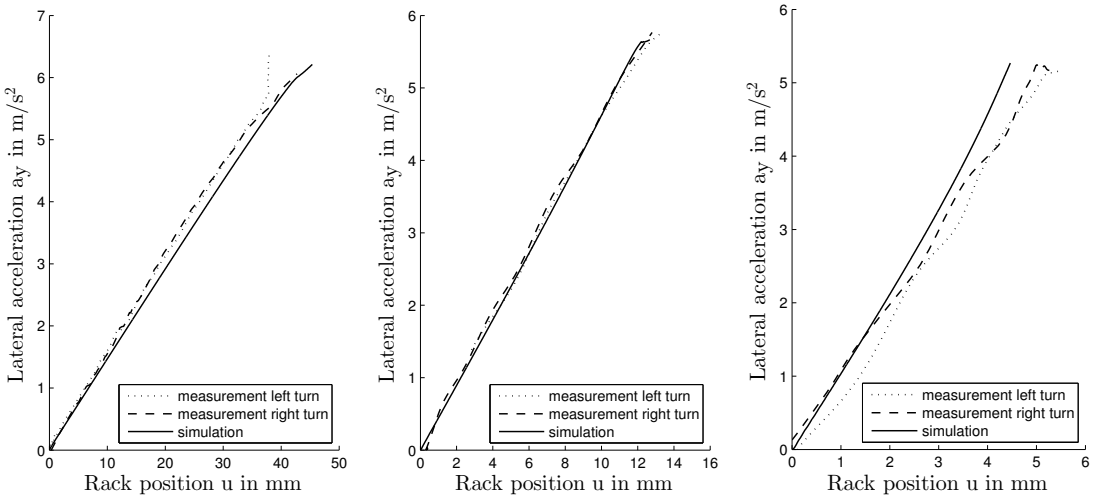

(a) Ramp steer maneuver at 30 kph, lateral acceleration (b) Ramp steer maneuver at 50 kph, lateral acceleration (c) Ramp steer maneuver at 70 kph, lateral acceleration

Figure 3.20: Driving behavior TV vehicle

Figures (a),(b) and (c) depict measurement and simulation data from a TV SbW vehicle at different velocities. On the abscissa the rack position is plotted. The maximum rack displacement is about 80 mm to the left and to the right. These figures express the steering tendency and the maximum acceleration. The measurement and simulations were done with a spacer at the front wheels.

The reason for these oscillations is because it is a challenge for the driver to perform this maneuver. The driver tries to drive at a constant radius and increases the velocity slowly. The TV steering is not as sensitive and accurate as the conventional SbW steering and

therefore, it is difficult to do a constant radius maneuver. Additionally, the TV steering has a small delay after a steering input. That is the reason why a ramp steer maneuver is more significant for the model validation than a constant radius maneuver.

Figure 3.21 depicts the torque difference of the front wheels over the rack displacement of test drives and simulations. This validation plots are an indicator how effective the TV steering is.

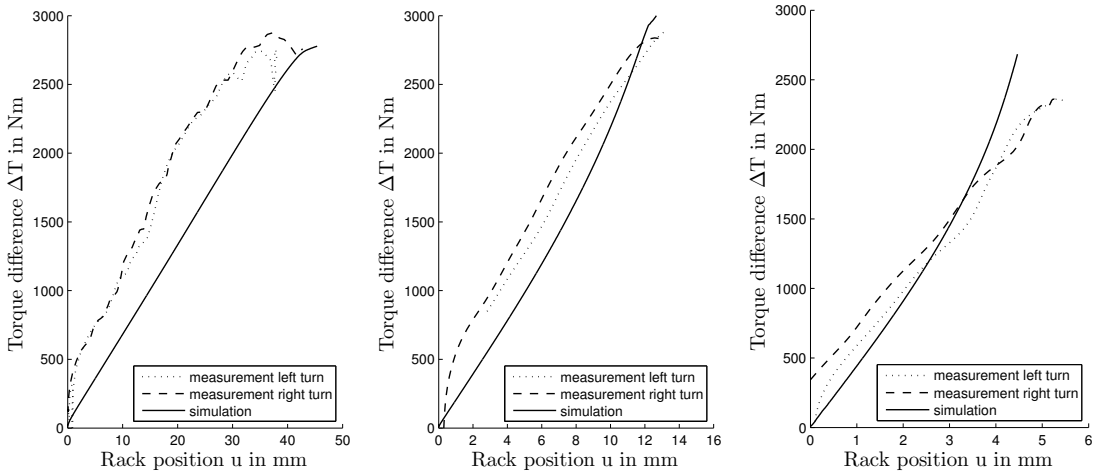

(a) Ramp steer maneuver at 30 kph (b) Ramp steer maneuver at 50 kph (c) Ramp steer maneuver at 70 kph

Figure 3.21: Torque difference of TV vehicle

Figures (a),(b) and (c) depict measurement and simulation data from a TV vehicle at different velocities. On the abscissa is the rack position plotted. The maximum rack displacement is about 80 mm to the left and to the right. These figures express the steering tendency and the maximum acceleration. The measurement and simulations were done with a spacer at the front wheels.

The maximum torque at each wheel is 1680 Nm. Hence, the theoretical maximum torque difference is 3360 Nm. But there is also a certain torque required to overcome the drag forces and to keep a constant speed level. In other words, the average torque of the wheels must be big enough to ensure a certain velocity. Additionally, the power of the engines are limited and is one of the reasons why in Figure (a) 3.21 the maximum torque difference of the measurement data is lower than in Figure (c) 3.21, where the vehicle velocity is 40 kph higher. These circumstances explain the main discrepancy of the measurement data. The simulations were done without power restrictions, because the aim is to analyze the driving behavior.

Dynamic maneuvers

This section provides the following maneuvers for the model validation:

- Slalom maneuver at 30 kph
- Slalom maneuver at 70 kph
- Step steer at 50 kph

The input parameter for the simulation is the torque difference of the measurements. One challenge is to ensure the same speed level because a slightly difference at the drag forces causes an acceleration or deceleration of the vehicle. If that happens, it is not possible to compare the measured and simulated data. To avoid this phenomenon, the input of the simulation was only the measured torque difference and an integrated PI-controller added the required torque equally distributed to the front wheels.

- **Slalom maneuver at 30 kph**

The slalom maneuver is an appropriate maneuver for the TV model validation because it is dynamic, simple and the measurement data are barely influenced by oscillations of the controller. Figure 3.22 depicts the measurement and simulation data of a 30 kph slalom maneuver. The simulated lateral acceleration, yaw rate and rack position are all about the the same factor higher than the measurements.

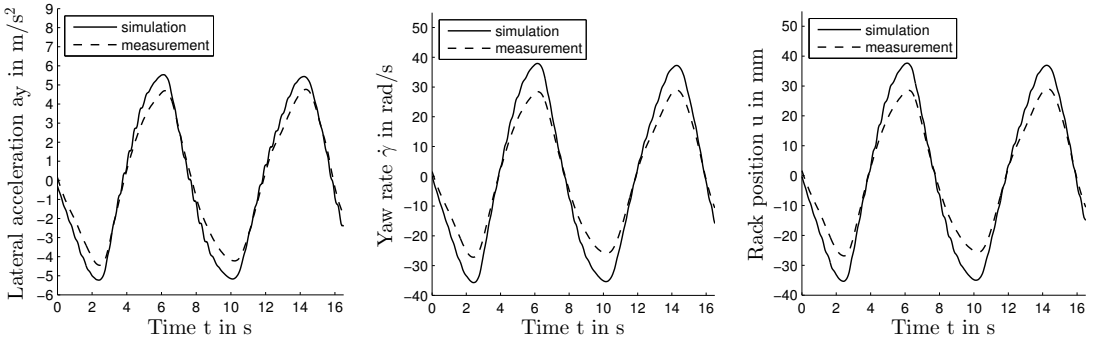

(a) Slalom maneuver at 30 kph, lateral acceleration (b) Slalom maneuver at 30 kph, yaw rate (c) Slalom maneuver at 30 kph, rack position

Figure 3.22: Sine input 30 kph, TV vehicle

Figure (a) depicts the lateral acceleration, Figure (b) the yaw rate and Figure (c) the rack position of a TV vehicle. The input for the simulation are the torque difference at the front wheels and a velocity profile for the PI-speed-controller.

- **Slalom maneuver at 70 kph**

Figure 3.23 depicts the measurement and simulation data of a 70 kph slalom maneuver. Compared to Figure 3.22 the simulation is closer to the measurement at 70 kph.

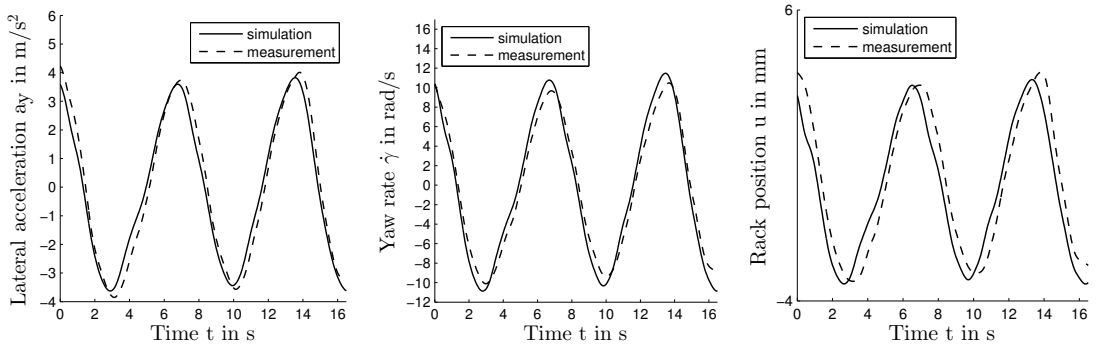

(a) Slalom maneuver at 70 kph, lateral acceleration (b) Slalom maneuver at 70 kph, yaw rate (c) Slalom maneuver at 70 kph, rack position

Figure 3.23: Sine input 70 kph, TV vehicle

Figure (a) depicts the lateral acceleration, Figure (b) the yaw rate and Figure (c) the rack position of a TV vehicle. The input for the simulation are the torque difference at the front wheels and a velocity profile for the PI-speed-controller.

- **Step steer at 50 kph**

Additionally to the slalom maneuvers a step steer input is provided. Figure 3.24 shows measured and simulated data of this maneuver.
The maximum value of the simulated lateral acceleration, yaw rate and rack position fit well with the measurements but the measurements has a higher delay. This delay is typically for the TV steering and it was noticed by drivers at test drives. The delay of the simulated signals is lower.

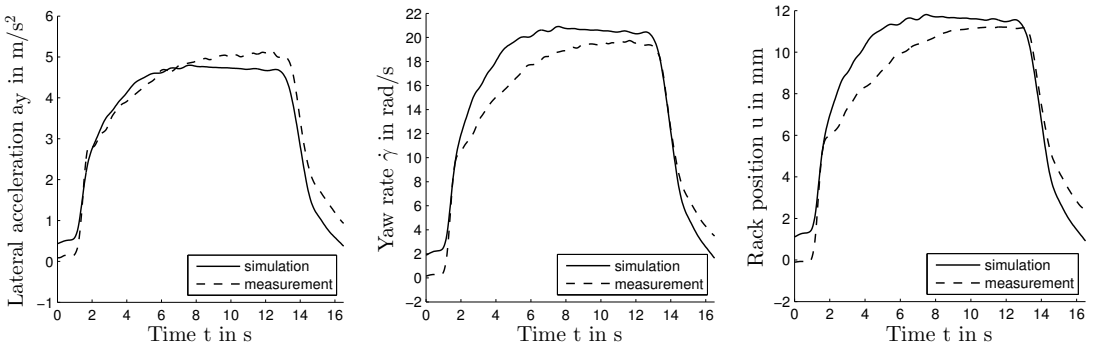

(a) Step steer maneuver at 50 kph, lateral acceleration

(b) Step steer maneuver at 50 kph, yaw rate

(c) Step steer maneuver at 50 kph, rack position

Figure 3.24: Step steer 50 kph, TV vehicle

Figure (a) depicts the lateral acceleration, Figure (b) the yaw rate and Figure (c) the rack position of a TV vehicle. The input for the simulation are the torque difference at the front wheels and a velocity profile for the PI-speed-controller.

Summing up the results, the accuracy of the stationary and dynamic simulations depends on the velocity.
The focus of the stationary ramp steer maneuver was on the validation of the lateral acceleration and on the required wheel torques. The ramp steer simulations show that the TV model performs better at 50 kph than at 70 kph.
The focus of the dynamic simulation was on the lateral acceleration, yaw rate and rack position. The dynamic simulations show that the TV model performs better at a velocity of 70 kph than of 30 kph. A reason for that might be the inaccurate estimated parameters, like the rack friction and the rack damping coefficient. These parameters were taken from an internal TKP project. The next step to improve the TV vehicle model would be to conduct further research on the rack model.
However, the TV model validation satisfies the requirements and can be used for further investigations.

4 Analysis of torque vectoring

This section focuses on a basic parameter study of the TV model. Section 3.5 was about the model validation of the conventional SbW vehicle and shows that the vehicle model itself satisfies the requirements and is able to describe the dynamic vehicle driving behavior.
The next step was the validation of the TV model which was extended by the rack position as one more DoF. The TV model requires a proper tire model which is able to take combined tire forces and camber changes into account. It is also important to have a proper suspension and steering model in order to consider three-dimensional force and torque vectors in the wheel center. In general, the rack position is dependent on those vectors. This is the reason why a three-dimensional multi-body vehicle model is needed. Of course, a simplified vehicle model might be good enough and can be tuned to get the desired results. However, the aim is to understand this steering system even for a multi-link suspension, where the kingpin axle changes its inclination angle during a steering maneuver. Therefore, the whole balance of forces and torques is changed.
The validation of the TV model in Section 3.6 depicts that the simulation results satisfy the requirements for a model which can be used for basic vehicle dynamic investigations. This section proceeds with further investigations and analyzes the impact of selected parameters on the TV model and on the conventional vehicle model.
The defined set-ups will always be provided in the same pattern with four different plots to make the comparison clear.

4.1 Set-up

The aim is to consider parameters which can be modified at the real prototype vehicle without extra work. Theoretically, there are hundreds of parameters that can be changed, but the focus is on basic vehicle and suspension parameters.

The Table 4.1 depicts the nine defined set-ups and each one is separately analyzed in the subsections.

Table 4.1: Set-ups for TV model analysis

Set-ups for parameter study of the TV model			
Nr.	**Set-up name**	**Name**	**Range from ... to ...**
1	Distance plate, spacer	sp	-20 mm to +50 mm
2	Front and rear ARB rate	c^f_{arb},c^r_{arb}	$2 \times c^f_{arb}$,$0 \times c^r_{arb}$ to $0 \times c^f_{arb}$,$2 \times c^r_{arb}$
3	Upper control arm point f in x-direction	$r_{f,F}(1)$	-50 mm to +50 mm
4	Upper control arm point f in y-direction	$r_{f,F}(3)$	-50 mm to +50 mm
5	Initial toe angle of front wheels	δ_{in}	$-1°$ to $+1°$
6	Initial camber angle of front wheels	$\gamma_{c,in}$	$-2°$ to $+2°$
7	CoG position in x-direction	$r_{CoG,F}(1)$	42/58 to 50/50 weight balance
8	CoG position in z-direction	$r_{CoG,F}(3)$	-100 mm to +100 mm
9	Tire cornering stiffness	c_α	80 % to 120 % of initial value

4.2 Parameter variation

The Table 4.2 depicts the pattern for the figures in this section. These figures should give an idea of the potential of the set-ups. The parameters have not been optimized. The first point is to show the efficiency and the power of the TV steering. The second one is to predict the driving behavior of the conventional and the TV vehicle.

Table 4.2: Pattern for the paramter variation figures

TV model Ramp steer maneuver at 50 kph *Torque difference* over *Lateral acceleration*	**TV model** Sine input at 50 kph *Lateral acceleration* over *time*
TV model Ramp steer maneuver at 50 kph *Lateral acceleration* over *steering angle - Ack**	**Conventional SbW model** Ramp steer maneuver at 50 kph *Lateral acceleration* over *steering angle - Ack**

*Ackermann steering angle

The figure in the first row and first column at Table 4.2 indirectly shows the efficiency of the set-up. It depicts how much torque difference is required to obtain a certain lateral acceleration. By analyzing this plot, it is important to have a look on the driving behavior, because it might be quite oversteering and hard to handle the vehicle. Therefore,

the steering tendency is provided in the figure in the second row and first column. Additionally, in the first row and second column a slalom maneuver is depicted to illustrate the dynamic behavior. For example, it considers the damper forces which do not occur at a steady state maneuver.
The figures in the second row express the driving behavior of the TV mode and the conventional mode. The trade-off to design a car which performs well in both modes will be a challenge for automotive engineers and is depicted in these figures.

1. Distance plate, spacer

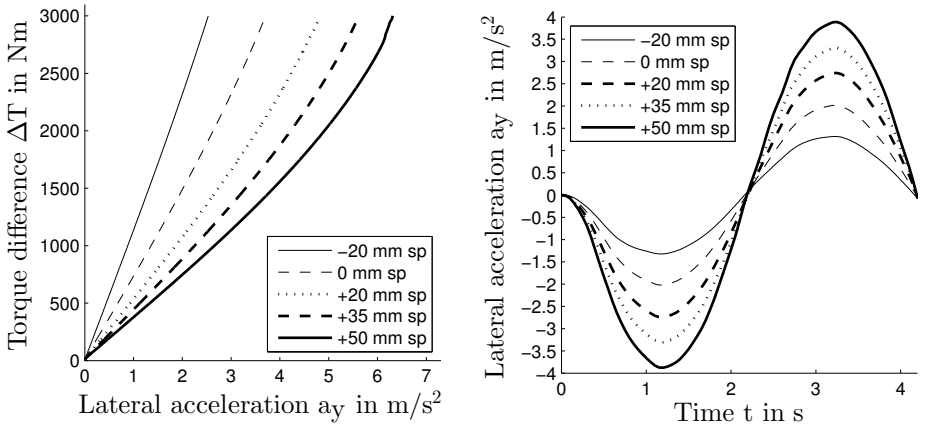

(a) TV mode, ramp steer at 50 kph (b) TV mode, slalom maneuver at 50 kph

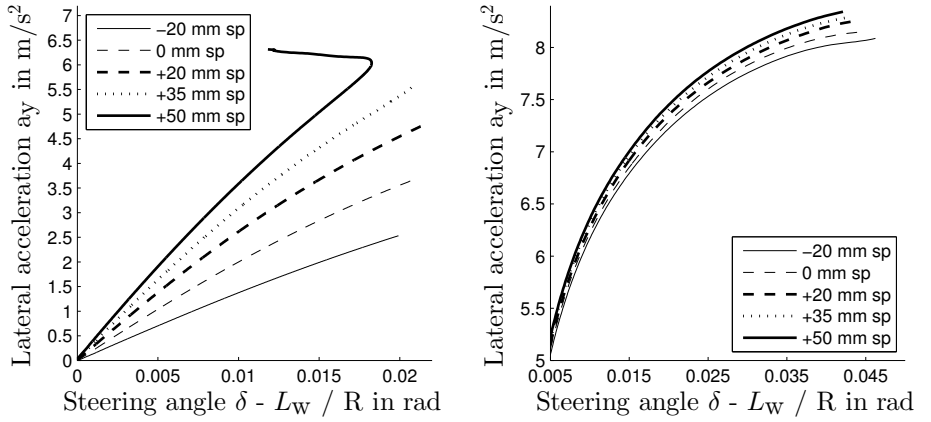

(c) TV mode, ramp steer at 50 kph (d) Conventional SbW mode, ramp steer maneuver 50 kph

Figure 4.1: Change of spacer thickness
Legend of the plot: sp = spacer, distance plate between wheel carrier and front wheel

The use of distance plates, so called spacers, were already used for the test drives for the model validation. Previous master theses, for example, [18] or the article [19] investigated

the effects of the spacer.
Spacers extent the scrub radius and make the TV steering more effective. It is the first point of the parameter study to depict the efficiency of the TV steering and to show the driving behavior of both modes. Moreover the spacer extension is an appropriate reference for further parameter variations, because it is already verified by test drives. The maximum spacer distance is limited by the installation space, especially the wheel case.

The maximum torque difference for the ramp steer maneuver is 3000 Nm. Additionally, a PI-controller adds an equally distributed driving torque at both front wheels to ensure the constant speed of 50 kph. The input rack position for the ramp steer maneuver in the conventional SbW mode ranges from zero to 27 mm. It is almost on the limit of the maximum possible lateral acceleration of the standard set-up.
The input for the slalom maneuver simulation is a sine torque signal which has an amplitude of 800 Nm and a frequency of 0.25 Hz at each wheel. Therefore, the maximum torque difference is 1600 Nm.

Figure (a) to (d) 4.1 depict the positive effects in each plot for a thicker spacer. It increases the maximum acceleration and produces a slightly more oversteering vehicle in the TV and conventional SbW mode.

2. Front and rear ARB rate

The change of an anti-roll-bar at the prototype can be done with little effort. The attachment points are easily accessible and BMW spare-part-dealers offer a wide range of anti-roll-bars.

Figure (d) 4.2 depicts the positive effects of a strong rear anti-roll-bar in order to increase the maximum lateral acceleration for the conventional SbW vehicle. Compared to Figure (d), 4.2 Figure(c) gives the TV model a more understeering and in the conventional mode a more oversteering driving behavior. This contrary performance is a challenge for optimizing both modes. Figure (b) 4.2 depicts a slightly higher lateral acceleration at the slalom maneuver for the strong front anti-roll-bar. This could be because of the more oversteering driving behavior of the vehicle. Figure (a) 4.2 does not show any remarkable differences.

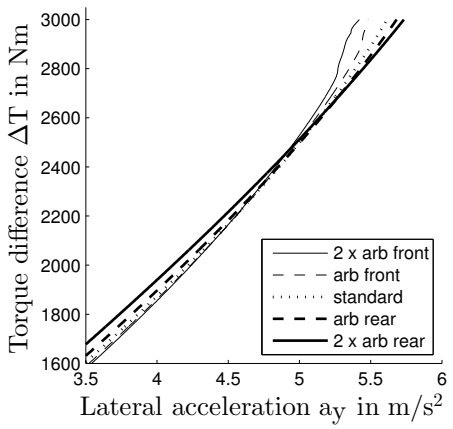

(a) TV mode, ramp steer maneuver at 50 kph

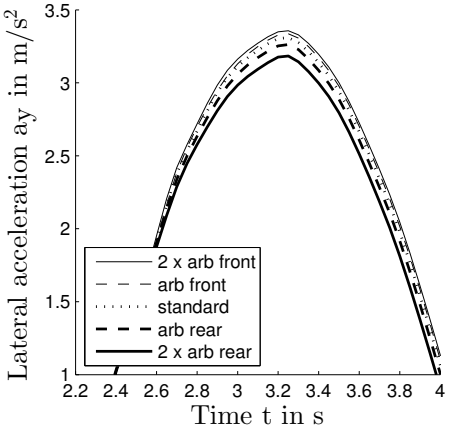

(b) TV mode, slalom maneuver at 50 kph

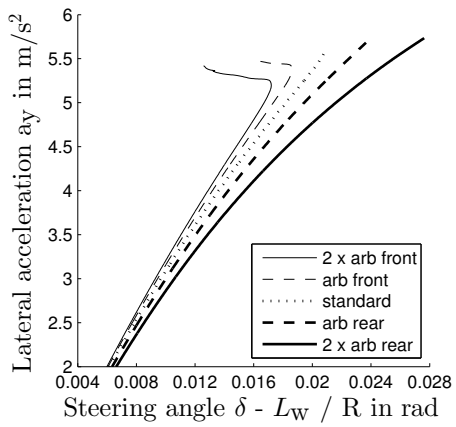

(c) TV mode, ramp steer maneuver at 50 kph

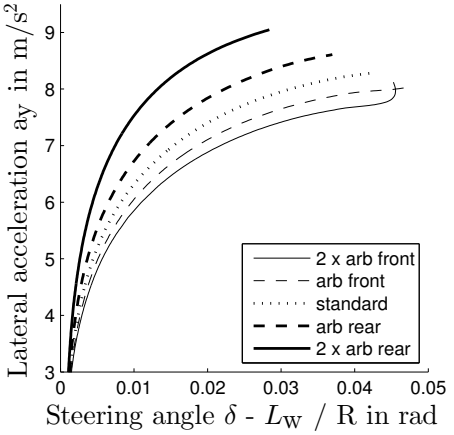

(d) Conventional SbW mode, ramp steer maneuver at 50 kph

Figure 4.2: Change of the anti-roll-bar rate

3. Upper control arm point *f* in x-direction

Figure 4.3 depicts the point f and the shifting direction. The kinematic dimensions of the scrub radius, trail and kingpin angle inclination are the main suspension parameters which effect the TV steering. The upper control arm is one additional part which can be easier changed than the lower links. A different control arm will change the initial toe and the camber angle as well, but this effect will be neglected. The influences of the initial camber and toe angles will be investigated in Subsection 5 and 6. The focus at the present subsection is on the influence of the kinematic movement of the suspension. By changing the connection point f in x-direction the kinematic trail will be changed mainly. A shift of point f in positive x-direction will change the trail in negative x-direction.

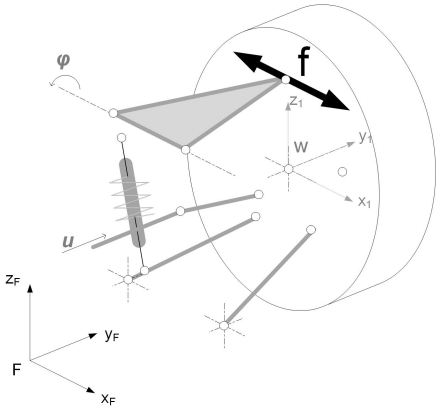

Figure 4.3: Shift of point f in x-direction

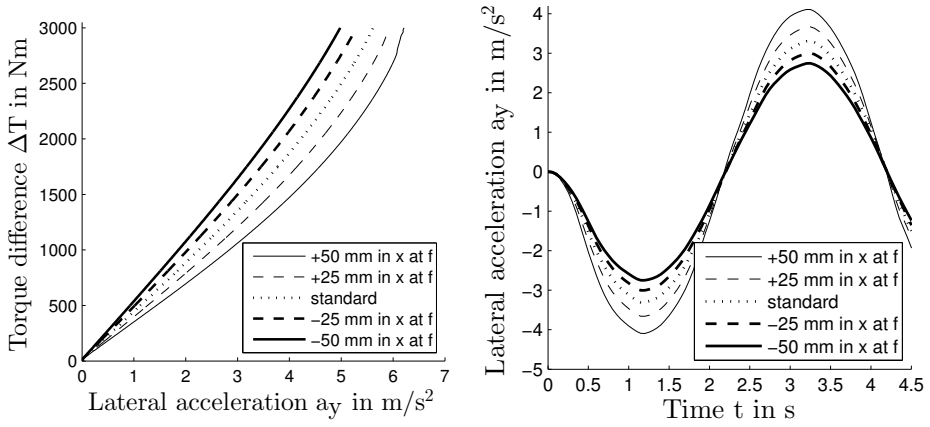

(a) TV mode, ramp steer maneuver at 50 kph

(b) TV mode, slalom maneuver at 50 kph

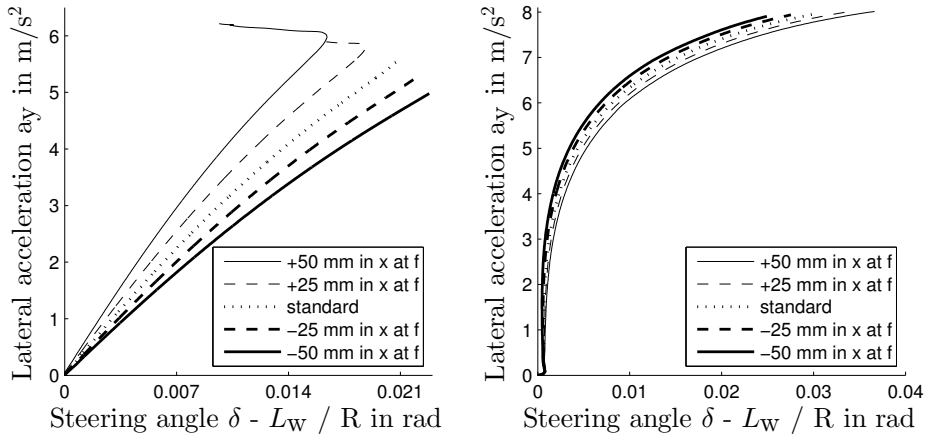

(c) TV mode, ramp steer maneuver at 50 kph

(d) Conventional SbW mode, ramp steer maneuver at 50 kph

Figure 4.4: Upper control arm connection point f shifted in x-direction

Shifting point f in negative x-direction has a positive effect on the TV steering in order to increase the maximum lateral acceleration. But it leads to an oversteering driving behavior in the TV mode and to an understeering driving behavior in the conventional mode.

4. Upper control arm point f in y-direction

Figure 4.6 depicts the point f and the shifting direction.
A shift of point f in y-direction increases mainly the scrub radius. A shift of point f in positive direction (left suspension) increases the scrub radius.

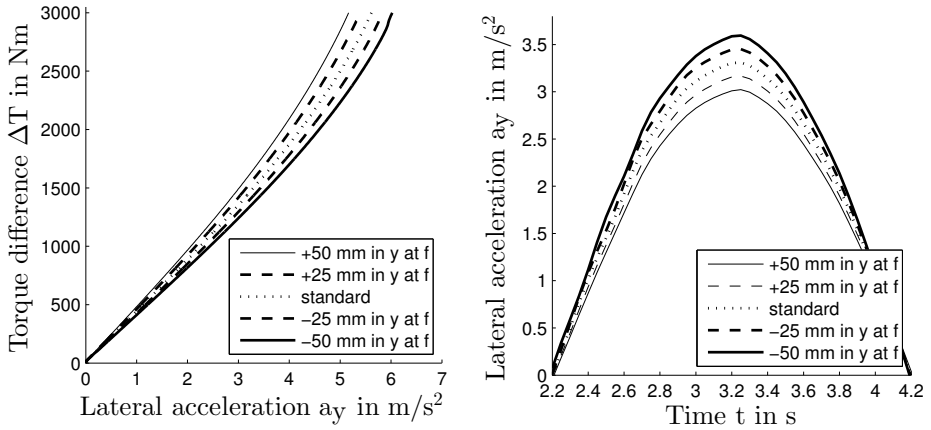

(a) TV mode, ramp steer maneuver at 50 kph

(b) TV mode, slalom maneuver at 50 kph

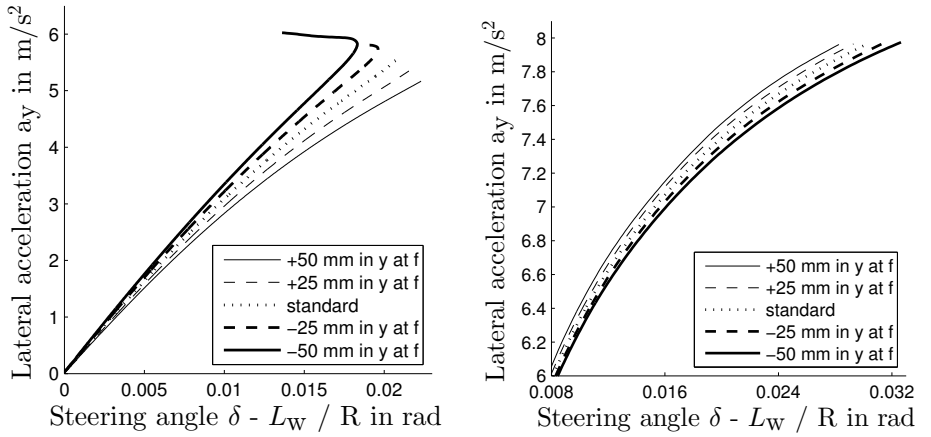

(c) TV mode, ramp steer maneuver at 50 kph

(d) Conventional SbW mode, ramp steer maneuver at 50 kph

Figure 4.5: Upper control arm connection point f shifted in y-direction

Figure (c) 4.5 depicts an oversteering tendency at about 5.5 m/s^2 for a negative shift of

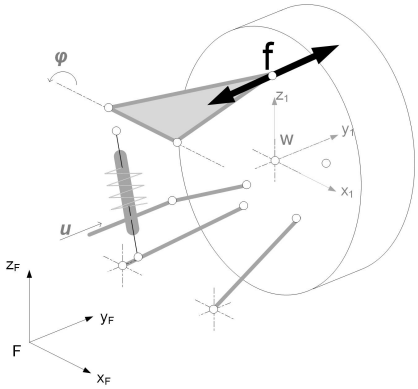

Figure 4.6: Shift of point f in y-direction, at front left suspension

point f in y-direction as well as an increasing lateral acceleration. The opposite driving behavior is depicted in Figure (d) 4.5. Respectively, Figure (b) 4.5 depicts a better performance for the negative shift of point f in y-direction.

5. Toe angle of front wheels

Figure 4.7 depicts the definition of the sign of the toe angle.
The initial toe angle at the front axle can be influenced by adjusting the tie rods or by

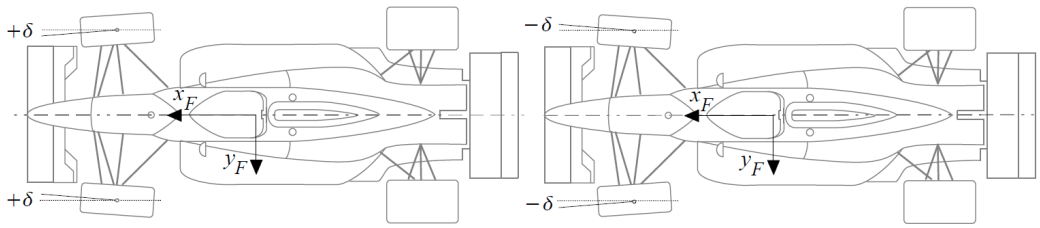

Figure 4.7: Sign of toe angle, grafic from [21]

a different upper control arm like at the Subsections 3 and 4. A positive toe angle can improve the steering response. A disadvantage of big toe angles is the increasing tire wear.

The change of the toe angle leads to a diametrically opposed driving behavior between the TV and the conventional SbW mode. A large negative toe angle leads to an oversteering driving behavior for the TV vehicle, illustrated in Figure (c) 4.8 and a high lateral acceleration at the slalom maneuver, depicted in Figure (b) 4.8. The optimal toe angle will be a trade-off between an efficient TV steering and to achieve a similar driving behavior in both modes.

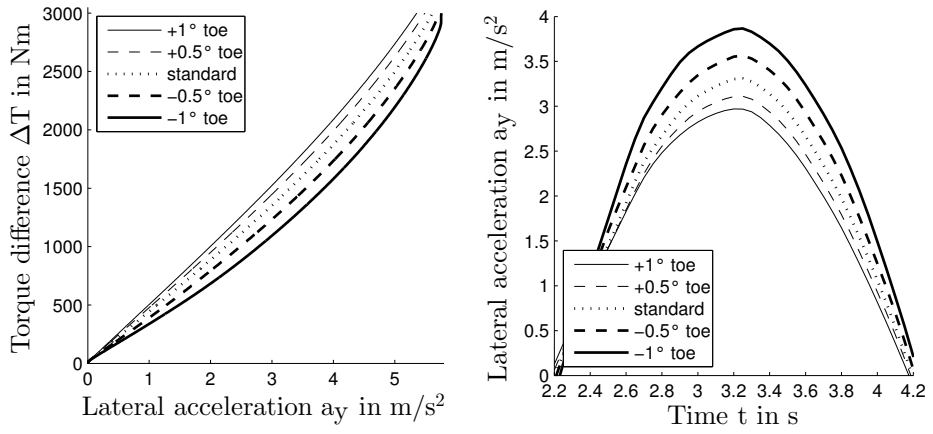

(a) TV mode, ramp steer maneuver at 50 kph

(b) TV mode, slalom maneuver at 50 kph

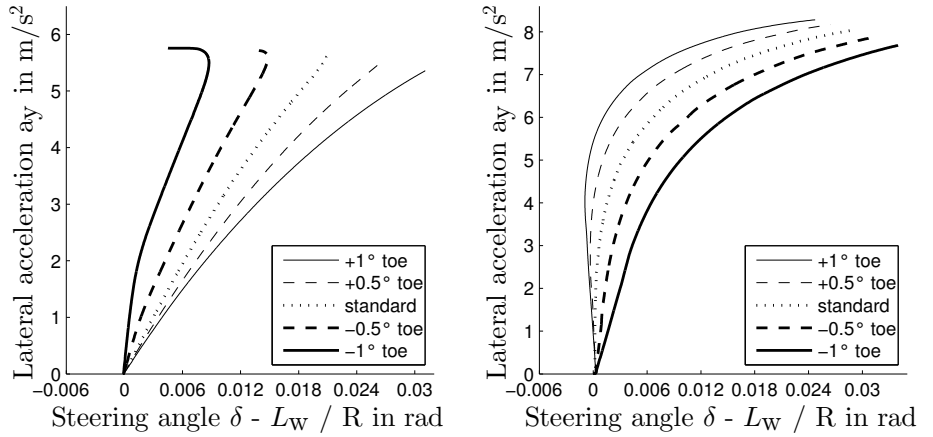

(c) TV mode, ramp steer maneuver at 50 kph

(d) Conventional SbW mode, ramp steer maneuver at 50 kph

Figure 4.8: Change of toe angle of front wheels

6. Camber angle of front wheels

Figure 4.9 depicts the definition of the sign of the camber angle.

The initial camber angle can be changed by a different upper control arm as it was done in the previous subsections. In general, the camber angle affects the driving behavior, maximum lateral acceleration, steering response and tire wear.

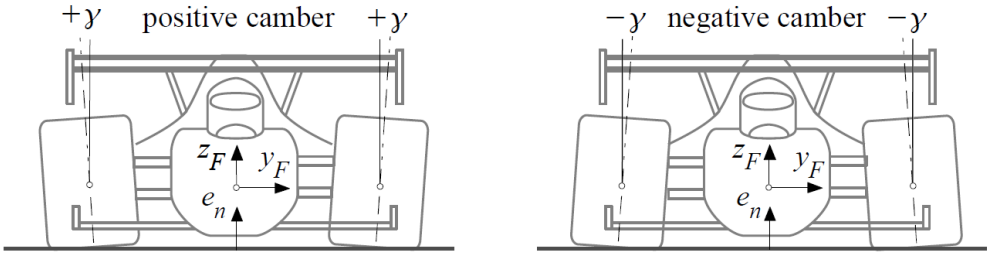

Figure 4.9: Sign of camber angle, grafic from [21]

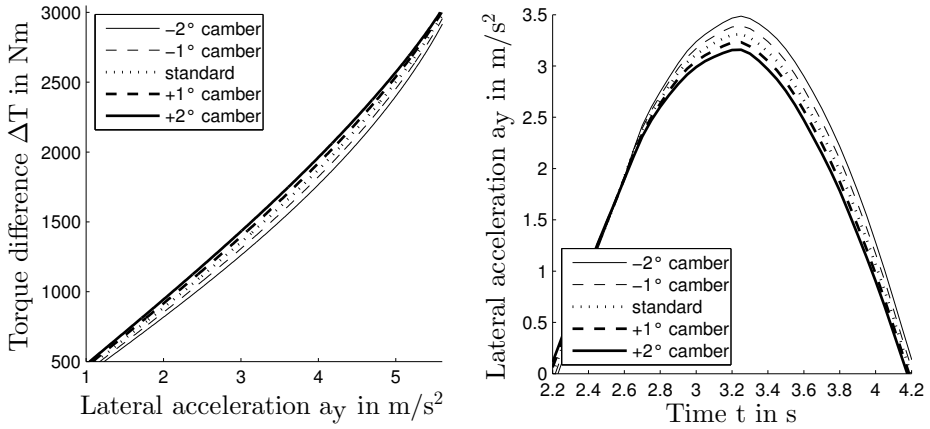

(a) TV mode, ramp steer maneuver at 50 kph

(b) TV mode, slalom maneuver at 50 kph

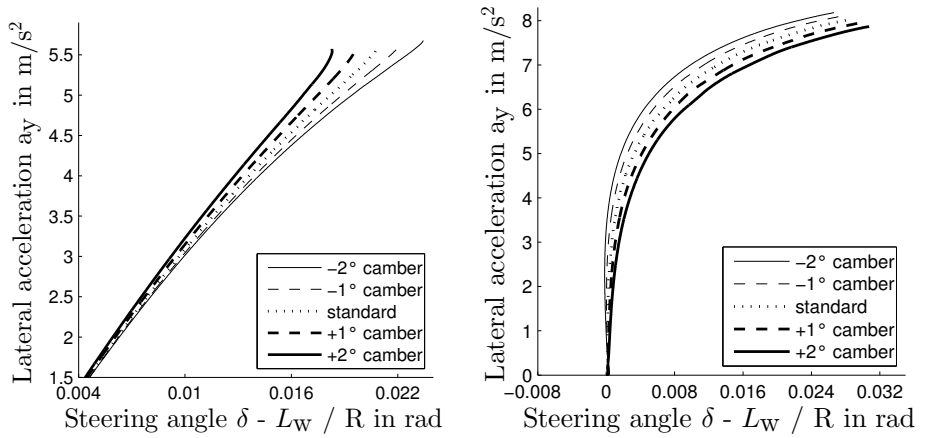

(c) TV mode, ramp steer maneuver at 50 kph

(d) Conventional SbW mode, ramp steer maneuver at 50 kph

Figure 4.10: Change of camber angle of front wheels

The steering tendency has again an opposite behavior, whereby the TV vehicle is more oversteering by negative camber angles, depicted in Figure (c) 4.10, but the maximum lateral acceleration at the slalom maneuver is larger with positive camber angles, depicted in Figure (b) 4.10.

7. CoG shift in x-direction

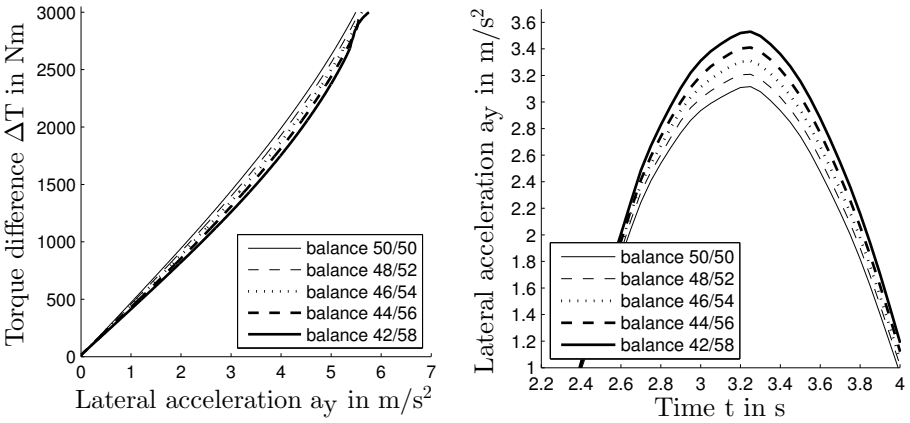

(a) TV mode, ramp steer maneuver at 50 kph

(b) TV mode, slalom maneuver at 50 kph

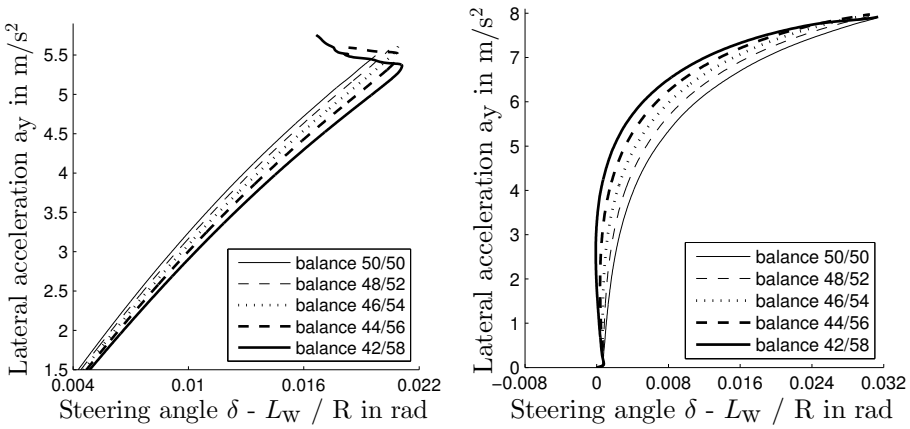

(c) TV mode, ramp steer maneuver at 50 kph

(d) Conventional SbW mode, ramp steer maneuver at 50 kph

Figure 4.11: CoG shift in x-direction

Legend of the plots: balance = weight balance of the vehicle

The position of the CoG is usually a fixed parameter and it is hardly possible to change it. However, the prototype vehicle has a different CoG than the original vehicle. The rebuilding changed the position of the CoG. Therefore, it is one of the overall parameters which is in the center of attention. The stationary cornering driving behavior of a linear

single track model will become more oversteering by increasing the weight balance at the rear wheels [6].

The driving behavior in the conventional SbW mode becomes more oversteering by increasing rear wheel loads, shown in Figure (d) 4.11, and fulfills the expectations. In the TV mode higher rear wheel loads lead to an understeering behavior and at about 5.3 m/s^2 the driving behavior is unstable. It is not possible to determine the driving behavior at this point, depicted in Figure (c) 4.11.

8. CoG shift in z-direction

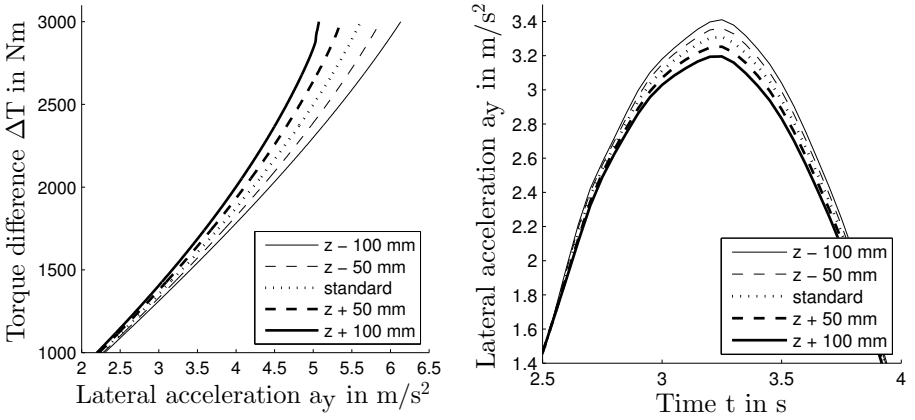

(a) TV mode, ramp steer maneuver at 50 kph

(b) TV mode, slalom maneuver at 50 kph

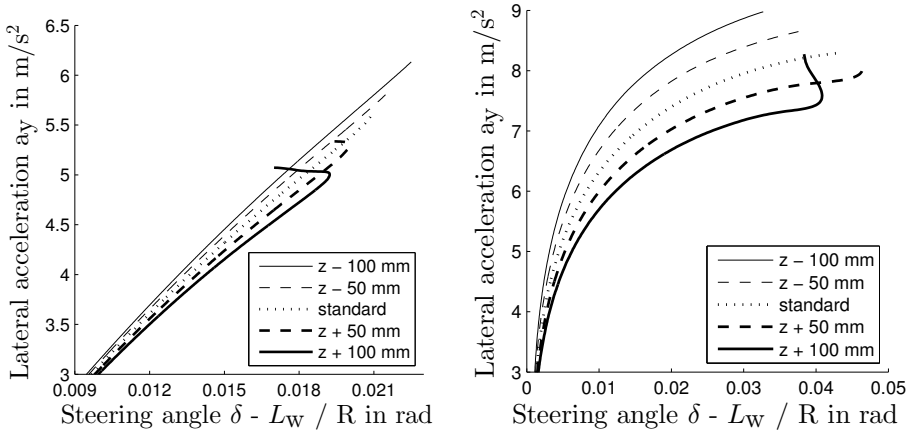

(c) TV mode, ramp steer maneuver at 50 kph

(d) Conventional SbW mode, ramp steer maneuver at 50 kph

Figure 4.12: CoG shift in z-direction

Legend of the plots: z = CoG position in z-direction

In general, a lower CoG position leads to less weight transfer. Hence, a higher lateral

acceleration is possible. The height of the CoG is usually a fixed parameter as well, but it can be changed a lot by extra load on the vehicle roof. Therefore, it is of particular importance to investigate this influence.

As expected the maximum lateral acceleration with a low CoG position is higher than with the original CoG position, at the conventional SbW vehicle, depicted in Figure (d) 4.12. The same driving behavior of the TV vehicle is depicted in Figure (c) 4.12. Figure (b) 4.12 depicts only a small difference between different CoG positions. Figure (a) 4.12 shows the benefits of a low CoG position. Therefore, it is one design goal to lower the CoG position, because it improves the overall efficiency and the driving behavior.

9. Tire cornering stiffness

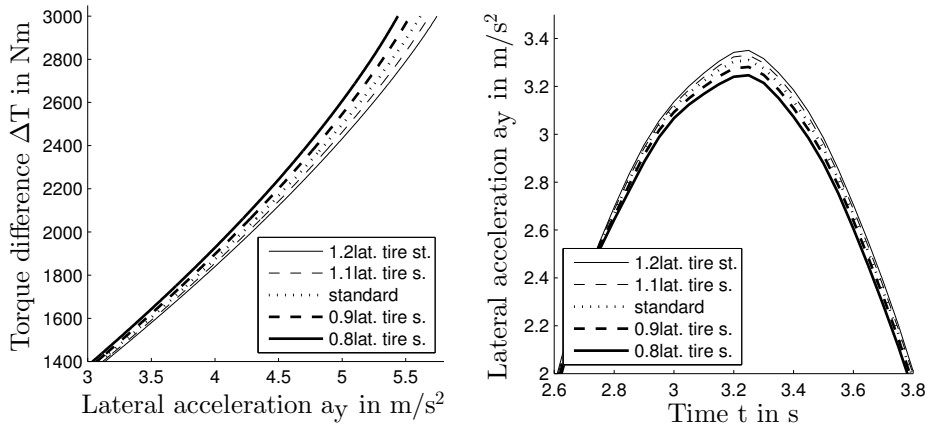

(a) TV mode, ramp steer maneuver at 50 kph

(b) TV mode, slalom maneuver at 50 kph

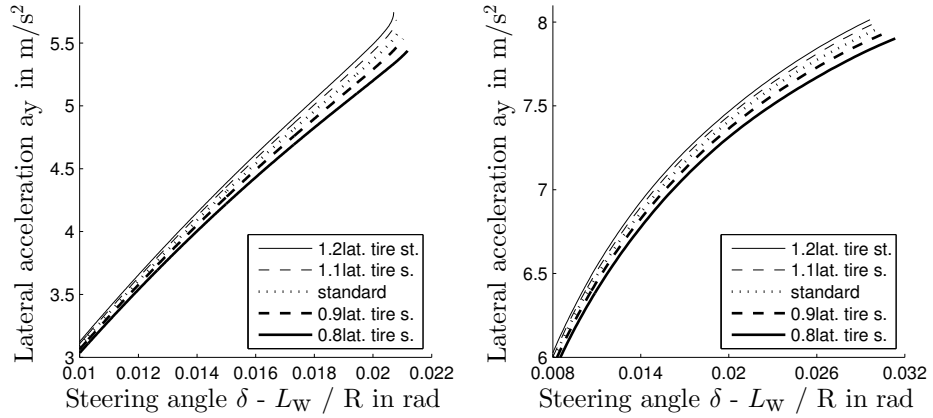

(c) TV mode, ramp steer maneuver at 50 kph

(d) Conventional SbW mode, ramp steer maneuver at 50 kph

Figure 4.13: Change of tire cornering stiffness

Legend of the plots: 1.0lat. tire s. = 100 % of initial cornering tire stiffness

The tire cornering stiffness is a fixed parameter for the given tires, but it can change by using different tires. In general, a higher cornering stiffness leads to a higher lateral acceleration. The variation of this parameter ranges from 80 % to 120 % of the initial tire cornering stiffness.

As expected the maximum acceleration with a larger tire corning stiffness is higher than with the original tires, shown in Figures (b), (c) and (d) 4.13. Additionally, an increasing tire cornering stiffness leads to a more oversteering behavior in the TV as well as in the conventional SbW mode, depicted in Figures (c) and (d) 4.13.

Comparison of set-ups

Maximum rack displacement

A different approach to indirectly show the efficiency of the TV mode is to determine the maximum rack displacement and is depicted in Table 4.3.

The difference of the rack displacement, at the ramp steer maneuver of the TV models at 50 kph, between the maximum of a certain set-up and the standard Δu is denoted as

$$\Delta u = \max\left(u_{\text{setup}}\right) - \max\left(u_{\text{standard}}\right) \tag{4.1}$$

with

$$\max\left(u_{\text{standard}}\right) = 12 \text{ mm} \tag{4.2}$$

at an lateral acceleration of 5.6 m/s^2. Comparing the TV model with the conventional SbW model the rack displacement of a ramp steer maneuver at 50 kph and at 5.6 m/s^2 is given by

$$\max\left(u_{\text{conv.SbW}}\right) = 16.1 \text{ mm}. \tag{4.3}$$

The Table 4.3 depicts the maximum rack displacement in the TV mode of a ramp steer maneuver at 50 kph. The rack displacement is a good indicator for the efficiency of the TV steering.

Table 4.3: Rack displacement

Maximum rack displacement difference					
Nr.	**Set-up name**	**Set-up**	Δu in mm	**Set-up**	Δu in mm
1	Distance plate, spacer	-20 mm	-9	50 mm	4.9
2	Front and rear ARB rate	$2 \times c^f_{arb}$, $0 \times c^r_{arb}$	0.6	$0 \times c^f_{arb}$, $2 \times c^r_{arb}$	-0.4
3	Control arm point f in x-direction	-50 mm	3.8	50 mm	-2.1
4	Control arm point f in y-direction	-50 mm	-1.8	50 mm	-4.3
5	Toe angle of front wheels	$-1°$	-2.5	$-1°$	3.2
6	Camber angle of front wheels	$-2°$	-0.3	$-2°$	0.3
7	CoG position in x-direction	42/58	-0.6	50/50	2.1
8	CoG position in z-direction	-100 mm	0.6	-0.6	-9
9	Tire cornering stiffness	80%	0.9	120%	-0.7

Maximum rack displacement difference of different set-up changes and the standard set-up. The results are given for a ramp steer maneuver at 50 kph and a torque difference of 3000 Nm at the front wheels

4.3 Conclusion of TV analysis

An opposed steering behavior tendency of the TV and conventional SbW mode was noticed, by doing the parameter variation. It will be a challenge to find the optimal set-up for a SbW vehicle with TV as a backup steering system. The design goals could be to lower the engine torques of the driven wheels or to reduce the required torque for the actuator at the steering gear or to have the same desired driving behavior in both modes.
It might be challenging for the driver if the vehicle is understeering in the conventional mode and oversteering in the TV mode . This abrupt change can be avoided by an optimized vehicle design or well-designed controller.
This parameter study shows that the suspension design has to deal with completely new requirements and challenges. Additionally, a SbW vehicle increases the possibility of suspension designing because the transmission ratio between the steering wheel and the rack is not fixed by the steering gearbox anymore.
One finding of the parameter variation is that a TV model requires a vehicle model which is able to describe at least the suspension kinematics as accurate as possible, with a well validated tire model and to take the wheel load transfers into account. A steering angle will change only if there is an unbalance between the forces and the torques of the left and the right side.
This parameter study investigated only the effect of single parameter changes, the next step should be to combine different parameter variations and to find optimal set-ups.
According to Table 4.3, the most effective set-up is the distance plate and the second most effective one is the shift of point f in x-direction. Therefore, the optimization of the suspension geometry is the foundation of a well design TV vehicle.

5 Conclusions and outlook

The goal of the present thesis is to create a simulation model for TV investigations. Chapter 1 described the motivation for this goal, introduced the company TKP and showed the prototype vehicle for this investigations.

The first part of the thesis was focused on creating suspension models for the used three-dimensional vehicle model and was described in Chapter 2 . A detail description of a *double wishbone* suspension is given in [21] and for a *McPherson* suspension in [22]. The further development of suspension models was motivated by these literatures from *Georg Rill*. However, an analytic solution for a *four-link* suspension or an *integral IV* suspension was not found. The concept of modeling such kind of suspension is given in [20]. The determination of the velocity of the required points at the suspension is based on [15].
The present thesis shows how a set of linear kinematic equations can be found for the velocity determination. This is possible even if the computation of the position of suspension elements requires solving nonlinear equations. The used *Jourdain* principle requires the partial derivations of position and rotation vectors. Those were found by the comparison of coefficients of two different descriptions of the velocity.
The used software for the simulation is MATLAB and for solving nonlinear equations additional toolboxes are necessary. Hence, in Chapter 2 the *Newton-Raphson* method is introduced. This method was implemented in the suspension model algorithm to avoid the need of these toolboxes. The computation time of these suspension models satisfied the demands and does not lead to a remarkable additional time. However, the computation time does not have a high priority because this model is only used for off-line simulations.

The following Chapter 3 was about the parameter identification and validation. In summary, it can be stated, that the determination of the masses of the single bodies was quite accurate. As opposite to this, the determination of the moment of inertia tensor of the chassis and the CoG in z-direction was more difficult and the range of variations of errors was higher.
Another weakness of the parameter identification was to get the spring characteristics of the bump stop, which were estimated. Moreover, the given spring and damper parameters are from a brand new car and might not be the same anymore, because the prototype vehicle has a mileage of more than 200,000 km. By doing more accurate measurements or replacing the spring and damper with new parts, it will improve the accuracy of the

parameters.
The road friction coefficient is not a constant vehicle fixed parameter and is dependent on the environment. Hence, it will stay a challenge to get the right value.
The vehicle model itself consists out of rigid bodies, inelastic joints and the sophisticated tire model *TMeasy*. The next step to improve the model would be to consider the elastic behavior of the bushings at the suspensions. However, this would increase the computation time and the complexity of the model. Furthermore, the chassis is one single body and it can be split up in sub-bodies, like drivers, engines and plain chassis. But this step would increase the unknown parameters and some of them might be hard to find.
Another part of Chapter 3 was the validation of the suspensions, the conventional SbW vehicle and the TV vehicle. The validation of the front suspension shows that the more complex *four-link* suspension performs better than the *double wishbone* suspension because it is closer to the real model. In contrast, the simplified model at the rear suspension is more suitable than the complex *integral IV* model. The reason is because the elasto-kinematics are neglected and the closed kinematic chain model of the *integral IV* suspension performs a different movement as the real model. The real model is more elastic and does not twist the suspension that much. That is why a simplified model performs better.

The validation of the conventional SbW vehicle requires an adaptation of two parameters (CoG in z-position and the road friction coefficient) to get the measured driving behavior which is depicted in handling diagrams. Slight deviations of measured and simulated signals were noticed. Probably the reasons are either parameter variations, made assumptions, simplifications by building up the model, measurement errors of the test drives or a combination of them. However, the results meet the requirements for the model and the next step was the validation of the TV model.
The creation of a TV model for vehicle dynamic simulation was the main goal of this thesis. This part was challenging because it is difficult to find existing models or literature. The validation results satisfy the requirements. The difference between the measurements and the simulations are acceptable for further investigations.

Finally, in Chapter 4 the TV model was analyzed and a parameter study was done. The aim was to define parameters, which can be changed at the prototype with a focus on the suspension geometry. The results were provided in four different plots of three different simulated maneuvers. These plots depicted the efficiency, the steering tendency and a comparison with the conventional SbW vehicle. One central outcome was the contrary behavior of the steering tendency at the TV and the conventional SbW mode. Another outcome was that the steering geometry and suspension kinematic affects the TV steering remarkably. The next step can be the design of an optimized suspension which is efficient and guarantees a consistent driving behavior while changing between the conventional SbW mode and the TV mode. Another step is to design a controller which is able to handle a TV steered vehicle. One example for possible difficulties can

be that the high variation of the pneumatic trail of the tires is an essential geometrical parameter which is difficult to detect.

This thesis provides an approach on how to describe the kinematic movement of three-dimensional suspensions without an analytic solution. The modeling concept can be used for similar models or applications. Furthermore, the procedure of parameter identification and validation was described. Finally, a parameter study of the TV model was done. New basic rudiments for suspension designing of a TV steered vehicle were created.

List of Figures

List of Tables

Bibliography

[1] Thyssenkrupp Presta AG. Unternehmen, http://www.thyssenkrupp-presta.com, 2016, Accessed on May 10, 2017.

[2] BMW. Owner's Manual for Vehicle, Online Edition for Part no. 01410012501 -08/06 BMW AG. User manual.

[3] BMW. Productinformation Fahrwerk E70 BMW AG. User manual.

[4] Rüdiger Cordes. Cw-werte, http://rc.opelgt.org, 2017, Accessed on May 10, 2017.

[5] Katrin Ellermann. *Mehrkörperdynamik*. Lecture script, University of Technology Graz, Institut of Mechanics, 2013/14.

[6] Katrin Ellermann. *Fahrzeugdynamik*. Lecture script, University of Technology Graz, Institut of Automovitve Engineering, 2014.

[7] Klaus Esser. Documentation IABG tyre measurement. Report, Thyssenkrupp Presta AG, 2016/17.

[8] Johannes Fehr. *Modellbildung und Parameteridentifikation in der Kraftfahrzeugtechnik*. University of Technology Graz, Institut für Fahrzeugtechnik Graz, Thyssenkrupp Presta AG, November 2015.

[9] Auto-Leebmann GmbH. http://www.leebmann24.de, 2017, Accessed on March 5, 2017.

[10] TU Graz. Ftg - fahrzeugtechnik graz, https://www.tugraz.at/institute/ftg/institut-fuer-fahrzeugtechnik/, Accessed on May 10, 2017.

[11] K.-H. Grote and J. Feldhusen. *Dubbel, Taschenbuch für den Maschinenbau*. Springer-Verlag, 2007.

[12] Dr. Ing. h.c. F. Porsche AG. Unternehmen, http://www.porscheengineering.com/nardo/de/thecompany/, 2017, Accessed on May 10, 2017.

[13] Reza N. Jaza. *Theory of Applied Robotics*. Springer-Verlag, 2010.

[14] Franz Michael Leichtfried. *Parameterbestimmung von vereinfachten Fahrdynamikmodellen anhand ausgewählter Fahrmanöver*. University of Technology Graz,Institut für Fahrzeugtechnik Graz, May 2015.

[15] Wolfgang Matschinsky. *Radführung von Straßenfahrzeugen, Kinematik, Elsto-Kinematik und Konstruktion*. Springer-Verlag, 2007.

[16] Andreas Mitterrutzner. *Development and Validation of a Vehicle Model for real time application on a Steer-by-Wire prototype.* University of Technology Graz, Institut für Fahrzeugtechnik Graz, Thyssenkrupp Presta AG, April 2015.

[17] Hans B. Pacejka and Egbert Bakker. The magic formula tire model. Technical report, Delft Univercity of Technology and NedCar Engineering & Development B.V., 2007.

[18] Cornel Pfister and Jan Reis. *Entwicklung eines Regelalgorithmus zum Lenken eines Fahrzeugs mit Einzelradantrieb durch Torque Vectoring.* NTB Buchs, Thyssenkrupp Presta AG, March 2016.

[19] Kristof Polmans and Sebastian Stracke. Torque Vectoring as redundant steering for automated driving or steer-by-wire. 5th international munich chassis symposium 2014, ThyssenKrupp Presta AG, RWTH Aachen.

[20] Georg Rill. *Simulation von Kraftfahrzeugen.* Vieweg-Verlag, 2007.

[21] Georg Rill. *Road Vehicle Dynamics, Fundamentals and Modeling.* CRC Press, 2012.

[22] Georg Rill and Thomas Schaeffer. *Grundlagen und Methodik der Mehrkörpersimulation.* Springer, 2014.

[23] Marco Schneider, Rafael Vincenz, and Andreas Reichmuth. SUNCAR Steer by Wire 2014/15 Endbericht Mechanik und Thermomanagement. Report, ETH Zuerich, 2014/15.

[24] Dieter Schramm, Manfred Hiller, and Roberto Bardini. *Vehicle dynamics, Modeling and Simulation.* Springer, 2014.